UNIVERSITY OF CALIFORNIA,
IRVINE

Characterization of a pathogenic conformation of amyloid immunoreactivity in Alzheimer's Disease and Cerebral Amyloid Angiopathy

DISSERTATION

Submitted in partial satisfaction of the requirements
for the degree of

DOCTOR OF PHILOSOPHY

in Biological Sciences

by

Ricardo Albay III

Disseration Committee:
Professor Charles G. Glabe, Chair
Professor Craig Walsh
Professor Leslie Thompson

2018

DEDICATION

To

Olivia and Gabriela Albay

beautiful reminders of what life is all about

“True wealth is not measured in money or status or power. It is measured in the legacy we leave behind for those we love and those we inspire.”

-Cesar Chavez

TABLE OF CONTENTS

LIST OF FIGURES

Chapter 1

Chapter 2

Chapter 3

Chapter 4

LIST OF TABLES

Chapter 1

Chapter 2

Chapter 3

ACKNOWLEDGEMENTS

I would like to express the deepest gratitude to my advisor, Professor Charles G. Glabe, you have been generous with your time, patience, and advice. I would like to thank you for establishing a research program that has significant importance to human health and surrounding me with scientists that encouraged creativity, independence, and the unbiased interpretation of data. These bright scientist include: Dr. Asa Hatami, Dr. Anna Pensalfini, Dr. Justyna Sosna, Dr. Stephan Philipp, Dr. Jorge Reyes-Ruiz, Dr. Jessica Wu, Dr. Saskia Milton, Lawrence Margol and Dr. Suhail Rasool.

I would also like to thank my advancement, and later dissertation committee members, Professor Dana Aswad, Professor Luis Villarreal, Professor Craig Walsh, and Professor Leslie Thompson for their guidance, constructive criticisms, and support.

Many thanks to the talented students that assisted with various aspects of this dissertation work, including: Sunit Misra, Jessica Carranza, Margaret Ho, Alysza Permalino, Micaela Arambel, and Courtney Crivelli.

This work was made possible by the love and support of my family. To my grandparents and parents, thank you for teaching me the value of an education, encouraging me to set goals and to persevere. To my father- and mother-in law Jesus and Carmen Rodriguez, thank you for being role models; your unwavering support means a great deal to me. To David, Krhystal, Marina, Natalia, Micaela, Alejandro, Eriberto, and Jesus, thank you for all of the support and laughs!

To my wife Gabriela, thank you for being so patient throughout this journey. I am grateful that for over a decade you have always been there for me, believed in me, and encouraged me. Know that you are my best friend and I love you more than words can describe.

Financial support was provided by the University of California, Irvine, NIH grants AG000538, AG033069, AG045729, and the Cure Alzheimer's Foundation.

CURRICULUM VITAE

Ricardo Albay III

2018	Doctor of Philosophy in Biological Sciences Concentration in Molecular Biology and Biochemistry University of California, Irvine Advisor: Prof. Charles G. Glabe
2016	Teaching Intern, School of Life Sciences & Technologies, Irvine Valley College, Irvine -Biochemistry and Molecular Biology
2014-15	Teaching Assistant, Department of Molecular Biology and Biochemistry, University of California, Irvine - Molecular Biology (BS99) and Molecular Biology Lab (BS116L)
2010	Graduate Student Researcher, Department of Biology, California State University, Los Angeles - Advisor: Amelia Russo-Neustadt
2009	Post-Baccalaureate Fellow, Department of Molecular Biology and Biochemistry, University of California, Irvine - Advisor: Professors Luis Villarreal and Charles Glabe
2005-2009	Bachelor of Science, Biopsychology University of California, Santa Barbara

FIELD OF STUDY

Characterization of a pathogenic conformation of amyloid immunoreactivity in Alzheimer's Disease and Cerebral Amyloid Angiopathy

PUBLICATIONS

1. **Albay, R**., Carranza, J., Ho, M., Permalino, A., Arambel, M., Sosna, J., & Glabe, C. G. (2018). Characterization of a pathogenic conformation of amyloid immunoreactivity in Alzheimer's Disease and Cerebral Amyloid Angiopathy. (In preparation).

2. Gonzalez,B.L., Bilousova, T., Miyoshi, E., Poon, W., Vinters, H., Miller, CA., Corrada, M., Kawas, C., Hatami, A., **Albay, R.**, Glabe, C., Gylys, K. (2018) Apolipoprotein E/Amyloid beta complex accumulates in AD cortical synapses via apoE receptors and is enhanced by APOE4. (Summited American Journal of Pathology)

3. Sosna, J., Philipp, S., **Albay, R.**, Reyes-Ruiz, J. M., Baglietto-Vargas, D., LaFerla, F. M., & Glabe, C. G. (2018). Early long-term administration of the CSF1R inhibitor PLX3397 ablates microglia and reduces accumulation of intraneuronal amyloid, neuritic plaque deposition and pre-fibrillar oligomers in 5XFAD mouse model of Alzheimer's disease, 1–11. http://doi.org/10.1186/s13024-018-0244-x

4. Knight, E. M., Kim, S. H., Kottwitz, J. C., Hatami, A., **Albay, R.**, Suzuki, A., et al. (2016). Effective anti-Alzheimer Aβ therapy involves depletion of specific Aβ oligomer subtypes. Neurology - Neuroimmunology Neuroinflammation, 3(3), e237–10. http://doi.org/10.1212/NXI.0000000000000237

5. Bilousova, T., Miller, C. A., Poon, W. W., Vinters, H. V., Corrada, M., Kawas, C., et al. (2016). Synaptic Amyloid-β Oligomers Precede p-Tau and Differentiate High Pathology Control Cases. The American Journal of Pathology, 186(1), 185–198. http://doi.org/10.1016/j.ajpath.2015.09.018

6. Hatami, A., **Albay, R.**, Monjazeb, S., Milton, S., & Glabe, C. (2014). Monoclonal antibodies against Aβ42 fibrils distinguish multiple aggregation state polymorphisms in vitro and in Alzheimer disease brain. The Journal of Biological Chemistry, 289(46), 32131–32143. http://doi.org/10.1074/jbc.M114.594846

7. Pensalfini, A., **Albay, R.**, Rasool, S., Wu, J. W., Hatami, A., Arai, H., et al. (2014). Intracellular amyloid and the neuronal origin of Alzheimer neuritic plaques. Neurobiology of Disease, 71, 53–61. http://doi.org/10.1016/j.nbd.2014.07.011

8. McLean, D., Cooke, M. J., **Albay, R.**, Glabe, C., & Shoichet, M. S. (2013). Positron emission tomography imaging of fibrillar parenchymal and vascular amyloid-β in TgCRND8 mice. ACS Chemical Neuroscience, 4(4), 613–623. http://doi.org/10.1021/cn300226q

9. Rasool, S., **Albay, R., III**, Martinez-Coria, H., Breydo, L., Wu, J., Milton, S., et al. (2012). Vaccination with a non-human random sequence amyloid oligomer mimic results in improved cognitive function and reduced plaque deposition and micro hemorrhage in Tg2576 mice. Molecular Neurodegeneration, 7(1), 1–1. http://doi.org/10.1186/1750-1326-7-37

10. Kayed, R., Canto, I., Breydo, L., Rasool, S., Lukacsovich, T., Wu, J., et al. (2010). Conformation dependent monoclonal antibodies distinguish different replicating strains orconformers of pre-fibrillar Ab oligomers. Molecular Neurodegeneration, 5(1), 57. http://doi.org/10.1186/1750-1326-5-57

11. Slaten, E. R., Hernandez, M. C., **Albay, R.**, Lavian, R., & Janusonis, S. (2010). Transient expression of serotonin 5-HT4 receptors in the mouse developing thalamocortical projections. Developmental Neurobiology, 70(3), 165–181. http://doi.org/10.1002/dneu.20775

12. **Albay, R.**, Chen, A., Anderson, G. M., Tatevosyan, M., & Janusonis, S. (2009). Relationships among body mass, brain size, gut length, and blood tryptophan and serotonin in young wild-type mice. BMC Physiology, 9(1), 4. http://doi.org/10.1186/1472-6793-9-4

CONFERENCE PRESENTATIONS

R. Albay, III, J. Carranza, S. Milton, C. G. Glabe. A unique conformation of amyloid is associated with cerebrovascular amyloid deposits and smooth muscle cell degeneration. Program No. 768.09. 2014 Neuroscience Meeting Planner. Washington D.C.: Society for Neuroscience, 2014. Online.

R. Albay, III, S. Misra, A. Pensalfini, C. G. Glabe. Intracellular M78 nuclear immunoreactivity is associated with increased histone H3 trimethylation and changes in chromatin structure. Program No. 40.25/G45. 2013 Neuroscience Meeting Planner. San Diego, CA: Society for Neuroscience, 2013. Online.

R. Albay, III, A. Pensalfini, A. Hatami, S. Milton, H. Arai, C. G. Glabe. A unique conformation of amyloid is associated with cerebrovascular amyloid deposits. Program No. 436.05/C64. 2012 Neuroscience Meeting Planner. New Orleans, LA: Society for Neuroscience, 2012. Online.

A. Pensalfini, R. Albay, III, L. Margol, A. Hatami, S. Rasool, H. Arai, S. Milton, W. Poon, Z. Shan, C. Glabe. Intranuclear M78 amyloid immunoreactivity colocalizes with nuclear APP-CTF immunoreactivity in early Alzheimer's Disease. Program No. 436.06/C65. 2012 Neuroscience Meeting Planner. New Orleans, LA: Society for Neuroscience, 2012. Online.

A. Pensalfini, S. Rasool, R. Albay, A. Hatami, J. Wu, H. Arai, W. Poon, Z. Shan, M. Corrada, C. Kawas, C. Glabe. Intranuclear accumulation of a novel type of amyloid is associated with loss of nuclear DNA in early Alzheimer's Disease. Program No. 47.13/O6. 2011 Neuroscience Meeting Planner. Washington, DC: Society for Neuroscience, 2011. Online.

S. Rasool, H. M. Coria, L. Breydo, J. Wu, S. Milton, A. Tran, R. Albay, C. G. Glabe. Non human amyloid oligomer epitope reduces Alzheimer's-like neuropathology in 3xTg-AD transgenic mice. Program No. 725.6. 2010 Neuroscience Meeting Planner. San Diego, CA: Society for Neuroscience, 2010. Online.

M.C. Hernandez, R. Albay, S. Janusonis. (2009) Serotonin 5-HT4 and adrenergic β2 receptors in the developing forebrain: Anti-sense proteins and autism. Society for Neuroscience Abstracts 345.1/G16.

Janusonis S., Albay R., Tatevosyan M., Chen A. (2008) The blood hyperserotonemia of autism as a multisystem problem. Society for Neuroscience Abstracts 345.28/V17.

AWARDS AND PROFESSIONAL MEMBERSHIPS

2009-present	Society for Neuroscience
2010	MBRS-RISE M.S. to Ph.D. Fellowship (CSULA)
2009	Post-Baccalaureate Research and Education Fellowship (UCI)
2007-2009	Undergraduate Research and Creative Activities Grant (UCSB)00

ABSTRACT OF THE DISSERTATION

Characterization of a pathogenic conformation of amyloid immunoreactivity in Alzheimer's Disease and Cerebral Amyloid Angiopathy

By

Ricardo Albay III

Doctor of Philosophy in Biological Sciences

University of California, Irvine, 2018

Professor Charles G. Glabe, Chair

The deposition of the amyloid β protein (Aβ) in the brain as plaques and the formation of neurofibrillary tangles (NFT) filled with hyper-phosphorylated tau are the canonical histopathological hallmarks of Alzheimer's disease (AD). The genetics of early onset, familial Alzheimer's disease (fAD) supports a causal role of Aβ in AD pathogenesis. However, plaques do not correlate with dementia and therapeutic strategies inhibiting the production of soluble Aβ or leveraging monoclonal antibodies to target the removal of monomeric Aβ have produced disappointing results. Despite the therapeutic pitfalls that sequence specific antibodies have faced, conformation dependent monoclonal antibodies provide an invaluable tool to investigate specific conformations of protein aggregates whose relative abundance may prove significant to the pathogenesis of disease. By investigating the pathological significance of a unique subpopulation of vascular amyloid we addressed a knowledge gap that exists in understanding the role conformational diversity of amyloid structure plays in Alzheimer's pathology. The data presented here demonstrate that monoclonal antibodies recognize deposits in human and

transgenic mouse brain that are spatially, temporally, and morphologically diverse (Chapter 1). We report a unique immunoreactivity in vascular smooth muscle cells (VSMC) that correlates with plaque pathology and a loss of α-actin immunoreactivity in AD brains and transgenic mouse models of AD (Chapter 2). We investigated whether mOC31 immunoreactivity was associated with markers of inflammation, including the activation of microglia, presence of pro-inflammatory signals interleukin-1β (IL1β) and high-mobility group box 1 (HMGB1); we found that HMGB1 is colocalized with mOC31 immunoreactivity in the cytosol of VSMC (Chapter 2). To address the causative link between Aβ and mOC31 immunoreactivity with the observed loss of α-actin immunoreactivity we developed an *in vitro* model utilizing primary human brain vascular smooth muscle cells (HBVSMC). In this model, we found that exogenous treatment with Aβ40-WT and Aβ40-A21G was sufficient to induce the loss of α-actin immunoreactivity observed in human and transgenic mouse brain (Chapter 3). Furthermore, we report a loss of membrane integrity and a direct interaction between Aβ and α-actin. These results suggest that Aβ may have both indirect and direct effects on VSMC phenotype. Our findings demonstrate that amyloid heterogeneity is a significant factor to consider in the development of disease modifying therapeutics.

INTRODUCTION

In 1906, Alois Alzheimer described for the first time a unique set of behavioral abnormalities in a 51-year old woman that he had treated for 5 years. In his report he recalled observing: progressive cognitive impairment, focal symptoms, hallucinations, delusions, and psychosocial incompetence. At necropsy, he observed the presence of plaques and neurofibrillary tangles in the brain that, in concert with astrogliosis, neuronal dystrophy, neuronal loss, and vascular alterations, have become the canonical hallmarks of the disorder. Alzheimer's disease is now recognized as the most common irreversible, progressive cause of dementia, the sixth leading cause of death in the United States and has become a social and economic issue in that there is no cure, no way to prevent it and no way to slow disease progression. Given that aging is a major risk factor, a sense of urgency is building as it is estimated that by 2050, 11 million Americans will be affected by the disease; increasing annual health care cost to a projected US$1 trillion [1].

Amyloid cascade hypothesis

The neuropathological diagnosis of Alzheimer's disease requires the evaluation of location, distribution, and abundance of characteristic brain lesions during the autopsy of a subject that has been clinically diagnosed [2]. Senile plaques are a type of parenchymal brain lesion evaluated by medical examiners to confirm the clinical diagnosis of AD. These extracellular deposits were first observed in 1892 by Blocq and Marinesco, associated with a subtype of dementia by Alzheimer in 1907 and named in 1911 by Simchowicz. The main component of plaques, amyloid β-peptide (Aβ), was not discovered until 1984 when it was isolated and sequenced from the meningeal blood vessels of AD patients and individuals with Down syndrome (DS) [3,4]. Early

comparisons between vascular and plaque amyloid revealed that both were composed of almost identical 4-kD polypetide and similar antigenic epitopes; with a notable difference in the length of the polypeptide c-terminus (Aβ39 vs Aβ42, respectively) [5,6]. The subsequent cloning of the gene encoding the precursor to the amyloid β protein (APP: amyloid protein precursor) and its localization to chromosome 21 [7,8], together with the observation that trisomy 21 or Down syndrome leads to the neuropathology of AD [9], set the stage for the proposal that the primary event in AD pathogenesis is Aβ accumulation. Further analysis into the vascular deposits that characterize both the Dutch type of hereditary cerebral hemorrhage with amyloidosis (HCHWA-D) and AD provided the first incidence where amyloid accumulation was the direct result of mutations in the *APP* gene [10].

Inheritable forms of AD invariably result in a clinical diagnosis before the age of 65 and are referred to as Alzheimer's disease with an early onset (EOAD). A subset of EOAD are caused by mutations and/or duplications in the *APP* gene and are commonly referred to as familial AD (fAD); this is in contrast with sporadic AD (sAD) for which no single cause can be attributed. APP is a type-I protein that contains a short cytoplasmic region and a large extracellular domain. The amyloid precursor is proteolytically processed by two distinct pathways: non-amyloidogenic and amyloidogenic. In the non-amyloidogenic processing pathway, APP is cleaved by α-secretase (membrane tethered ADAM) that results in the formation of a large soluble ectodomain (sAPPα) and an 83-amino acid membrane associated C-terminal fragment (C83). The amyloidogenic pathway gives rise to three fragments sAPPβ, Aβ, and AICD after the sequential cleavage of APP

in the extracellular domain by β-secretase (membrane tethered BACE) and in the transmembrane region by γ-secretase (membrane embedded complex with presenilin).

In excess of fifty *APP* mutations have been observed with twenty-six of these fAD alterations occurring in exon 16 and 17 which corresponds to the n-, c-terminus, and Aβ regions of APP [11,12]. A double mutation occurs in a Swedish fAD pedigree at codons 670 and 671 that corresponds to the n-terminus of Aβ. The K670N/M671L in the APP protein is located immediately upstream the β-secretase cleavage site and shifts the production of total Aβ, resulting in higher levels of both Aβ40 and Aβ42 in vitro [13]. Eleven pathogenic mutations have been reported within the Aβ sequence that include: A673V, D678N, E682K (Leuven mutation), A692G (Flemish mutation), E693Q (Dutch mutation, HZCHWA-D), E693K (Italian mutation), E693G (Arctic mutation), E693del, D694N (Iowa mutation), L705V, and A713T. The effects associated with alterations in the Aβ sequence are diverse; for example, the E693Q (Dutch) and E693G (Arctic) have been shown to enhance the aggregation of Aβ into protofibrils or fibrils [14,15], where AD patients carrying the A692G (Flemish) mutation predominately deposit Aβ40 into vascular walls [16]. Furthermore, fourteen mutations are localized at the c-terminus of Aβ and near the γ-secretase cleave site and involve codons 714-717 and 723-724. These mutations include: T714l/A, V715M/A, V716V/T/F/ M, and V717l/G/L/F, and L723P and K724N and selectively lead to an increase in longer forms of Aβ peptides [17,18]. Although a majority of *APP* mutations are pathogenic, one mutation, A673T protects against AD and cognitive decline in elderly without Alzheimer's disease by reducing the β-cleavage of APP that effectively reduces levels of secreted Aβ [19]. In addition to *APP* on chromosome 21, the AD locus has

expanded to include chromosome 14, and 1; implicating the genes: *PSEN1* and *PSEN2*, respectively. These loci encode for the active site of γ-secretase and alter APP metabolism in a way that elevates the relative levels of long Aβ peptides [20,21]. Although the exact mechanism for each specific mutation in *PSEN1* and *PSEN2* differ, in all cases the mutations appear to decrease the C- to N-terminal carboxyl-peptidase function of γ-secretase and results in a gain of toxic Aβ42/Aβ40 [22]. Together *APP, PSEN1, and PSEN2* account for over three-hundred mutations and strongly support the hypothesis that Aβ is the causative agent in AD.

The genetics of EOAD support a causal role of Aβ in AD pathogenesis; however, neurofibrillary tangle counts correlate better with cognitive impairment than amyloid plaque burden [23]. Therapeutic strategies utilizing small-molecules that inhibit the production of Aβ by targeting β-secretase (LY2886721) and γ-secretase (Semagacestat) have been plagued with toxicity issues or worsen cognitive function [24]. Treatments involving monoclonal antibodies to target the removal of Aβ have produced disappointing results as well, for example: the clinical trail for Bapineuzumab was discontinued midway after patients with mild to moderate AD showed no treatment effect on either cognitive or functional outcomes; even when biomarker analysis indicated the antibody engaged its target [25]. A second monoclonal antibody, Solanezumab, had shown encouraging results in Phase 3 clinical trials in mild (but not moderate) AD patients but was also terminated after several endpoints goals were not met with statistical significance [26]. AD immunotherapy had a break-through when a phase 1b clinal trail showed a human monoclonal antibody for oligomeric and fibrillar Aβ (aducanumab) not only engaged amyloid plaques, the therapy halted disease progression and provided significant benefit in multiple

cognitive measures [27]. Two unique feature may be contributing to the success of aducanumab: (1) researchers used reverse translational medicine to isolate a monoclonal antibody from healthy individuals for the treatment of disease and (2) the antibody recognizes an aggregation specific epitope that is not present in monomeric Aβ. The recent success and not too distant failures bring forward the inherit difficultly involved in working with amyloid and highlight that not all antibodies are created equal. Together these results stress the central role amyloid heterogeneity plays in the amyloid cascade hypothesis.

Cerebral Amyloid Angiopathy

Cerebral amyloid angiopathy (CAA) is a term used to describe the pathological process during which an amyloid protein progressively deposits in arterioles and small arteries with subsequent degenerative vascular changes and is often an under appreciated lesion of AD. CAA can occur with or without AD and be either sporadic or hereditary, as in the case of hereditary cerebral hemorrhage with amyloidosis (HCHWA). HCHWA-(Dutch, Italian, Arctic, Iowa, Flemish, and Piedmont) is caused by a mutation in the *APP* gene that frequently result in either the substitution or deletion of an amino acid adjacent to residues 21 and 22 on the Aβ peptide [28,29]. These changes to Aβ increase the propensity of the peptide to oligomerize, fibrillize, or be cleared less effectively [30,31]. Sporadic and inherited CAA is recognized within brain tissue by the presence of a characteristic acellular thickening of vessel walls and commonly stained by periodic acid-Schiff (carbohydrate macromolecules in connective tissue), toluidine blue, crystal violet, thioflavin S or T (fluorescent under ultraviolet light), and Congo red stain (yellow-green birefringence under polarized light) [32]. Intracerebral hemorrhage is a pathological hallmark of

CAA that generally occurs in the cortical and cortico-subcortical (lobar) brain regions where the vascular amyloid despots are most frequent [33]. Recurrent lobar intracerebral hemorrhage has been shown to be significantly associated with apolipoprotein E (apoE) genotype [34].

In the central nervous system, apoE is produced primarily by smooth muscle cells, astrocytes, microglia and under certain conditions by neurons [35]. Commonly found in high-density lipoprotein (HDL)-like particles, apoE in the CNS is believed to play a role in reverse cholesterol transport, lipid delivery, as well as facilitating synaptogenesis in neurons [36,37]. The human *APOE* gene is located on chromosome 19 and contains several single nucleotide polymorphisms (SNPs); the most common three SNPs lead to amino acid substitutions and give rise to three common isoforms of apoE: apoE2 (cys112, cys158), apoE3 (cys112, arg158), and apoE4 (arg158, arg158) [38]. ApoE was linked to AD pathogenesis after it was discovered to colocalized with amyloid plaques and the ε4 allele of the *APOE* gene was discovered to be a strong genetic risk factor for familial and sporadic late-onset AD (LOAD) and CAA [39,40]. Although the severity of CAA in AD is variable, it is however, identified in 85-95% of AD brains. Individuals with one ε4 allele are threefold more likely to develop AD by the age of 65 and approximately twelvefold in those with two ε4 allele [41]. Identifying the underlying mechanism for how apoE influences Aβ accumulation in the brain is still a work in-progress with in vitro and in vivo studies suggesting that apoE may influence soluble Aβ clearance. For example, a study has shown that apoE isoforms do not significantly influence Aβ production and processing in vivo; rather, apoE isoforms differentially affect Aβ clearance before plaque formation in the brain with apoE4 resulting in clearance that is slower than E3 and E2 [42].

While most of the apoE biology in AD has been investigated in mammalian cell and mouse models, a report using human induced pluripotent stem cells (hiPSCs) has revealed a possible species specific differences where in human cells apoE4 provides a gain of toxic function in AD pathogenesis in regards to Aβ production, tau phosphorylation, and GABAergic neuron degeneration [43].

Pathological studies have shown a positive correlation between plaque density and ε4 allele dose in AD patients at autopsy and transgenic mice that develop Aβ deposition and express human apoE isoforms have a strong effect on the time of onset of Aβ deposition as well as the amount, location, and conformation of Aβ in the brain [44,45]. Additionally, crossing human apoE to Tg2576 and 3xTg-AD mice both result in a relative shift of Aβ deposition from the brain parenchyma to arterioles in the form of CAA in apoE4 expressing mice when compared to apoE3 or mouse apoE [46,47]. A similar effect of apoE4 predisposing to CAA is seen in humans with more Aβ40 amyloid depositing into brain vasculature in a dose and isoform (ε4>ε3>ε2) dependent manner [48]. Neuropathological studies have demonstrated that Aβ deposition is associated with localized loss of smooth muscle cells (SMC), weakening of the vessel wall, rupture and hemorrhage into the brain [49]. Furthermore, disruption of SMC was shown to interfere with the ability of the vessel to respond to both endothelial-dependent and independent vasodilators, suggesting an underlying loss of coordinated SMC function in affected vessels [50].

Late-onset Alzheimer's disease is the most common form of human dementia that does not currently have a unique neuropathological mechanism that causes disease but rather has multiple

concomitant factors. The most common factor contributing to LOAD, supported by *APOE* genetics, is the accumulation of vascular amyloid in vessels and the effect CAA has on SMC; the predominate regulator of cerebral blood flow in physiological and pathological conditions [51]. A multifactorial study that analyzed thousands of brain images and followed changes in tens of plasma and cerebral spinal fluid biomarkers from the Alzheimer's Disease Neuroimaging Initiative (ADNI) revealed a strong correlation between LOAD and vascular disregulation as an early pathological event during disease development [52]. Altogether, these studies demonstrate that the detrimental effects of Aβ are not limited to the brain parenchyma and spreads over into the cerebral vascular system responsible for maintaining homeostasis before the diagnosis of AD; the demise of vascular cells appears to exacerbate an already perilous situation.

The 'strain' paradigm of Alzheimer's disease

The observation that some mutations in *APP* give rise to florid parenchymal amyloid deposition and memory loss while others result in cerebral amyloid angiopathy with severe cases causing stroke mirrors the 'strain' paradigm of prion disease. That is, some mutations in the prion protein (PrP) give rise to spongiform degeneration as in Creutzfeld-Jakob disease (gCJV) and Gerstmann–Sträussler–Scheinker syndrome (GSS), while other mutations are associated with disturbances in sleep-wake cycle as in fatal familial insomnia (FFI) [53]. This comparison suggests that mutations could possibly influence protein mis-folding and the conformations amyloid aggregates adopt, where variations in structure result in distinct pathologies, or strains of disease. Recently, a number of studies have provided evidence that a 'prion-like' self-propagating mechanism could be applied to a wide range of disease associated with protein mis-

folding, including Aβ, tau, α-synuclein, huntingtin with polyQ repeats [54], superoxide dismutase 1 (SOD1) and TDP-43 [55]. At least two distinct strains of Aβ prions can be discerned in the brains of AD patients and were able to maintain strain fidelity after serial passages in mice; incidentally, both of these strains resulted in CAA [56]. Sold-state NMR data has demonstrated the presence of distinct fibril structures that arise when Aβ40 is seeded with brain extract from phenotypically distinct forms of sAD (rapidly progressive vs typical prolong-duration) [57]. This suggest that amyloid heterogeneity is not solely due to mutations and in the case of Aβ, strains can arise from the same peptide sequence.

Studies with microtubule associated protein tau (MAPT) have shown that minute amount of preformed aggregate was sufficient to initiate robust conversion of normal proteins into tau aggregates; furthermore, in vivo inoculations of MAPT seeds often results in time-dependent spreading of pathology to synaptically connected distant brain regions [58,59]. The relationship between amyloid deposition and neurofibrillary tangle formation was a central issue in the pathogenesis of AD. It has been convincingly shown that fibrillar Aβ, but not soluble Aβ, induces the phosphorylation of MAPT that results in the accumulation of paired-helical-filaments (PHF) of MAPT that is incapable of binding microtubules [60]. The interaction between Aβ and MAPT, specifically the conversion of normal to pathogenic status, has been recapitulated with a number of amyloidogenic proteins including: α-synuclein (α-syn) and islet amyloid precursor protein (IAPP) and begs the question as to whether other seemingly soluble proteins could become pathogenic after interactions with Aβ aggregates [61,62] .

Insights from conformation-dependent antibodies and the epitopes they recognize.

The epitope that an antibody recognizes on the primary amino acid sequence can be categorized into one of two classes: continuous or discontinuous. In both categories the three dimensional structure is paramount and influences the spatial organization of amino acids that participate in the protein or aggregate's antigenic epitope [63]. Epitopes that are continuous tend to localize with secondary structures that are loops or protruding regions of the protein structure [64]. Conversely, antigenic epitopes that are discontinuous favor the β-strand secondary structure, are in high packing density regions in tertiary protein structure, and tend to make poor antigenic determinate for natively folded proteins because they normally hidden [65]. For simplicity, an antibody that recognizes a continuous epitope is referred to as sequence dependent and one that recognizes a discontinuous epitope is referred to conformation dependent. The Alzheimer's research field is coalescing around the hypothesis that conformation dependent antibodies, specifically those directed towards the various epitopes generated by β-stands and β-sheet stacking, are powerful tools to study and treat pathogenic conformations of mis-folded protein.

Before the use of conformation dependent antibodies, the determination of the conformation status of a mis-folded protein solely relied on biochemical approaches, such as: characterizing its solubility or by the size of the aggregate according to size exclusion chromatography and gel electrophoresis. The importance of conformational diversity adopted by amyloid was highlighted when it was discovered that independent of the specific sequence of the aggregating protein, both oligomers and fibrils display common or generic epitopes that define one from the other [66,67]. Unexpectedly, a defining feature of this class of antibody was their ability to recognize

aggregates formed by different types of amyloid associated protein, including MAPT, IAPP, polyglutamate (polyQ), α-synuclein, and PrP. The lack of sequence specificity indicate that conformation-dependent antibodies may recognize three-dimensional epitopes, such as: a specific turn or hydrogen-boding motif (e.g. steric zipper) on the polypeptide backbone that does not occur in the native protein structure or ordered side chain arrays that run perpendicular to the β-strands [68]. Furthermore, conformation-dependent antibodies provided evidence for the generalization that amyloid aggregates that share common epitopes also share a common mechanisms of pathogenesis and thus provide the opportunity to develop therapeutics for an array of disease [69].

Conclusion

Here I address a knowledge gap that exist in attributing conformational diversity in amyloid structure to specific AD pathology. Specifically, I described the pathological significance of a immunologically distinct Aβ epitope or conformation in CAA and AD. Studies included: determining the spatial and temporal distribution of vascular amyloid recognized by a monoclonal antibody against fibrillar Aβ (mOC31), understanding the relationship between vascular amyloid and α-actin immunoreactivity and exploring the inflammatory environment around mOC31-immunoreactive vessels. Lastly, I utilized *in vitro* cultured human primary brain vascular smooth muscle cells (HBVSMC) as a model to elucidate the mechanism of Aβ-induced pathology. This dissertation presents the findings of these investigation in three sections: (1) generation of monoclonal antibodies against fibrillar Aβ and the characterization of a unique conformation of vascular amyloid in human and transgenic (Tg) mouse brain, (2) pathological

significance of vascular amyloid recognized by mOC31 in human and Tg-mouse brain, and (3) mechanisms of pathogenicity in an *in vitro* human brain smooth muscle primary cell culture model.

CHAPTER 1

Generation of monoclonal antibodies against prefibrillar and fibrillar Aβ and the characterization of a unique conformation of vascular amyloid in AD and transgenic (Tg) mouse model of AD brain

Introduction

Development of disease modifying therapeutics is hindered by the lack of a commonly understood mechanism for AD pathogenesis which is complicated by increasing evidence that amyloids, like Aβ, are structurally diverse [70,71]. There are at least 2 structurally distinct classes of amyloid aggregates that can be generalizable, including prefibrillar aggregates and fibrillar aggregates. Conformation dependent antibodies can detect these structures by the exposure or masking of epitopes that are unique to an individual aggregation status [67,69]. Prefibrillar aggregates share structural properties with pore-forming β-barrels which have β-strands that assemble in antiparallel β-sheets and are recognized by the A11 antiserum [72]. Fibrillar aggregates are composed of parallel, in-register, hydrogen-bonded β-sheets and are recognized by the OC antiserum [73]. For many types of aggregates A11 and OC are mutually exclusive; that is A11 does not recognize amyloid fibrils or monomers and OC does not recognize prefibrillar aggregates or monomer, suggesting that they are on alternative pathways that culminate in the formation of amyloid fibrils [74]. Evidence supports that prefibrillar and fibrillar aggregates are structurally polymorphic and raises the question as to which of these structural variations contributes to disease.

We generated a panel of 29 rabbit monoclonal antibodies: 6 specific for prefibrillar aggregates (mA11s) and 23 specific for fibrillar aggregates (mOCs). We characterized the immunoreactivity of these antibodies on human and Tg-mouse models of AD brain and report that although 3 unique prefibrillar polymorphism could be identified *in vitro,* none of the mA11s appear to accumulate in detectable levels using immunohistochemistry. In contrast, 6 mOCs differentially stain intracellular and extracellular amyloid on the basis of subcellular location and plaque morphology. Specifically, mOC23 recognizes the rim or peripheral cortex of spherical "cored" plaques, while the central core is stained by mOC22. In contrast, the large and amorphous extracellular deposits elucidated by mOC1, mOC116. and several other antibodies. Furthermore, mOC78 immunoreactivity colocalizes with elevated intracellular Aβ at early times in 3XTg-AD mice and human brains. We found that mOC78 also stains neuronal nuclei at intermediate stages of plaque pathology. We conclude with the characterization of a unique conformation of vascular amyloid immunoreactivity and find that it is exclusively accumulates within brain vascular smooth muscle cells. These results highlight the structural variation present in Alzheimer's disease and support the hypothesis that these variations may contribute to disease heterogeneity.

Materials and methods

mAll and mOC antibody production

Rabbit monoclonal antibodies and were made under contract with Epitomics (Burlingame, CA) using Aβ40-colloidal gold oligomer mimics (mA11s) or fibrillar Aß42 (mOCs) as the antigen for immunizing New Zealand white rabbits, as previously described for preparing A11 and OC polyclonal serum [67,69] and, more recently, monoclonal antibodies mA11-55, mA11-205,

mOC64 and mOC87 [75,76]. For mA11s, approximately 1900 pools of hybridomas were screened against Aβ42 prefibrillar oligomers (PFOs) by ELISA using plates coated with 50nM of Aβ42 PFO, and 96 pools having an absorbance above background were selected and subjected to further aggregation state analysis against a medium density array of Aβ monomer, Aβ PFO, Aβ fibrils, α-synuclein PFO, IAPP PFO by ELISA and dot blotting. Secondary screening yielded 6 clones displaying unique immunoreactive properties: mA11-55, mA11-118, mA11-121, mA11-201, mA11-204, mA11-205. For mOCs, approximately 10,000 pools of hybridomas were screened against Aß42 fibrils, Aβ PFO or Aß monomer, and 120 pools having an absorbance at least 3-folds above background in ELISA assays were selected for further analysis. Secondary screening consisted of probing blots of a medium density array of 130 different preparations of fibrils, prefibrillar oligomers and monomers of Aβ1–42, Aβ1–40, islet amyloid polypeptide (IAPP), polyQ40, overlapping 15 residue peptide segments of Aß and amyloid-forming random peptides. A subset of hybridoma pools were also screened by immunohistochemistry on AD and age-matched control brain tissues. The medium density array screen yielded 23 clones displaying unique immunoreactive properties: mOC1, mOC3, mOC9, mOC15, mOC16, mOC22, mOC23, mOC24, mOC29, mOC31, mOC41, mOC51, mOC64, mOC76, mOC78, mOC86, mOC87, mOC88, mOC98, mOC104, mOC107 mOC108, mOC116.

Human and mouse tissue acquisition and preparation

Postmortem paraformaldehyde-fixed brain tissue was obtained from the neuropathological core of the University of California at Irvine Alzheimer's Disease Research Center (UCI ADRC). Subjects enrolled in the ADRC were given the MMSE and as standard protocol for autopsy

cases, Braak and Braak neurofibrillary tangle and plaque staging was evaluated [77]. This study examined tissues from the frontal cortex (Brodmann's Areas B9 and B11). All mouse tissue was acquired in accordance with animal protocols approved by the Institutional Animal Care and Use Committee at the University of California, Irvine. The 3XTG-AD (B6;129-Tg(APPSwe,tauP301L)1Lfa Psen1tm1Mpm/Mmjax) mice were obtained from The Jackson Laboratory [78]. Mice were housed in groups of 2 to 5 or single-housed for aggressive males, under a 12-h light/12-h dark cycle at 21 °C, with food and water ad libitum. The initial characterization by Oddo et al. found that the 3XTG-AD mice show a progressive increase in Aβ peptide deposition in AD-related areas that include the hippocampus and cortex beginning as early as 3-months, impairment of synaptic transmission and long-term potentiation at 6-months, and in addition to extracellular Aβ plaques, these mice exhibit structurally altered and hyper-phosphorylated tau at 12-months of age. At 3, 6, 12, and 14-months of age 3XTG-AD mice and age-matched controls were intracardially perfused using a peristaltic pump with approximately 120 ml of phosphate buffered saline over 10 min. Brains were isolated and one hemisphere was fixed in 4% (w/v) paraformaldehyde while the other half was micro-dissected to isolate cortex, hippocampus, and mid-brain and snap frozen in liquid nitrogen for further analysis. Paraformaldehyde-fixed human and mouse brain tissue was sectioned to 50 μm using a Vibratome Series 1000 vibrating microtome (The Vibratome Company, St. Louis, MO). Sections were stored in PBS containing 0.02% NaN_3 at 4° C for immunohistochemistry and immunofluorescence analysis.

Immunohistochemistry (IHC)

Free-floating sections were incubated in 3% hydrogen peroxide and 3% methanol in Tris-buffered saline (TBS), (20mM Tris and 137 mM NaCl, pH 7.6) for 30 minutes at room temperature (RT) to quench endogenous peroxidase activity. Non-specific background staining was reduced with a 1 hour incubation in blocking solution that consist of 2% (w/v) bovine serum albumin (BSA) (Sigma-Aldrich, St. Louis, MO) and 0.1% (v/v) Triton X-100 (Tx) (Sigma-Aldrich, St. Louis, MO) in TBS at RT. Tissues were incubated with primary antibodies diluted in blocking solution overnight at 4° C (antibody information listed in Table 1.1). The sections were then washed 2 x 5 minutes with 0.1% (v/v) Tx in TBS, blocked for 30 minutes in blocking solution, and incubated with the biotinylated secondary antibody (goat anti-rabbit or horse anti-mouse) (Vector Laboratories, Inc., Burlingame, CA) for 1 hour at RT at a concentration 10 µg/ mL in blocking solution containing 1.5% (v/v) of normal serum (Vector Laboratories, Inc., Burlingame, CA). After incubation with the secondary antibodies, the tissue sections were washed 2 x 5 minutes in 0.01% Tx in TBS and incubated in blocking solution for 30 minutes at RT. An ABC peroxidase kit and 3,3'-diaminobenzidine (DAB) substrate kit (Vector Laboratories, Inc., Burlingame, CA) was used to detect the biotinylated secondary antibodies. Following the DAB incubation, the tissue sections were washed 5 x 5 minutes in dH2O and allowed to air dry on colorfrost coated-glass slides (Fisher Scientific, Waltham, MA). The sections were then dehydrated using sequential 3 minute incubations in 50%, 70%, and 95% ethanol, followed by a 15 minute incubation in 100% ethanol and cleared in Histoclear I/II for 5 minutes (National Diagnostics, Atlanta, GA). The sections were then mounted, cover slipped with DePeX (EMS, Hatfield, PA), and visualized using an Olympus BH-2 light microscope (Olympus America Inc.,

Center Valley, PA). The omission of either the primary or the secondary antibody was used as the negative control and resulted in no DAB staining.

Immunofluorescence (IF) and confocal microscopy

Free-floating sections were washed with TBS, permeabilized in 0.1% (v/v) Tx in TBS for 30 minutes and incubated in blocking solution for 1-hour at RT. Human and mouse sections were then co-labeled with primary rabbit antibody (e.g. mA11-55, mOC31, mOC78) and a mouse antibody (e.g. anti-Aβ(4G8), anti-Aβ(6E10), anti-α-actin (1A4)) in blocking solution overnight at 4° C (antibody information listed in Table 1.1). After washing 3 times for 5 minutes in TBS with 0.1% Tx, and incubation in blocking solution with 1.5% (v/v) normal goat serum for 1 hour, primary antibodies were detected with 10 μg/mL of highly cross-absorbed goat-anti-rabbit and goat-anti-mouse secondary antibodies coupled to Alexa Fluor 488, 555 or 647 dyes (Invitrogen, Thermo Fisher Scientific) for 1-hour at RT. When probing with antibodies from identical species (e.g. mOC78/APP-CTF), one monoclonal antibody was biotinylated and detected using streptavidin conjugated to Alex Fluor 488, 555, or 647 dyes (Invitrogen, Thermo Fisher Scientific) after detection of non-biotinylated primary antibody and blocking with 10x excess of normal IgG of primary antibody species (e.g. rabbit IgG). Selected sections were counter stained with 1% Thioflavin-S, a well-established stain for β-sheet stacking in amyloids (Sigma-Aldrich, St. Louis, MO) for 8 minutes, followed by 80% ethanol for 8 minutes twice, 95% ethanol once, and three washes with dH2O. Confocal micrographs were acquired using a Leica TCS SP8 confocal microscope (Leica Microsystems Inc., Buffalo Grove, IL) using a 20x (NA=0.75) or 63× objective (NA=1.40).

M78 correlation with AD pathology and statistical analysis

M78 positive nuclei in the hippocampal region (CA1) of 3, 10, 12 and 14 month 3XTG-AD and wild type mice or in the frontal cortex of human brains were manually counted from confocal microscopy images. 6 to 8 (317.3 μm × 317.3 μm) fields were analyzed from at least 3 independent experiments and the average counts/mm2 were plotted against different ages in mice or against the Braak and Braak Plaque Stage in humans, considering plaque stage 0 = no AD pathology; plaque stage A–B = intermediate pathology/intermediate area of plaque deposition; plaque stage C = late AD pathology/high plaque area. For the analysis that combined subjects enrolled in the ADRC and subjects participating in the The 90+ Study, the area fraction occupied by OC plaques was obtained from immunohistochemical staining of the frontal cortex of 47 subjects and 6 (500 μm × 500 μm) fields per subject were analyzed. Three major categories were defined based on the OC area fraction and represented by low (<1%, average OC counts per mm2 ± SEM = 144.3 ± 24.0, n = 15), intermediate (1–10%, average OC counts per mm2 ± SEM = 673.15 ± 84.3, n = 12) and high (> 10%, average OC counts per mm2 ± SEM = 900.0 ± 55.8, n = 20) OC immunoreactivity. Based on this classification, the average counts per mm2 of M78 positive nuclei in the frontal cortex of each subject were plotted against the OC plaque area fraction. All measurements were performed using the free Java image processing program (ImageJ). Statistical analysis was performed using OriginPro 8 (OriginLab Corp., Northampton, MA). Statistical differences between groups were determined by One-way ANOVA followed by Bonferroni's post-hoc comparisons tests.

Samples containing Aβ-hairpin motif and Dot blot analysis

Aβ-hairpin samples: LVF-FT and LVF were previously described and characterized by the lab of James Nowick [79,80]. 1 µl of a serially diluted sample was applied to Whatman nitrocellulose membrane (GE Healthcare, Pittsburgh, PA) and allowed to air dry, blocked with 5% non-fat milk in Tris-buffered saline (TBS) containing 0.01% Tween 20 (TBS-T), at room temperature for 1 hour, washed three times for 5 min each with TBS-T and incubated overnight at 4°C in blocking solution containing protein-A purified mOC31 IgG (0.1 µg/ml) or hybridoma media (diluted 1:50 in blocking solution). The membranes were then washed three times for 5 min each with TBS-T, placed in blocking solution for 1hour, then incubated with horseradish peroxidase-conjugated anti-rabbit IgG (Vector Laboratories, Inc., Burlingame, CA) diluted 1:10,000 in blocking solution and incubated for 1 hour at room temperature. After the application of detection antibody, blots were washed three times with TBS-T and developed with enhanced chemiluminscence (ECL) protocol (GE Life Sciences, Pittsburgh, PA). Membrane micrographs were obtained by exposing membranes to Amersham Hyperfilm ECL (GE Health Bio-Sciences, Buckinghamshire, UK) or using a Nikon D700 (Nikon Inc., Melville, NY) camera as described in [81].

Antibodies used in IHC and IF

The antibodies used in this chapter and the working concentrations are listed in Table 1.1

Table 1.1: List of antibodies used in Chapter 1

Antibody	Epitope/Immunogen	Source	Type	Working Dilution	Application
mA11 (e.g. mA11-55, mA11-205)	Prefibrillar Oligomer Aβ	Glabe Lab	Rabbit	1 µg/mL	IHC
mOC (e.g. mOC31, mOC78)	Fibrillar Aβ	Glabe Lab	Rabbit	1 µg/mL	IHC, IF

Antibody	Epitope/Immunogen	Source	Type	Working Dilution	Application
APP-CTF	c-terminus APP (751-770)	Glabe Lab	Rabbit	1:200	IF
Aβ (6E10)	1-16 of Aβ	Covance	mouse	5 µg/mL	IHC, IF
Aβ (4G8)	18-22 of Aβ	Sigma	mouse	1 µg/mL	IHC, IF
Aβ40 (D8Q7I)	c-terminus Aβ40	Cell Signal	rabbit	1:200	IF
Aβ42 (D3E10	c-terminus Aβ42	Cell Signal	rabbit	1:200	IF
MOG (D10)	176–247 of MOG of human origin	Santa Cruz	mouse	1:100	IF
NeuN	Purified cell nuclei from mouse brain	Millipore	mouse	1:100	IF
α-actin SMC (1A4)	n-terminus of smooth muscle α-actin	Sigma	mouse	1 µg/mL	IHC, IF
CD31		Abcam	mouse	5µg/mL	IF
GFAP	Purified GFAP from porcine spinal cord	Millipore	mouse	2 µg/mL	IF
NG2	Cell line expressing a truncated form of NG2	Millipore	mouse	2 µg/mL	IF
Collagen IV	Purified pepsin fragments of type IV collagen from human kidney	DakoCytomation	mouse	1:50	IHC, IF
Cathepsin D	Human liver cathepsin D	Sigma	mouse	2 µg/mL	IF
Rab5	Full-length Rab5	Santa Cruz	mouse	1:500	IF
Rab7	Synthetic peptide (163-177) of human Rab7	Sigma	mouse	5 µg/mL	IF

Results

Prefibrillar oligomer specific monoclonals do not recognize extracellular plaques

A11 monoclonal antibodies (mA11s) were generated using the same strategy employed to make the A11 polyclonal serum, that is, rabbits were vaccinated with Aβ40 covalently coupled to colloidal gold particles via a carboxyl terminal thiol [69]. It was determined that 4 of the 6 clones recognized generic epitopes corresponding to PFO-forming sequences, including mA11s 55, 118, 204, and 205 (data not shown). We investigated whether the monoclonal IgGs can detect the accumulation of PFOs in AD frontal cortex. No specific staining of plaque deposits was observed

with mA11s by immunohistochemistry (Figure 1.1), this is in contrast to anti-Aβ mouse monoclonal 6E10 and consistent with the mA11 lack of immunoreactivity with amyloid fibrils. Closer examination is required to elucidate whether these oligomers are detectable in vivo, such as confocal immunofluorescence microscopy and immunoprecipitation.

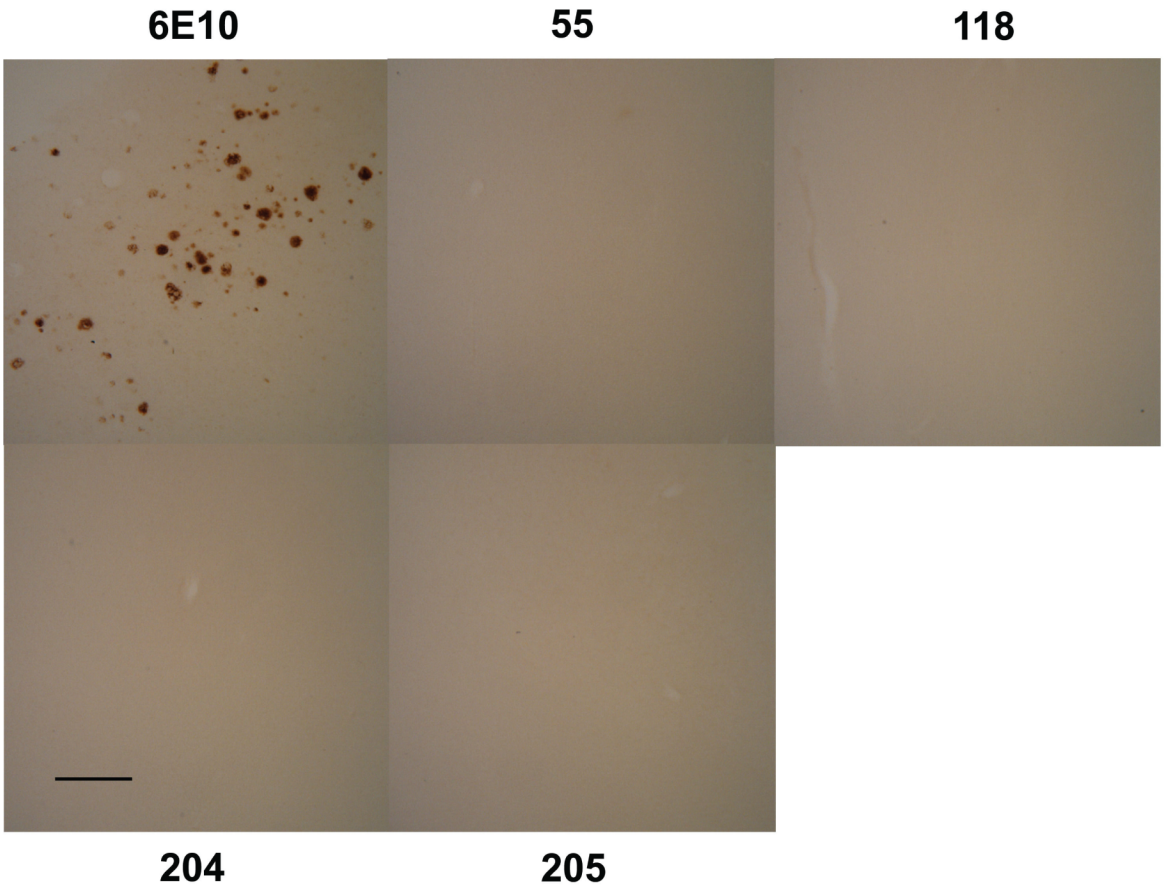

Figure 1.1 Prefibrillar oligomer specific monoclonals do not recognize extracellular plaques. Sections of the frontal cortex (Broadman's area 11) were stained with mA11-55, 118, 204, and 205; along with 6E10 as a control. The bar indicates 200 µm.

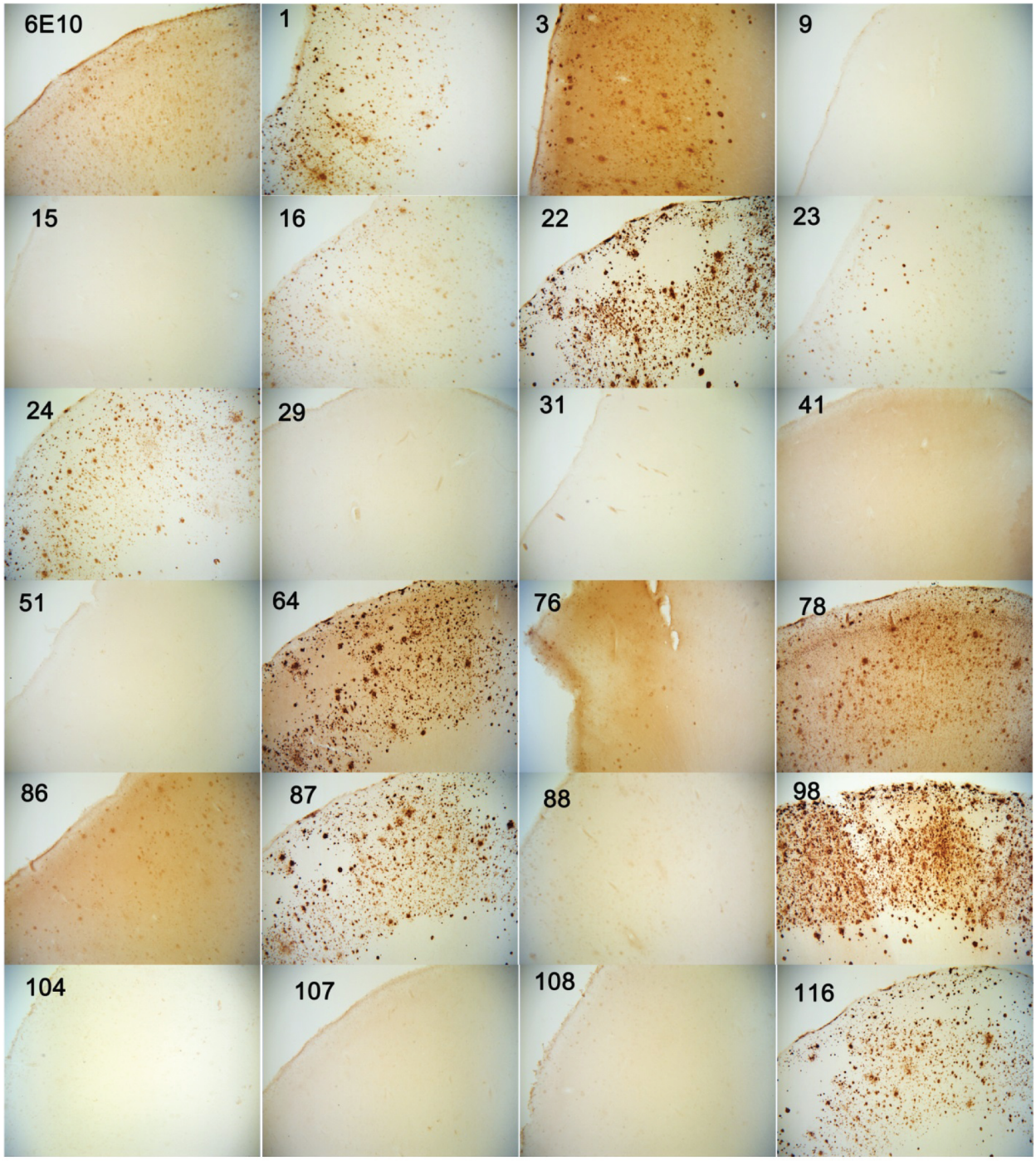

Figure 1.2 Immunostaining of human AD brain with mOC antibodies. 40 μm thick serial sections from frontal cortex (Brodman's area 11) were stained with the 23 mOC antibodies and 6E10.

Fibrillar specific monoclonals recognize distinct types of amyloid deposits in AD and transgenic mouse brain

OC monoclonal antibodies (mOCs) were generated using the same strategy employed to make the OC polyclonal serum, that is, rabbits were vaccinated with Aβ42 fibrils [67]. We selected 120 different clones from a pool of over 10,000 to be screened against a medium density array and found that 23 mOCs displayed a unique pattern of immunoreactivity in vitro (data not shown), including mOCs 1, 3, 9, 15, 16, 22, 23, 24, 29, 31, 41, 51, 64, 76, 78, 86, 87, 88, 98, 104, 107, 108, 116. We investigated whether the monoclonal IgGs can detect the accumulation of fibrillar Aβ in AD and 3xTg-AD brain. We found that the epitopes uncovered by these monoclonals fell in to three broad categories: diffuse background, intracellular deposits, and extracellular deposits (Figure 1.2). These deposits were predominately found in the grey matter of the cortical tissue examined. mOCs that presented as diffuse background on AD tissue, such as mOCs 9, 15, 29, 41, 51, 104, 107, 108 were subjected to formic acid antigen retrieval and yielded the same diffuse background pattern (data not shown). Immunohistochemistry on 3xTg-AD mouse model revealed many similarities with AD tissue samples (Figure 1.3); for example, in both AD and Tg-mouse tissues mOCs 23, and 86 exclusively recognize extracellular plaques, mOCs 1, 22, 24, 78, 86, 88, 116 recognized intracellular accumulation of Aβ in addition to extracellular plaques and mOCs 9, 15, 29, 41, 51, 104, 107, 108 presented as diffuse background. A subset of mOCs did prefer intracellular amyloid in the 3xTg-AD mouse model when compared to AD tissue sections, including mOCs 3, 16, 64, 76, 87 and 98.

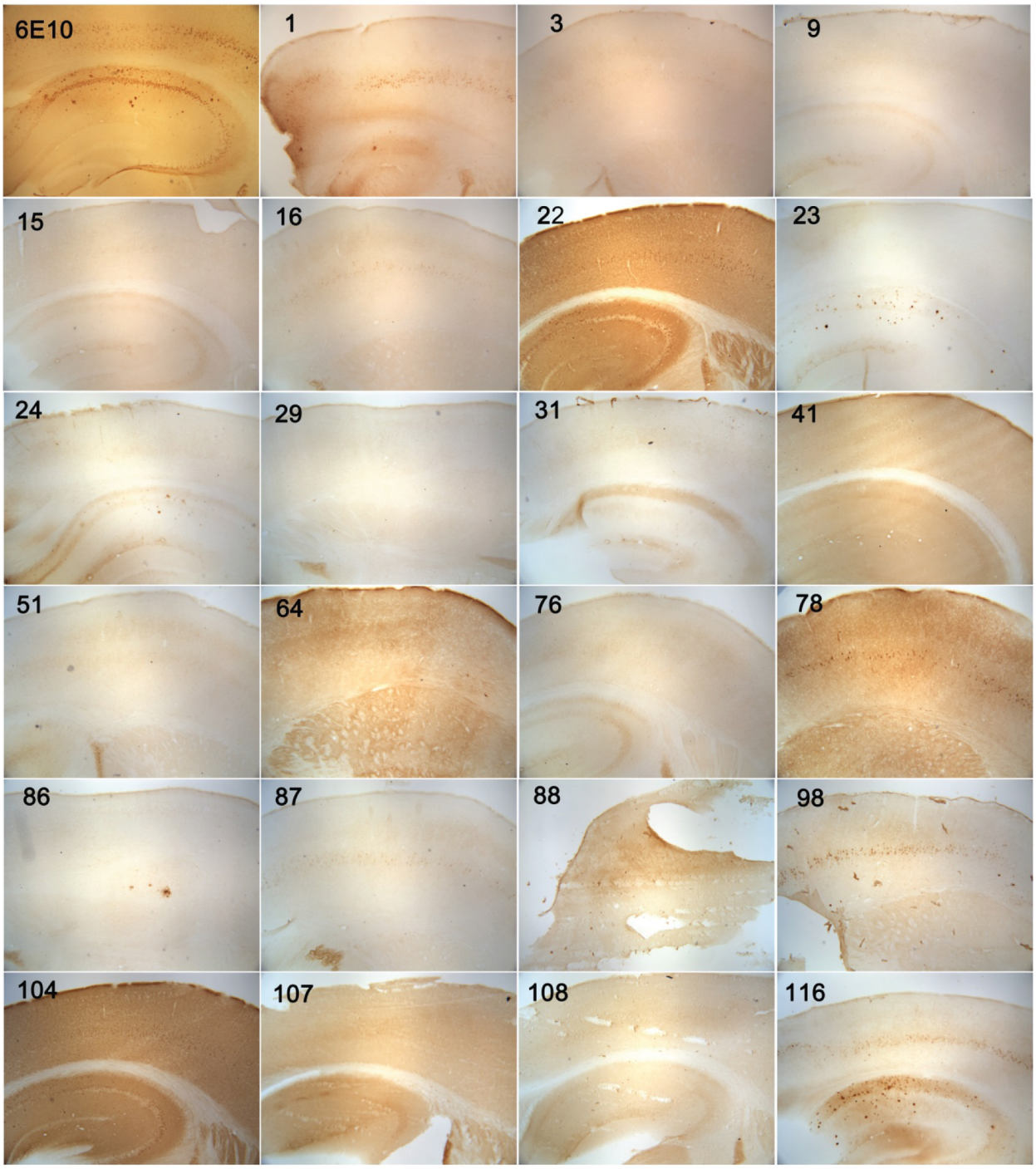

Figure 1.3 Immunostaining of 3XTg-AD brain with mOC antibodies. 40 μm thick serial sections from 14m 3xTg-AD mice were stained with the 23 mOC antibodies and 6E10.

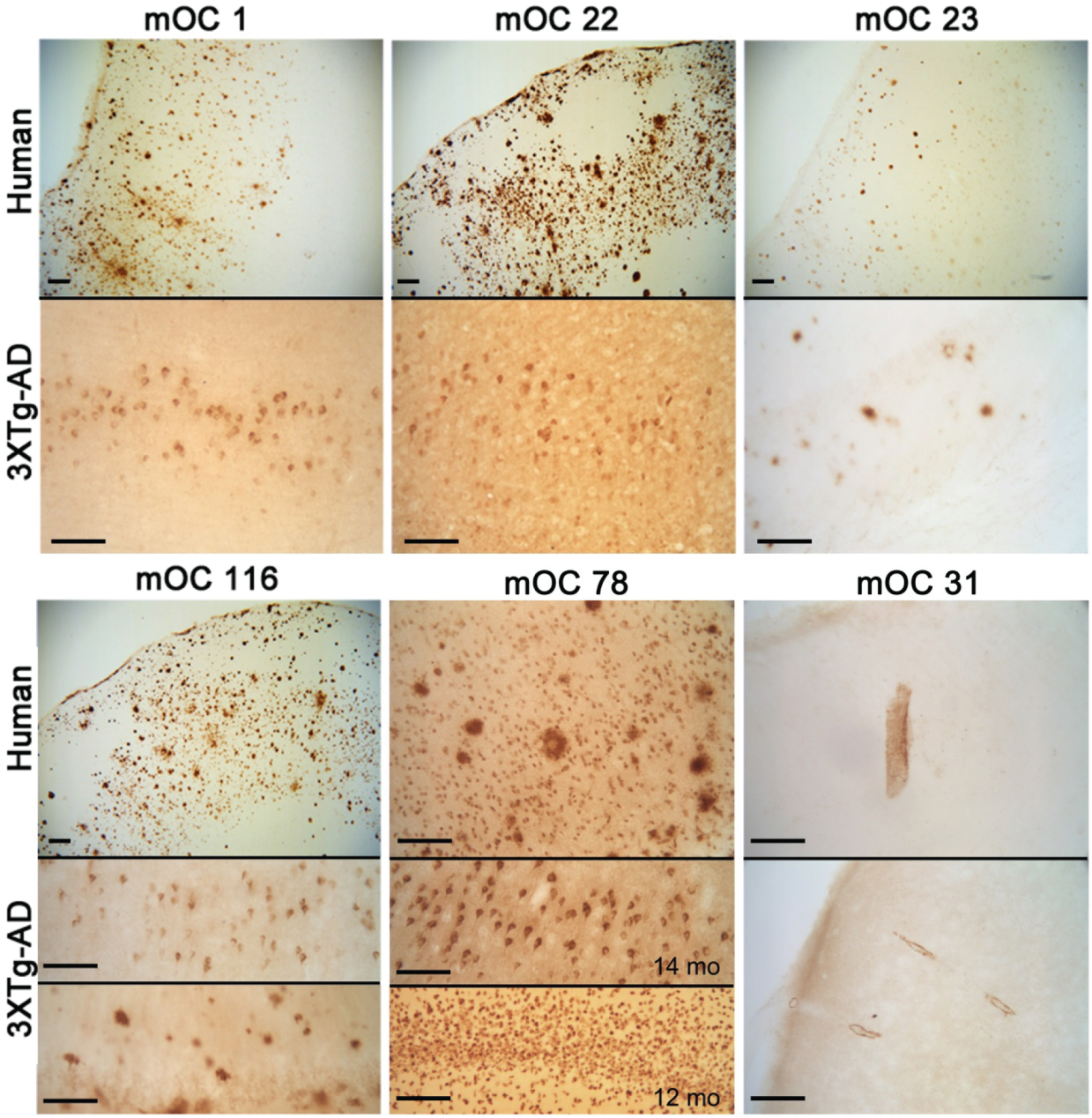

Figure 1.4 Differential staining of human AD and 3XTg-AD mouse brain. Sections were stained with the indicated mOC antibodies. Top panels: human AD brain. Bottom panels: 14 mo. 3XTg-AD mouse brain, except as indicated. Bars = 100 μm.

We examination the mOCs and found that a number of them identified morphologically and spatially unique types of amyloid deposits, including mOC1, mOC22, mOC23, mOC116, mOC78, and mOC31 (Figure 1.4). For example, extracellular plaques are recognized by mOCs 1, 22, 23, 116, and 78, but the deposits elucidated by these antibodies are morphologically

distinct. Specifically, mOCs 1, 22, and 78 recognize amorphous deposits that occupy a larger surface area than mOC23; the deposits recognized by this mOC are smaller and spherical in morphology. The heterogeneity of Aβ aggregates is not exclusive to extracellular deposits; intracellular deposits recognized by mOC1, 22, 78 116 are differentiated spatially. In both AD and 3xTg-AD mouse model mOC78 recognizes intracellular Aβ that accumulates in the nucleus of brain cells. Furthermore, the deposits recognized by mOC31 are unique from all the aforementioned antibodies; this epitope is not present in parenchymal amyloid and is exclusively found in brain vasculature.

M78 stains nuclei at intermediate stages of amyloid plaque deposition in AD brains

Intrigued by the unique spatial distribution of mOC78 in brain cells uncovered in secondary screening we investigated the temporal accumulation of nuclear amyloid in human brains using Braak and Braak plaque staging as a proxy for the temporal progression of disease. We found that mOC78 stains nuclei in a subset of human brains that have neurons with intracellular amyloid positive for anti-Aβ (6E10) (Figures1.5-a,b). In addition to neurons, the astrocytes and oligodendrocytes in these sections also have nuclei that were immunoreactive with mOC78 (Figures1.5-c-e). Astrocytes and oligodendrocytes mOC78 immunoreactivity differs from neurons in that they do not have anti-Aβ (6E10) immunoreactivity peripheral to the nucleus. Double label confocal immunofluorescence microscopy of the same samples in Figures1.5-a and b shows that neurons with elevated anti-Aβ (6E10) immunoreactivity also contain mOC78 positive nuclei (Figure 1.5-f).

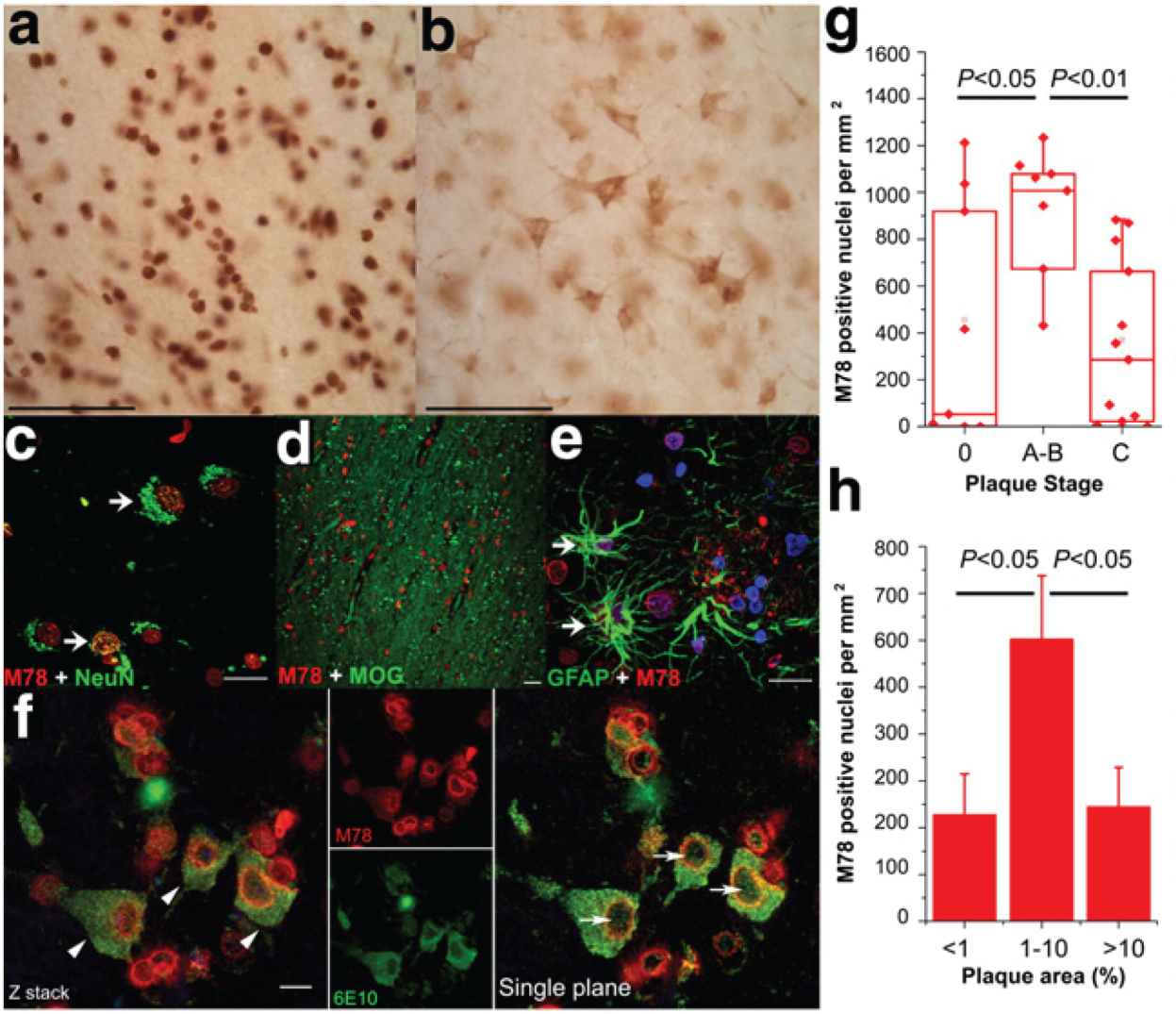

Figure 1.5 Intranuclear M78 immunoreactivity in human brain and correlation with plaque pathology. (a, b) Adjacent sections from the Broadman's B11 region were stained with M78 (a) or 6E10, (b). Bar = 100 µm. (c–e) Triple label immunofluorescence staining with M78 (red) and (c) NeuN (green), (d) myelin oligodendrocyte glycoprotein (green), or (e) glial fibrilliary acidic protein (GFAP), (green) and chromatin (DAPI, blue). Arrows point to co-localization of M78 and specific cell markers. Bar = 20 µm. (f), Double label immunofluorescence staining with M78 (red) and 6E10 (green). The arrows point to cells with neuronal morphology that stain for both M78 and 6E10. Bar = 20 µm. (g) M78 nuclear immunoreactivity correlates with intermediate stages of plaque area deposition (stage A and B) in the frontal cortex of subjects from the ADRC cohort. (h) Average counts per mm2 of M78 positive nuclei in the frontal cortex of the combined ADRC and The 90+ study subjects are plotted against the OC positive plaque area fraction. The bars indicate the values of mean ± SEM. Bar = 20 µm.

We examined two cohorts of cortical tissue samples and quantified the density of mOC78 nuclear immunoreactivity with respect to plaque stage. The first cohort consisted of 28 brains

Table 1.2: ADRC cohort

Subject ID #	Age	Sex	PMI	NPDx1	Tangle Stage	Plaque Stage	MMSE
11-02	91	F	4.82	Normal (MBC)	4	0	29
41-08	96	M	3.58	Normal (MBC)	2	0	29
15-02	88	F	5	Normal	2	0	29
09-06	112	F	3.5	Normal (MBC)	4	0	28
03-00	87	F	4.5	Normal	1	0	28
09-03	81	M	6.4	Normal (MBC)	2	0	27
35-08	94	M	3.87	Normal (MBC)	1	0	27
06-03	84.5	M	6.3	SDC	3	0	22
47-97	71	M	4.9	Normal	1	A	/
29-09	83	F	5.25	Normal (MBC)	4	A	30
07-03	84	F	4.25	Normal (MBC)	3	A	29
06-11	83	M	3.42	Normal (MVC)	5	C	24
12-03	81	F	7	SDC	5	C	23
03-03	79	M	3.5	AD	5	B	/
62-98	81	M	5	AD	5	B	12
09-01	82	F	6.6	AD	6	B	4
17-01	81	F	4.3	AD	5	B	0
34-99	77	F	5.4	AD/LBD	4	B	0
19-06	59	M	3.3	AD	6	C	/
05-09	57	F	3.17	AD	6	C	2
10-02	77.5	M	4.5	AD	4	C	19
10-11	90	F	6.58	AD	6	C	13
19-03	77	M	5	AD	6	C	11
25-10	57	F	3.17	AD	6	C	11
01-06	63	M	5.8	AD	6	C	10
14-03	76	M	3.75	AD	6	C	6
10-10	63	F	2.93	AD	6	C	2
04-02	83.2	M	3.5	AD	6	C	0

Table 1.3: 90+ cohort

Subject ID #	Age	Sex	PMI	NPDx1	Tangle Stage	Plaque Stage	MMSE
19-09	95–99	M	5.50	Normal (MBC)	3	0	29
21-07	95–99	F	5.50	Normal (MBC)	2	0	29
23-09	100 +	F	20.80	Normal (MBC)	2	0	25
27-06	90–94	M	6.80	Normal (MBC)	1	0	26
29-07	95–99	M	34.10	LBD	2	0	6
26-04	90–94	F	4.50	CBD	3	0	4
33-06	95–99	F	3.00	Normal (MBC)	2	0	4
23-07	95–99	F	7.70	Normal (MBC)	2	A	11
25-08	100 +	F	4.00	Normal (MBC)	2	A	16
30-06	95–99	F	1.00	Normal (MBC)	3	A	26
37-06	95–99	M	3.50	Normal (MBC)	3	A	17
03-07	95–99	F	3.80	AD	5	B	29
06-06	100 +	F	3.40	AD	5	B	17
24-07	95–99	M	14.50	AD	5	B	28
28-08	95–99	M	4.70	AD	5	B	18
37-05	100 +	F	3.90	AD	5	B	29
02-08	95–99	F	5.10	AD	5	C	21
06-08	95–99	F	5.30	AD	6	C	0
27-07	95–99	F	4.10	AD	6	C	0
28-07	95–99	F	4.10	AD	6	C	25
37-08	95–99	F	5.40	AD	6	C	0

and the second was made up of 21 brains that were both obtained from the UC Irvine Alzheimer's Disease Research Center (ADRC) brain bank. The first group consisted of 12 cognitively normal individuals with mini mental state examinations (MMSE) scores ranging from 23 to 30, 15 AD individuals with MMSE scores 0-19 and one individual with senile dementia changes with MMSE score 22 (Table 1.2). Analysis of this cohort revealed that mOC78 immunoreactivity is correlated with with Braak and Braak plaques stages A and B, compared to

stage 0 (p<0.05) or stage C (p<0.01), suggesting that nuclear amyloid is associated with early disease progression (Figure 1.5-g). No significant correlation was observed between mOC78 positive nuclei and tangle stage or MMSE. The second group consisted of 21 brains from subjects that were older than 90 years (Table 1.3). This cohort consisted of samples that were selected on the basis of histopathological and psychometric classifications as non-demented with insufficient pathology to qualify for a classification of AD (NDIP), non-demented with AD pathology (NDAP), demented with insufficient pathology (DIP) and demented with AD pathology (DAP). Although no statistically significant correlation between mOC78 positive nuclei and plaque stage, tangle stage or MMSE was observed in this cohort, combined analysis of the samples from the ADRC and the 90+ cohorts on the basis of the total amyloid plaque area stained by OC showed that mOC78 positive nuclei are significantly elevated in samples that contain an intermediate amount of plaque area (1-10%) compared to no plaques (<1%) or high plaque area (>10%) (p< 0.05) (Figure 1.5-h). This suggests that mOC78 positive nuclei are abundant at early phases of plaque deposition and decline with increasing plaque area.

Intraneuronal and nuclear amyloid fibril immunoreactivity accumulates in 10–12 month 3xTg-AD mice

In human samples Braak and Braak plaque staging provided a proxy for disease progression. We decided to investigate more directly the temporal relationship between mOC78 nuclear amyloid accumulation and disease progression in aged 3xTg-AD mice. We found that at 3 months Tg-mice have elevated anti-Aβ (6E10) immunoreactivity in a subset of neurons in CA1, but no mOC78 immunoreactivity was observed (Figure 1.6-a). At 10 months, the Aβ immunoreactivity

colocalizes with the fibril specific mOC78 immunoreactivity in neurons (Figure 1.6-b), which suggest that accumulation of intracellular Aβ or APP precedes its mis-folding in neurons. At 12 months, the mOC78 immunoreactivity is predominately nuclear (Figure 1.6-c), with trace amounts still localized with anti-Aβ(6E10) in the perinuclear space. The presence of nuclear and

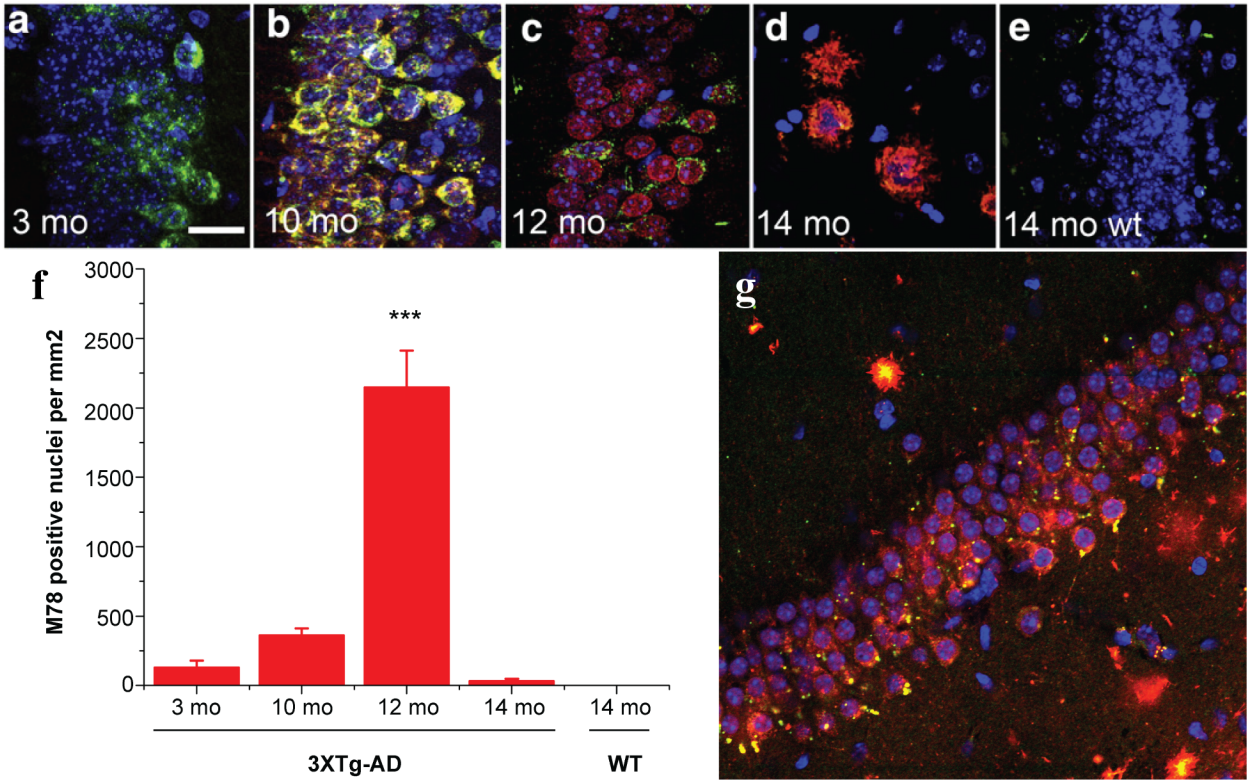

Figure 1.6 mOC78 labels intracellular amyloid and nuclei at intermediate times in 3XTg-AD and 5XFAD-Tg mice. (a) At 3 months, a subset of neurons exhibit elevated perinuclear anti-Aβ(6E10) staining, but no mOC78 immunoreactivity is observed. (b) At 10 months, mOC78 immunoreactivity (red) is primarily perinuclear and colocalized with anti-Aβ(6E10) (green) in neurons. Nuclei are labeled with DAPI (blue). (c) At 12 months, the mOC78 staining is primarily nuclear and is surrounded by anti-Aβ(6E10) and mOC78 immunoreactivity in neurons. (d) At 14 months, mOC78 staining is primarily restricted to plaques that stain weakly with anti-Aβ(6E10). (e) No anti-Aβ(6E10) or mOC78 staining is observed in 14 month wild type brain. (a–c, e), CA1. (d), stratum oriens adjacent to CA1. (f) Time course analysis of mOC78 nuclear immunoreactivity in the CA1 region of 3XTg-AD mice at 3, 10, 12 and 14 months and 14 month wild type. mOC78 nuclear immunoreactivity is significantly elevated in 12 month-old 3XTg-AD mice as compared to other age groups. The bars indicate the values of mean ± SEM (*** $p < 0.001$ vs 3 month, 10 month, and 14 month 3XTg-AD and 14 month WT). (g) Confocal fluorescence image of 6 month 5XFAD-Tg mouse brain showing CA1 of the hippocampus stained with mOC78 (red), anti-Aβ(4G8) (green) and DAPI (blue). The neuronal nuclei are stained by mOC78. Bar = 20 μm.

pernuclear amyloid is no longer detectable at 14 months and is replaced with immunoreactivity associated with extracellular plaques (Figure 1.6-d). A majority of mOC78 plaques are weakly immunoreactive for anti-Aβ (6E10), even after the application of antigen retrieval methods for plaque staining by anti-Aβ (6E10). 14 month wild type mice were absent of mOC78 immunoreactivity (Figure 1.6-e). Changes in mOC78 nuclear immunoreactivity as a function of age in the CA1 region of 3xTg-AD and wild type mice were quantified and summarized in Figure 1.6-f. The quantifications qualify our observations and show a significant increase in the counts per mm^2 of mOC78 positive nuclei in 12 month 3xTg-AD mice. Similar nuclear mOC78 immunoreactivity was observed in 6 month 5XFAD mice (Figure 1.6-g), proving evidence that intranuclear amyloid is not unique to the 3xTg-AD mouse.

Characterization of a unique conformation of vascular amyloid immunoreactivity

We found in our initial characterization of mOCs that a number of morphological distinct epitopes for amyloid are present in human and Tg-mouse brain. While many epitopes were associated with amyloid deposits in parenchymal tissue, mOC31 immunoreactivity specifically localized to non-parenchymal cells in brain tissue. mOC31 recognizes a linear and discontinuous epitope that corresponds to residues 3-10 and 22-23 of the Aβ peptide (Figure 1.7-a). The discontinuous property of the epitope suggest that secondary structure of Aβ peptide may play a role in forming the antibodies antigenic determinant; it should also be noted that the location of this epitope is adjacent to an amino acid sequence within the Aβ peptide that, when mutated, causes HCHWA. Immunohistochemistry was carried out on serial sections of AD brain tissue with the antibodies: anti-Aβ (6E10), anti-Aβ (4G8) and mOC31. These studies demonstrate that

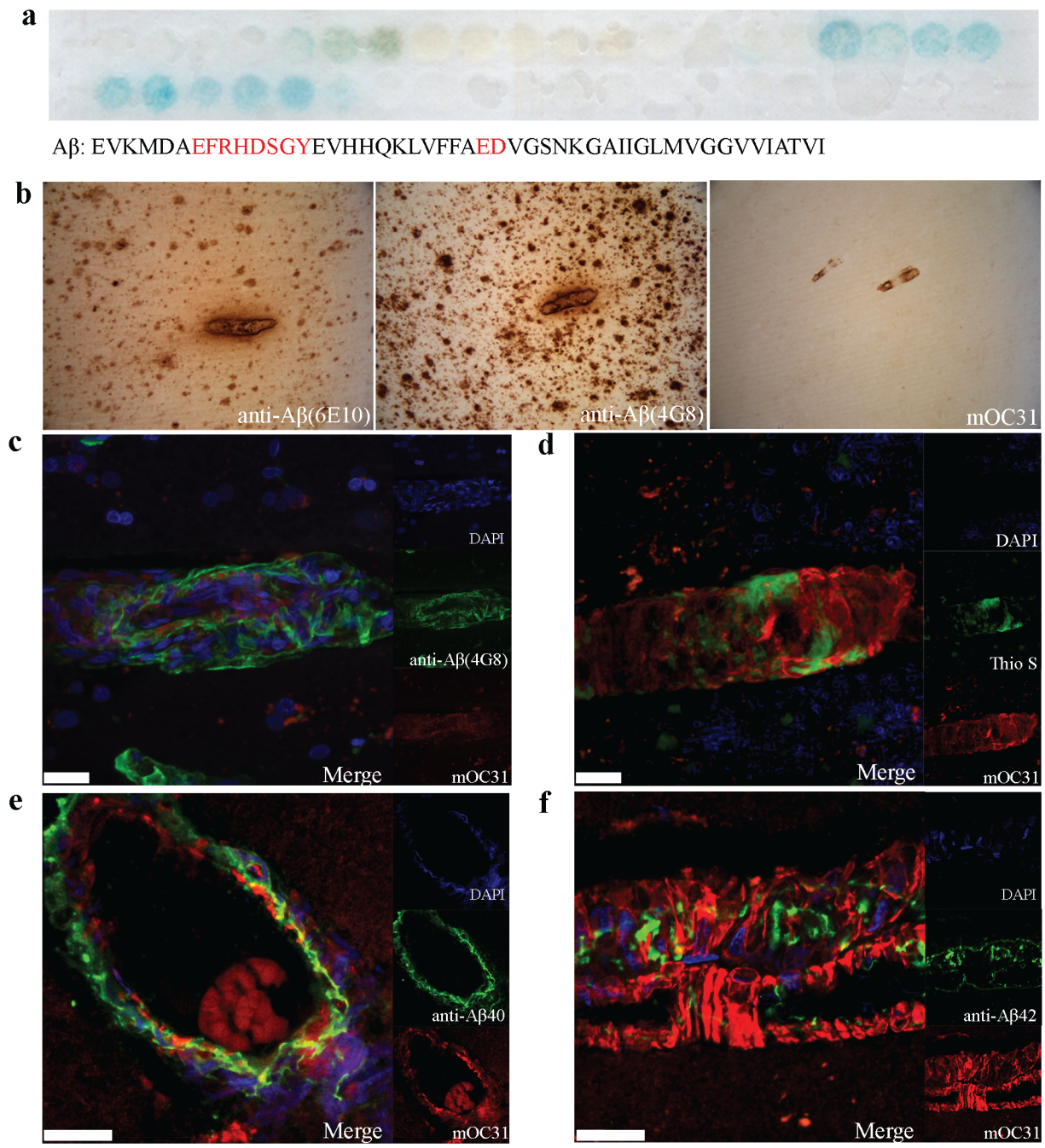

Figure 1.7 mOC31 recognizes a unique conformation of vascular amyloid. (a) Epitope mapping of mOC31 with a series of overlapping 10mer peptides of the Aβ sequence. mOC31 recognizes a discontinuous epitope of residues 3-10 and 22-23. (b) Immunohistochemistry using anti-Aβ(6E10), anti-Aβ(4G8) and mOC31 from serial sections of an AD sample laden with parenchymal and vascular amyloid. Confocal immunofluorescence of AD sample with DAPI (blue), amyloid marker (green) and mOC31 (red). Amyloid was probed with sequence specific epitopes for Aβ: (c) anti-Aβ(4G8), (e) anti-Aβ40, (f) anti-Aβ42 or with the fluorescence dye (d) Thioflavin-S. Bar = 20μm

in the presence of florid parenchymal and vascular deposits the mOC31 antibody identified only vascular amyloid (Figure 1.7-b). Furthermore, double label immunofluorescence revealed that this vascular amyloid is a subset of amyloid recognized by anti-Aβ (4G8) (Figure 1.7-c) and anti-Aβ (6E10) (data not shown). Other markers for amyloid include Thioflavin S (Thio S), which is a dye that binds to amyloid enriched with β-sheets, in these experiments mOC31 recognized amyloid that is primarily distinct from that of Thio S (Figure 1.7-d). The extensive literature citing the importance of Aβ40 to vascular amyloid (reviewed here [82]) led us to ask if mOC31 immunoreactivity was composed of Aβ40 or Aβ42. Double label immunofluorescence with c-terminal antibodies: anti-Aβ40 or anti-Aβ42, revealed that both Aβ40 and Aβ42 are associated with mOC31 and suggest that both peptides can form the antigenic determinant recognized by mOC31 (Figure 1.7-e,f). Together these observations imply that mOC31 identifies a previously uncharacterized conformation of vascular amyloid and the lack of overlap with Thioflavin S is consistent with the antibody's inability to recognize parenchymal plaques.

Vascular smooth muscle cells (VSMC) accumulate amyloid immunoreactivity

Brain vasculature is composed of number of cells, including: endothelial cells, pericytes, astrocytes, and smooth muscle cells. Since mOC31 amyloid immunoreactivity accumulated in vascular cells we investigated which cell type, if any, were specifically affected and if the amyloid was localized around the vessels. We used double label immunofluorescence to probe for vascular amyloid and a specific vascular cell type (Figure 1.8-a-d). We found a considerable amount of overlap with smooth muscle cell marker (anti-α-actin) and no colocalization with endothelial (anti-CD31), pericyte (anti-NG2), and astrocyte (anti-GFAP) markers. We also

looked at filamentous actin (f-actin) and found that mOC31 amyloid immunoreactivity also colocalized with f-actin found in smooth muscle cells (Figure 1.9-a). Localization with intracellular actin led us to ask if any of the mOC31 amyloid immunoreactivity was located

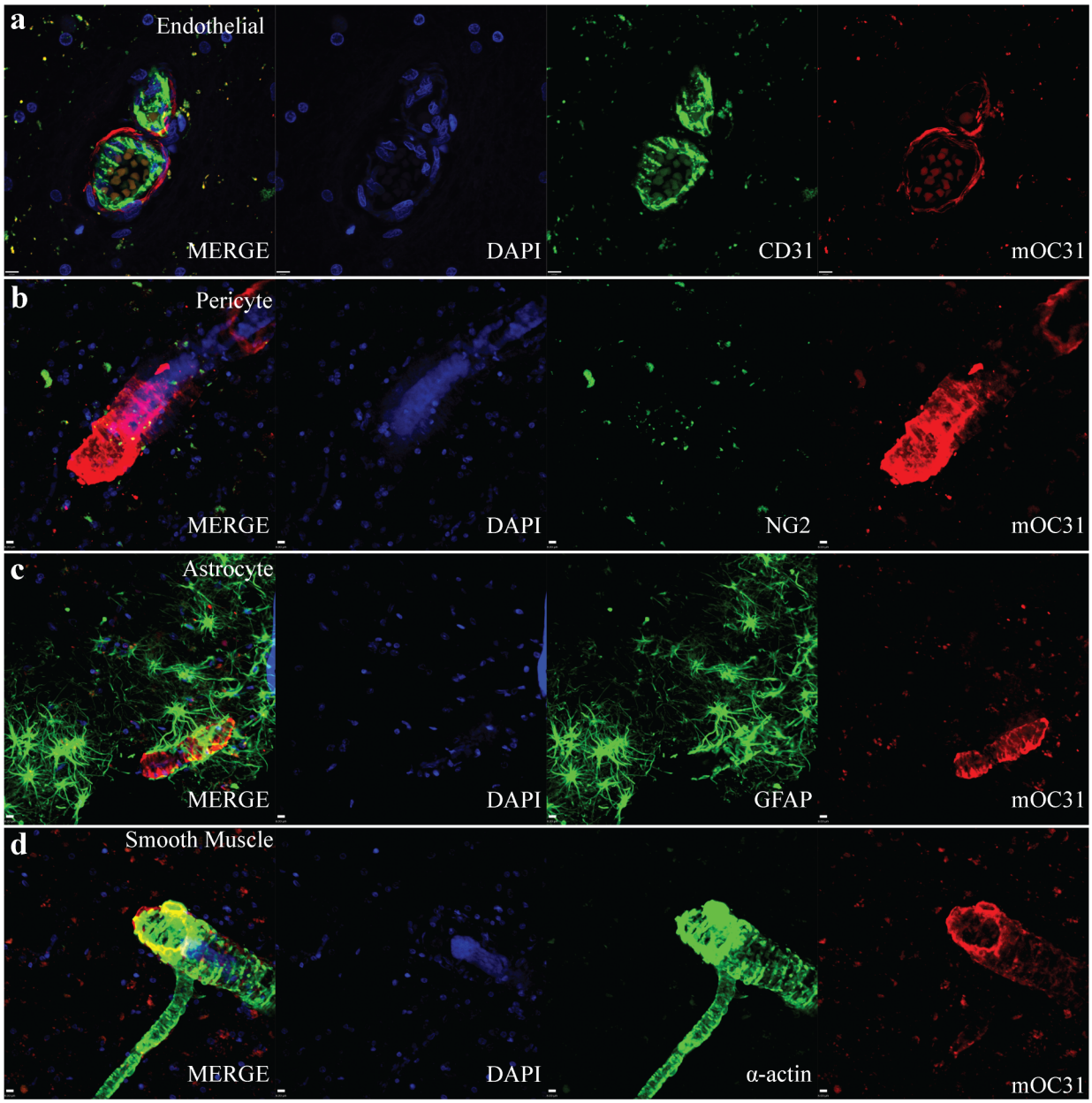

Figure 1.8 Vascular smooth muscle cells accumulate amyloid immunoreactivity. Confocal immunofluorescence of AD sample with DAPI (blue), cell-specific marker (green) and mOC31 (red). (a) Endothelia cells were labeled with anti-CD31. (b) Pericytes were labeled with anti-Neural/Glial antigen 2 (NG2). (c) Astrocytes were labeled with anti-Glial Fibrillary Acidic Protien (GFAP). (d) Vascular smooth muscle cells were labeled with anti-α-actin(1A4). Bar = 8μm

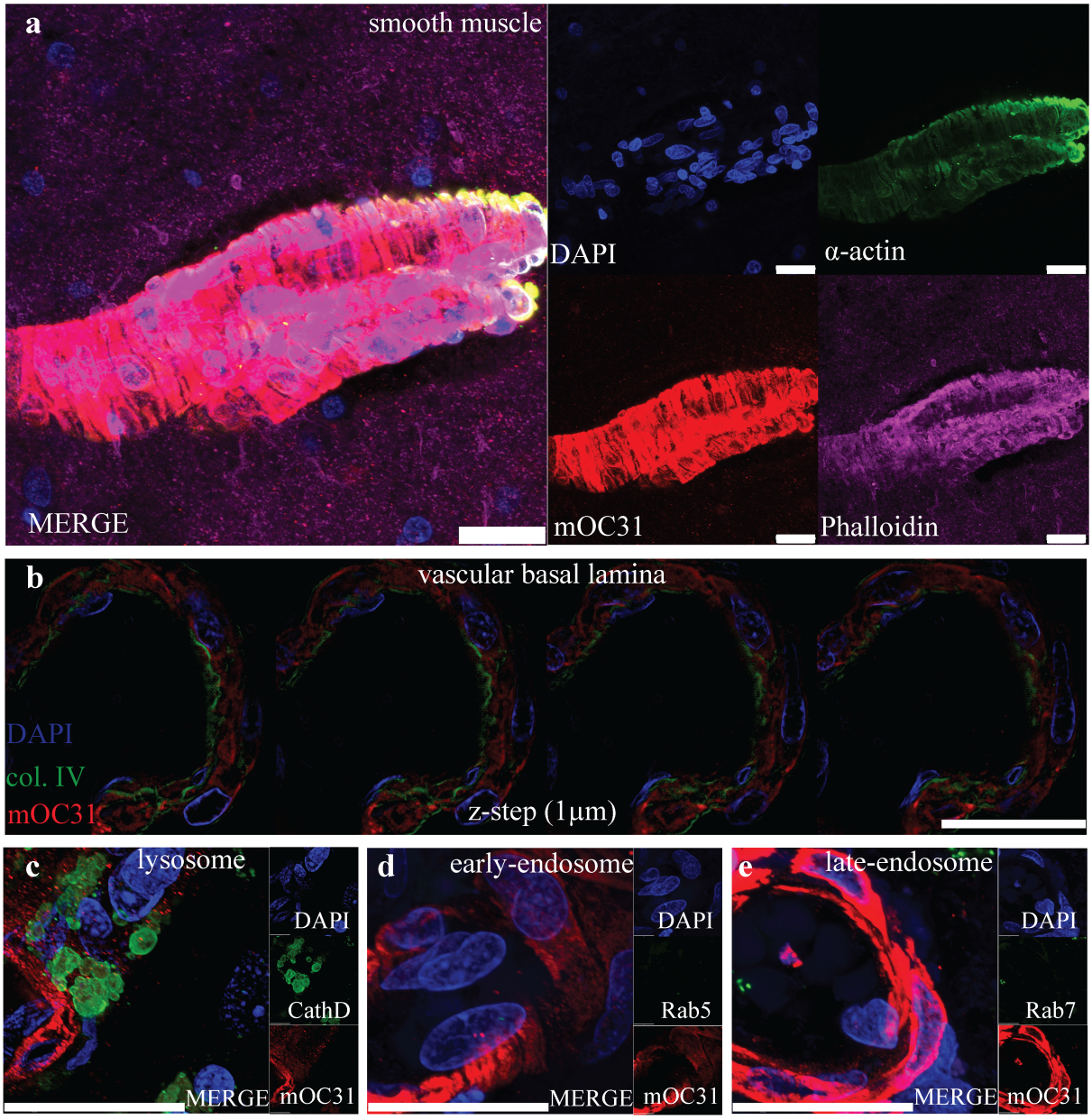

Figure 1.9 Vascular smooth muscle cells accumulate intracellular mOC31-amyloid. Confocal and super-resolution confocal, were noted, immunofluorescence of AD sample with DAPI (blue), extracellular or sub-cellular marker (green) and mOC31 (red) show mOC31 immunoreactivity inside vascular smooth muscle cells. (a) F-actin in vascular smooth muscle cells was labeled with Phalloidin. (b) Super-resolution confocal immunofluorescence with anti-collagen IV was used to examine basal lamina. (c) Lysomomes were labeled with anti-cathepsin D and (d) early- and (e) late-endosomes were labeled with anti-Rab5 and anti-Rab7, respectively. Bar = 25 μm.

outside the cell. Super-resolution confocal microscopy with the basement membrane maker (anti-collagen IV) and mOC31 showed that the amyloid immunoreactivity was intracellular (Figure 1.9-b). The amyloid immunoreactivity was also predominately cytosolic as it did not colocalize with lysosomal (anti-Cathepsin D) and endosomal (anti-Rab5 and anti-Rab7) cellular compartments in vascular smooth muscle cells (Figure 1.9-c-e). Together these results show that vascular smooth muscle cells specifically accumulate mOC31 immunoreactivity intracellularly.

Discussion

Characterization of *in vitro* aggregates have shown that significant variations in molecular structure results in distinct structural differences in fibrils as determined by solid state NMR [83]. Here we report a panel of 29 monoclonal antibodies (mAbs) and found that a subset have the ability to recognize and differentiate distinct polymorphic variants of Aβ aggregates *in vivo* (Figure 1.2 and 2.3). Surprisingly, about half of mAbs recognize molecular structures that do not deposit in brain at detectible levels or only exist *in vitro* (Figure 1.1 and mOCs: 9, 15, 29, 41, 51, 104, 107, 108). These monoclonal antibodies may be more suitable for detecting soluble aggregates in cell lysates or serum.

Deposits stained by our panel of mAbs shared properties with fibrils (mOC) and recognized either intracellular aggregates or extracellular plaques. Monoclonal OC antibodies elucidate the morphological heterogeneity that exist *in vivo* and by extension variations in molecular structure (Figure 1.4). These variations in structures are differentiated by the exposure or masking of unique epitopes, pathologic patterns that antibodies have evolved to detect. Amyloid plaques

have been shown not to correlate with disease progression and many have argued the protective nature of these extracellular deposits [23]. Here we highlight amyloid immunoreactivity by two antibodies that differentiate aggregates spatially and subcellularly *in vivo* (Figure 1.5 and Figure 1.7). mOC78 recognizes an intracellular aggregate of parenchymal cells that accumulates early, before behavioral deficits, and whose location within the cell evolves, revealing the dynamic nature of amyloid deposition in AD and the neuronal origin of plaques (Figure 1.6). mOC31 recognizes non-parenchymal amyloid that is localized exclusively in brain vascular smooth muscle cells (Figure 1.7 and 2.8). It has been shown that certain amyloid morphologies may be more pathogenic than others in the affected organs of amyloid disease [83]. Double label confocal microscopy tells us that the amyloid epitope linked to mOC31 is unique from other Aβ antibodies and the pathological significance will be the focus of Chapter 2.

CHAPTER 2

Pathological significance of vascular amyloid recognized by mOC31 in AD and Tg-mouse model of AD brain

Introduction

AD is a pervasive neurodegenerative disease that can only be diagnosed post-mortem by its two histopathological hallmarks, the accumulation of mis-folded amyloid beta (Aβ) and hyper-phosphorylated tau. It has been convincingly shown that Aβ deposition in the entire brain follows a distinct sequence in which regions are hierarchically involved. That is, amyloid propagation occurs anterograde to neural circuits; beginning with the neocortex, moving to subcortical regions that include the hippocampus, and ending in the brainstem and cerebellum (84). There are strong genetic components linking mutations at regions flanking Aβ to alterations in proteolytic processing of the amyloid precursor protein (APP) by presenilin (PS) and these cases follow Mendelian genetics for autosomal dominant genes and are referred to as early onset familial Alzheimer's disease (fAD) (85). A risk factor for the most common cause of dementia, sporadic and late-onset AD (LOAD), exists in apolipoprotein E ε4 (apoE4), where carrying just one allele increases the likelihood of getting the disease 2-4 fold by the age of 65 (86).

Cerebral amyloid angiopathy (CAA) is an often under-appreciated lesion of AD that also has a genetic component. Specifically, a subset of mutations found within the Aβ region of APP occur adjacent to residues 21 and 22 on the Aβ peptide and corresponds to the following familial forms of CAA: Dutch, Italian, Arctic, Iowa, Flemish, and Piedmont (28). Although the severity of CAA

in AD is variable, it is however, identified in 85-95% of AD brains and the leading cause of stroke because of lobar hemorrhage in elderly (34,86,87). Not surprising, APOEε4 is also a risk factor for sporadic and AD-associated CAA with an associated dose-dependent increase in deposited Aβ40 per blood vessel for those carrying the allele (48,49). Where pathogenic vascular amyloid accumulates remains contentious issue. As studies conducted by Henry Wisniewski and colleagues in the 90s highlight, CAA is associated with the secretion and accumulation of fibrillar and non-fibrillar deposits by vascular smooth muscle cells (VSMC) (88). Studies have also suggested that Aβ is internalized causing smooth muscle degeneration but the obligatory internalization remains a contentious issue (88,89). The alternative hypothesis is Aβ exerts its deleterious effects on the surface of VSMCs either through soluble Aβ that drains along perivascular spaces or by Aβ fibril assembly at the surface of smooth muscle cells (90,91). Cerebral amyloid angiopathy has been correlated with the loss of regional perfusion in transgenic mice and although these reductions may not be primarily responsible for regional neuronal cell loss, over time it may contribute to the exacerbation of pathologies (92).

Human brain samples were gathered from UCI ADRC and selected based on apoE polymorphic genotype. To address the pathological significance of mOC31 immunoreactivity we stained AD and 5XFAD Tg-mouse brain with mOC31 and characterized its spatial and temporal localization. We investigated whether mOC31 specific vascular amyloid was correlated with apoE genotype in our cohort. We also determined if mOC31-specific vascular amyloid correlated with a loss of smooth muscle actin immunoreactivity. To asses the inflammatory status associated with mOC31 immunoreactivity we probed for local and systemic inflammatory markers IL-1β and HMGB1,

respectively; we also searched for activated microglia. We found that mOC31 immunoreactivity increase with disease progression in AD and Tg-mouse models of AD. We also found that apoE genotype not only correlates with an increase in total amyloid load in vessels (Thioflavin S), but also with mOC31 immunoreactivity. Furthermore, mOC31 immunoreactivity is also correlated with a loss of smooth muscle actin immunoreactivity and an increase in HMGB1 immunoreactivity. These findings suggest that a unique fibrillar aggregate recognized by mOC31 is associated with a novel and specific pathogenic phenotype.

Materials and methods

Human and mouse tissue acquisition and preparation

Postmortem paraformaldehyde-fixed brain tissue was obtained from the neuropathological core of the University of California at Irvine Alzheimer's Disease Research Center (UCI ADRC). Subjects enrolled in the ADRC were given the MMSE and as standard protocol for autopsy cases, Braak and Braak neurofibrillary tangle and plaque staging was evaluated [77]. This study examined tissues from the frontal cortex (Brodmann's Areas B9 and B11), hippocampus, and cerebellum. All mouse tissue was acquired in accordance with animal protocols approved by the Institutional Animal Care and Use Committee at the University of California, Irvine. The 5XFAD-Tg (B6SJL-Tg(APPSwFlLon,PSEN1*M146L*L286V)6799Vas/Mmjax) mice were obtained from The Jackson Laboratory [93]. Mice were housed in groups of 2 to 5 or single-housed for aggressive males, under a 12-h light/12-h dark cycle at 21 °C, with food and water ad libitum. The 5XFAD-Tg mice display Aβ peptide deposition earlier than the 3XTG-AD mice. At 2-months, the Aβ deposits are predominately intraneuronal; while after 6-months the animals

have a considerable amount extracellular plaque deposition and behavior deficients [94]. At 2 and 6 months of age mice 5xFAD-Tg and age-matched controls were intracardially perfused using a peristaltic pump with approximately 120 ml of phosphate buffered saline over 10 min. Brains were isolated and one hemisphere was fixed in 4% (w/v) paraformaldehyde while the other half was micro-dissected to isolate cortex, hippocampus, and mid-brain and snap frozen in liquid nitrogen for further analysis. Paraformaldehyde-fixed human and mouse brain tissue was sectioned to 50 μm using a Vibratome Series 1000 vibrating microtome (The Vibratome Company, St. Louis, MO). Sections were stored in PBS containing 0.02% NaN_3 at 4° C for immunohistochemistry and immunofluorescence analysis.

Immunohistochemistry (IHC)

Free-floating sections were incubated in 3% hydrogen peroxide and 3% methanol in Tris-buffered saline (TBS), (20mM Tris and 137 mM NaCl, pH 7.6) for 30 minutes at room temperature (RT) to quench endogenous peroxidase activity. Non-specific background staining was reduced with a 1 hour incubation in blocking solution that consist of 2% (w/v) bovine serum albumin (BSA) (Sigma-Aldrich, St. Louis, MO) and 0.1% (v/v) Triton X-100 (Tx) (Sigma-Aldrich, St. Louis, MO) in TBS at RT. Tissues were incubated with primary antibodies diluted in blocking solution overnight at 4° C (antibody information listed in Table 2.1). The sections were then washed 2 x 5 minutes with 0.1% (v/v) Tx in TBS, blocked for 30 minutes in blocking solution, and incubated with the biotinylated secondary antibody (goat anti-rabbit or horse anti-mouse) (Vector Laboratories, Inc., Burlingame, CA) for 1 hour at RT at a concentration 10 μg/mL in blocking solution containing a 1.5% (v/v) of normal serum (Vector Laboratories, Inc.,

Burlingame, CA). After incubation with the secondary antibodies, the tissue sections were washed 2 x 5 minutes in 0.01% Tx in TBS and incubated in blocking buffer for 30 minutes at RT. An ABC peroxidase kit and 3,3'-diaminobenzidine (DAB) substrate kit (Vector Laboratories, Inc., Burlingame, CA) were used to detect the biotinylated secondary antibodies. Following the DAB incubation, the tissue sections were washed 5 x 5 minutes in dH2O and allowed to air dry on colorfrost coated-glass slides (Fisher Scientific, Waltham, MA). The sections were then dehydrated using sequential 3 minute incubations in 50%, 70%, and 95% ethanol, followed by a 15 minute incubation in 100% ethanol and cleared in Histoclear I/II for 5 minutes (National Diagnostics, Atlanta, GA). The sections were then mounted, cover slipped with DePeX (EMS, Hatfield, PA), and visualized using an Zeiss Axio Imager 2 (Carl Zeiss Microscopy, Oberkochen, Germany). The omission of either the primary or the secondary antibody was used as the negative control and resulted in no DAB staining.

Quantification of mOC31 area fraction and statistical analysis

Stained vessels in the cortex, hippocampus, and cerebellum were quantified by a systematic random sampling technique and area fractionator probe using MBF Biosciences Stereological Investigator software (MBF Biosciences, Williston, VT). Two independent experiments with sections measuring between 30 mm^2 and 60 mm^2 were imaged and subjected to a grid that measured 2.5 mm x 2.5 mm and a counting frame of 1.8 mm x 1.8 mm so that half of the tissue section was surveyed randomly. Approximately 5-10 counting frames were generated for each tissue section and the for area of immunoreactivity was divided by the total area to arrive at the area fraction and were plotted against the Braak and Braak Plaque Stage in humans, considering

plaque stage 0 = no AD pathology; plaque stage A–B = intermediate pathology/intermediate area of plaque deposition; plaque stage C = late AD pathology/high plaque area. Quantification was followed by statistical analyses applying a one-way ANOVA with post-hoc Tukey HSD (Honestly Significant Difference) by IBM SPSS Statistics Version 24 software. Data are shown as mean± SEM. p values are as follows: * $p < 0.05$, ** $p < 0.01$, and *** $p < 0.001$.

Immunofluorescence and confocal microscopy

Free-floating sections were washed with TBS, permeabilized in 0.1% (v/v) Tx in TBS for 30 min and incubated in blocking solution for 1-hr at RT. Human and mouse sections were then co-labeled with primary rabbit antibody mOC31 and an additional mouse antibody in blocking solution overnight at 4° C (antibody information listed in Table 2.1). After washing 3 times with TBS with 0.1% Tx, and incubation in blocking solution with 1.5% (v/v) normal goat serum for 1 hour, primary antibodies were detected with 10 µg/mL of highly cross-absorbed goat-anti-rabbit and goat-anti-mouse secondary antibodies coupled to Alexa Fluor 488, 555 or 647 dyes (Invitrogen, Thermo Fisher Scientific). Confocal micrographs were acquired using a Leica TCS SP8 confocal microscope (Leica Microsystems Inc., Buffalo Grove, IL) using a 20x (NA=0.75) or 63× objective (NA=1.40). The omission of either the primary or the secondary antibody was used as the negative control and referred to when setting microscope parameters to account for autofluorescence and non-specific staining.

Quantification of mOC31 integrated density

mOC31 immunoreactivity and Thioflavin S fluorescence were quantified by examining tissue sections of comparable regions of the brain tissue sections with a Leica TCS SP8 confocal microscope using a 63× objective. 3 to 5 (184 μm × 184 μm) fields were analyzed from 21 brain samples and at least 2 independent experiments. The confocal micrographs were imported into Volocity 6.3 high-performance 3D imaging software (PerkinElmer) in which volume and fluorescence intensity of objects were automatically collated after setting threshold for minimum object size and intensity. Quantification was followed by statistical analyses applying a one-way ANOVA with post-hoc Tukey HSD (Honestly Significant Difference) by IBM SPSS Statistics Version 24 software. Data are shown as mean± SEM. p values are as follows: * $p < 0.05$, ** $p < 0.01$, and *** $p < 0.001$.

Correlation between mOC31 and α-actin and HMGB1 immunoreactivity

mOC31 and α-actin immunoreactivity were quantified by examining tissue sections of comparable regions of the brain tissue sections with a Leica TCS SP8 confocal microscope using a 63× objective. 5 to 7 (72 μm × 72 μm) fields were analyzed from 29 human subjects and 2 independent experiments. The confocal micrographs were imported into Volocity 6.3 high-performance 3D imaging software (PerkinElmer) in which volume and fluorescence intensity of objects were automatically collated after setting threshold for minimum object size and intensity. For over 100 individual vessels the florescence intensity of mOC31 and α-actin was plotted and Pearson correlation coefficient was determined using IBM SPSS Statistics Version 24 software.

Data are shown as Pearson's correlation *r*. p values are as follows: * $p < 0.05$, ** $p < 0.01$, and *** $p < 0.001$.

Antibodies used in IHC or IF

The antibodies used in this chapter and the working concentrations are listed in Table 2.1.

Table 2.1: List of Antibodies used in Chapter 2

Antibody	Epitope/Immunogen	Source	Type	Working Dilution	Application
mOC31	Fibrillar Aβ	Glabe Lab	rabbit	1 µg/mL	IHC, IF
6E10	1-16 of Aβ	Covance	mouse	5 µg/mL	IHC, IF
α-actin SMC	n-terminus of smooth muscle α-actin	Sigma	mouse	1 µg/mL	IF
HMGB1 (F1D)		abcam	mouse	1 µg/mL	IF
IL1β		R&D Systems	goat		IF
Iba	c-terminus of synthetic IBA1 peptide	Wako	rabbit	3 µg/mL	IF
NFκB		Cell Signaling	rabbit	1:500	IF

Results

Smooth muscle cells accumulate significant amounts of vascular amyloid immunoreactivity in the hippocampus of AD brains and aged 5XFAD-Tg mice.

Evidence suggests that Aβ deposition in the entire brain follows a distinct sequence in which regions are hierarchically involved. That is, amyloid propagation occurs anterograde to neural circuits; beginning with the neocortex, moving to subcortical regions that include the hippocampus, and ending in the cerebellum [84]. In a cohort of 23 brains from the ADRC brain bank (Table 2.2), tissue sections from cortex, hippocampus, and cerebellum were labeled with mOC31 and nuclear fast red as a counter stain for nuclei. After immunohistochemistry and

Table 2.2: apoE cohort

Subject ID #	Age	ApoE	NPDx1	Tangle Stage	Plaque Stage	MMSE
26-05	90	2/2	Normal (mild Braak Changes)	Stage 3	Stage A	29
08-14	52	2/3	Normal (mild braak changes)	Stage 3	Stage A	20
06-03	84	3/3	Normal (mild Braak Changes)	Stage 3	None	22
05-04	76	3/3	Normal (mild Braak Changes)	Stage 1	None	3
16-13	76	3/3	Normal (mild Braak Changes) and Parkinsons disease	Stage 2	None	30
39-13	78	3/3	Pick's Disease	Stage 0	None	9
24-11	86	3/3	Normal (mild Braak Changes)	Stage 3	Stage A	22
32-05	89	3/3	Normal (mild Braak Changes)	Stage 3	Stage B	24
14-03	76	3/3	Alzheimer's Disease	Stage 6	Stage C	6
10-04	71	3/3	Alzheimer's Disease	Stage 6	Stage C	3
10-10	63	3/3	Alzheimer's Disease	Stage 6	Stage C	2
12-12	82	3/3	Alzheimer's Disease	Stage 6	Stage C	17
04-03	83	4/4	Vascular Dementia	Stage 3	None	28
16-07	90+	4/4	Normal (mild Braak Changes)	Stage 4	Stage A	28
02-12	64	4/4	Alzheimer's Disease	Stage 5	Stage B	7
21-13	89	4/4	Alzheimer's Disease	Stage 4	Stage B	16
19-03	77	4/4	Alzheimer's Disease	Stage 6	Stage C	11
39-04	70	4/4	Alzheimer's Disease	Stage 6	Stage C	2
03-08	72	4/4	Alzheimer's Disease	Stage 6	Stage C	0
13-08	89	4/4	Alzheimer's Disease	Stage 5	Stage C	17
04-10	79	4/4	AD and Vascular Dementia	Stage 6	Stage C	12
11-13	78	4/4	Alzheimer's Disease	Stage 6	Stage C	3
37-13	71	4/4	Alzheimer's Disease	Stage 4	Stage C	23

stereological analysis we found that mOC31 immunoreactivity is deposited into smooth muscle cells in equal proportions in the cortex, hippocampus, and cerebellum before any evidence of amyloid plaques (Figure 2.1-a). Vascular amyloid modestly increases in the cortex and cerebellum as the disease progresses, with the hippocampus accumulating as much as 2x more mOC31 immunoreactivity in brains with intermediate plaque pathology when compared to

brains where plaques are absent (*p<0.5)* (Figure 2.1-b). We decided to investigate directly the temporal relationship between mOC31 vascular amyloid immunoreactivity and disease

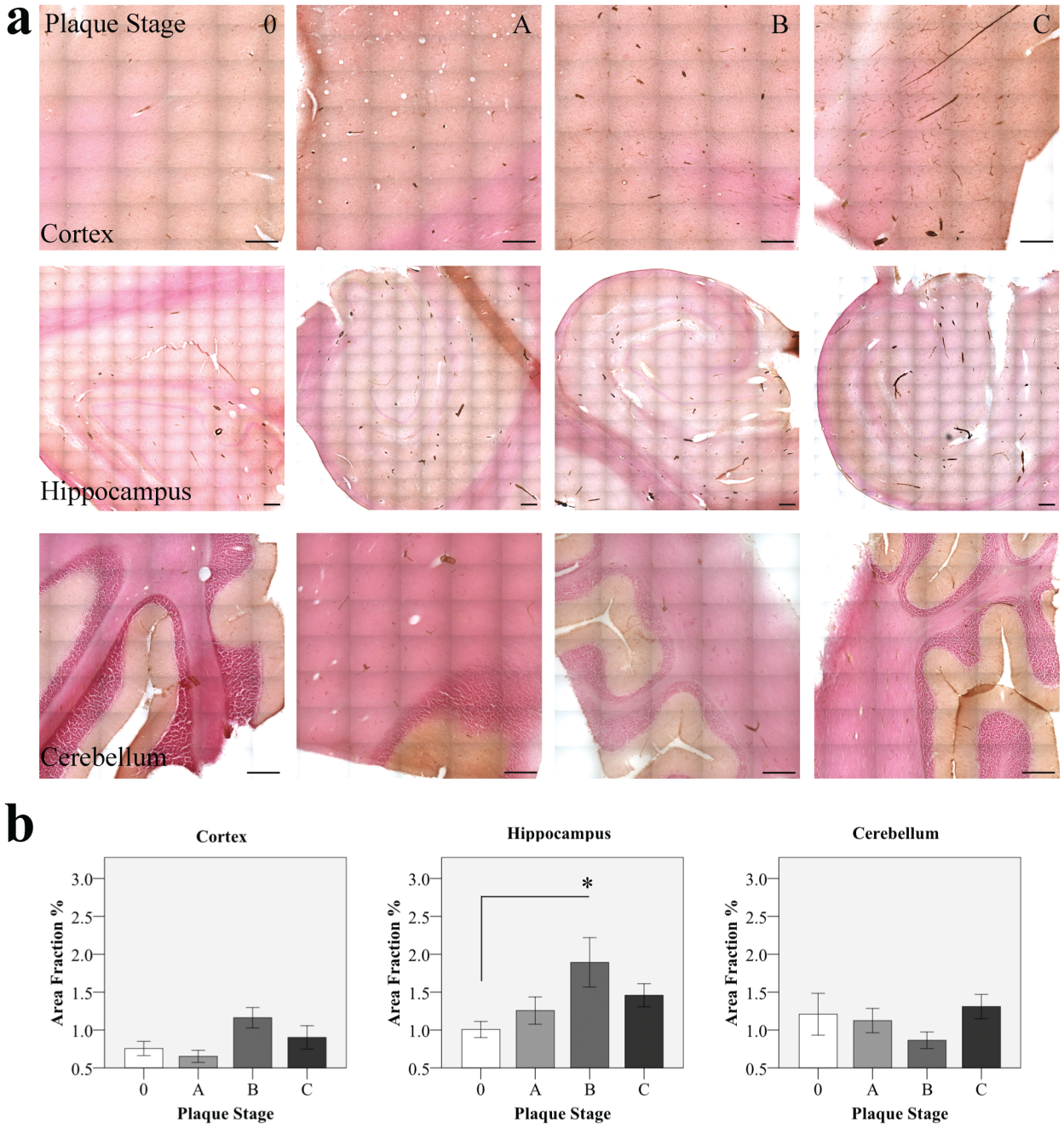

Figure 2.1 Vascular mOC31 immunoreactivty correlates with paraenchymal plaque deposition in the hippocampus of AD brain. (a) Cortex, hippocampus, and cerebellum tissue sections from 21 human brains were probed with mOC31 by immunohistochemistry (brown) and counter stained for nucleic acids by nuclear fast red (red). (b) Wide-field tile scans were taken at 20X and tissue sections were quantified in stereological investigator using area fraction fractionator probe. Bars indicate the mean ± sem. * = $p < 0.05$. Scale bar 500 µm

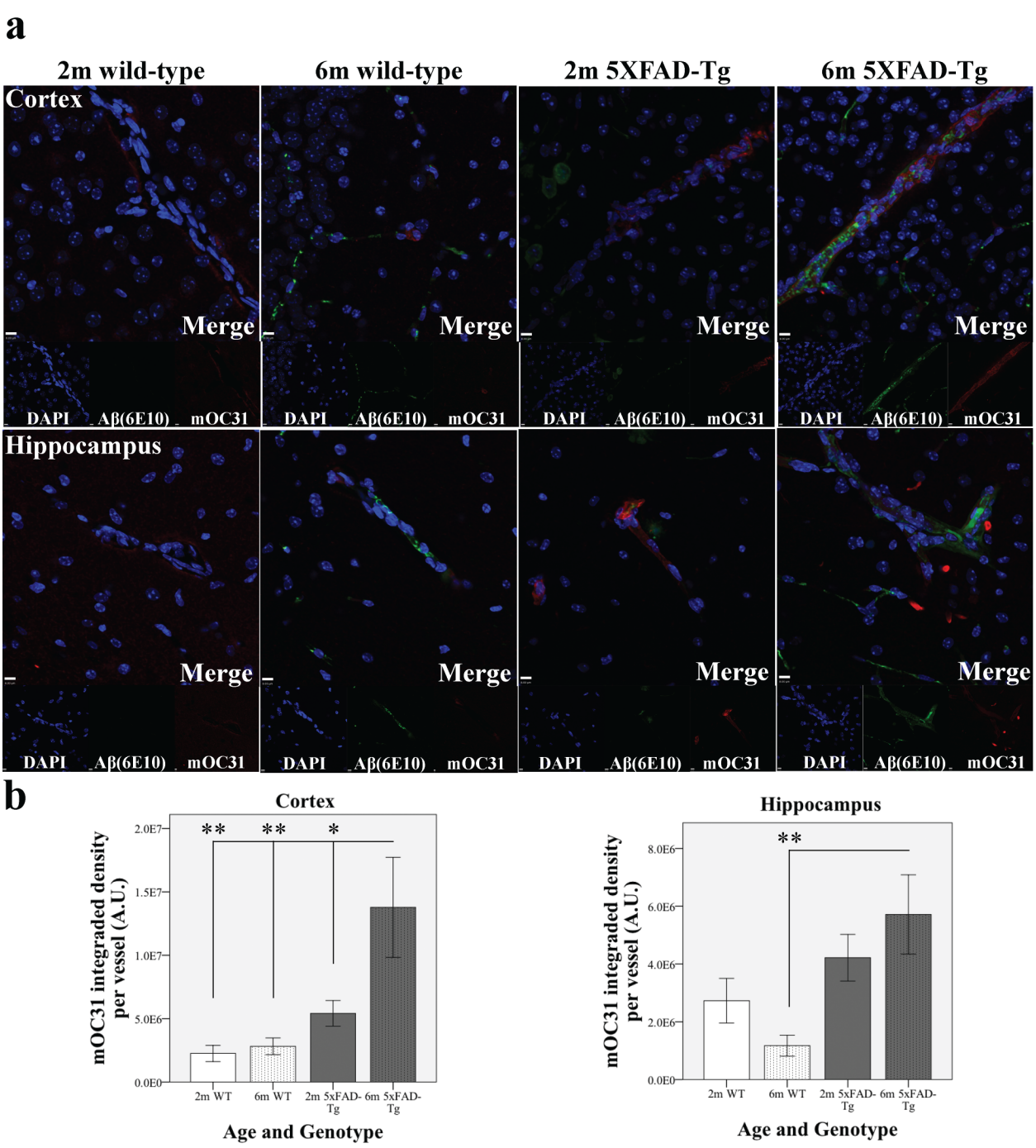

Figure 2.2 Vascular mOC31 immunoreactivty correlates with age in the cortex and hippocampus of 5XFAD-Tg mouse brain. (a) Cortex (a) and hippocampus tissue sections from 2m, 6m wild-type and 5XFAD-Tg mouse brains were probed with mOC31 (green) and anti-Aβ(6E10) (red) by immunofluorescence. Nuclei were counter-stained with DAPI (blue). (b) Confocal micrographas were obtained and the intergrated density per vessel was quantified by the analyical software Volocity. Bars indicate the mean ± sem. * = $p < 0.05$ **, $p < 0.01$. Scale bar 8 µm

progression in aged 5XFAD-Tg mice. We found that with age 5XFAD-Tg mice accumulate increasing levels of mOC31 vascular amyloid immunoreactivity (Figure 2.2-a). Wild-type mice have trace amounts of staining, but these levels appear to be at a steady state and do not statistically differ between 2 months and 6 months of age. At 6 months, the cortex and hippocampus of 5XFAD-Tg mice had 3x more amyloid immunoreactivity per vessel than age-matched non-Tg ($p<0.01$) (Figure 2.2-b). This findings suggest that the accumulation of mOC31 vascular amyloid immunoreactivity occurs before the deposition extracellular plaque and behavior deficits in human and Tg brains and that level of vessel involvement correlates with disease progression.

ApoE4 genotype is correlated with an increase in vascular mOC31 amyloid immunoreactivity and Thioflavin-S fluorescence

We investigated whether the CAA/AD associated risk factor, apoEε4, influences the deposition of mOC31 vascular amyloid immunoreactivity in a cohort of 23 brains homozygous for apoE2, apoE3, or apoE4 (Table 2.2). Double label immunofluorescence with mOC31 and Thioflavin S showed that amyloid load, determined by integrating the area and intensity of fluorescence, recognized by both Thioflavin S and mOC31 was significantly elevated in apoEε4 carriers when compared to apoEε3 ($p<0.01$) (Figure 2.3). It is worth mentioning that in the apoEε3 carriers, a larger proportion of mOC31 immunoreactivity that does not overlap with Thioflavin S. The apoEε2 in one brain examined contained minuscule amounts of mOC31 immunoreactivity.

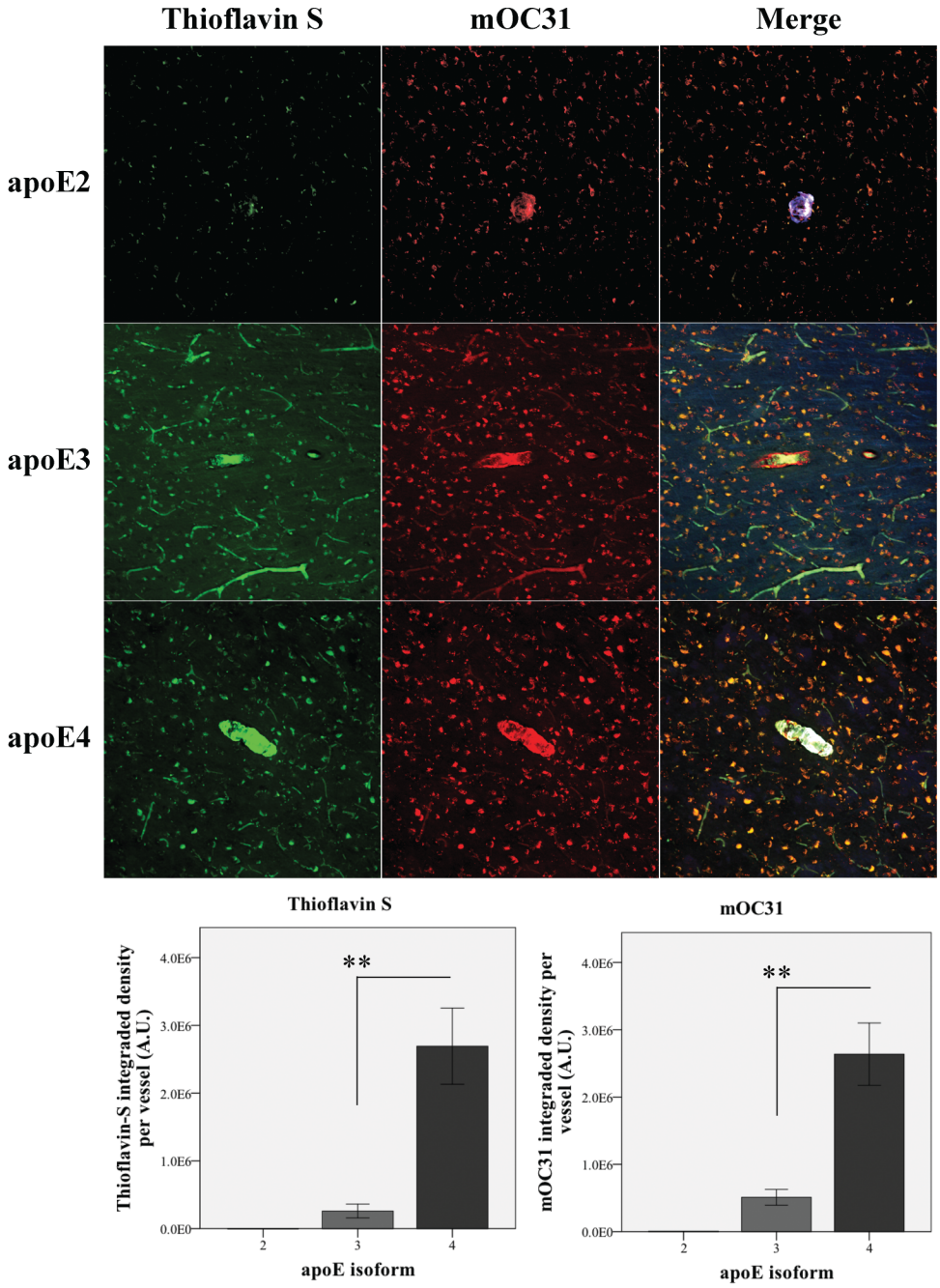

Figure 2.3 ApoE4 genotype is correlated with an increase in vascular mOC31 amyloid immunoreactivity and Thioflavin-S fluorescence. Human brain tissue sections from cortex(Brodmann's Area 9) were probed with Thioflavin S (green) and mOC31 (red) by immunofluorescence. Confocal micrographas were obtained and the intergrated density per vessel was quantified by the analyical software Volocity. Bars indicate the mean ± sem. * = $p < 0.05$ **, $p < 0.01$.

mOC31 amyloid immunoreactivity is correlated with a loss of α-actin immunoreactivity

In our search to understand where in the vasculature mOC31 immunoreactivity was accumulating, we made the observation that the immunoreactivities of vascular amyloid and α-smooth muscle actin were not only colocalized but also correlated. Specifically, we frequently noticed that when anti-α-actin staining was high, mOC31 staining was weak and vice versa (Figure 2.4-a). We took our cohort of 23 brains and subjected them to double label immunofluorescence, probing for mOC31 and α-actin, and acquired confocal micrographs of over one-hundred vessels. After importing them into Volocity, an analytical program that measured the volume and fluorescence intensity of individual vessels, we found significant negative Pearson correlation ($\boldsymbol{r} = -0.512$, $p < 0.01$) (Figure 2.4-b). We also examined if this loss of actin immunoreactivity resulted in arterioles that were prone to leak, searching for hemosiderin by Prussian-blue stain. We observed no differences between mOC31-positive and mOC31-negative vessels (data not shown). These findings support an inverse relationship between $mOC31^{+}$ vascular amyloid and α-actin immunoreactivity exists in brain vascular smooth muscle cells, but a pathogenic consequence remains to be determined.

Inflammatory signal HMGB1 colocalizes with mOC31 vascular amyloid, but not pro-inflammatory cytokine or microglia

Since mOC31 vascular amyloid immunoreactivity is correlated with a loss of α-actin staining we investigated the inflammatory microenvironment around the amyloid laden vessels. Double-label immunofluorescence, coupled with confocal microscopy, revealed that high-mobility group box protein 1 (HMGB1) is colocalized in the arterioles of brains containing mOC31 staining (Figure

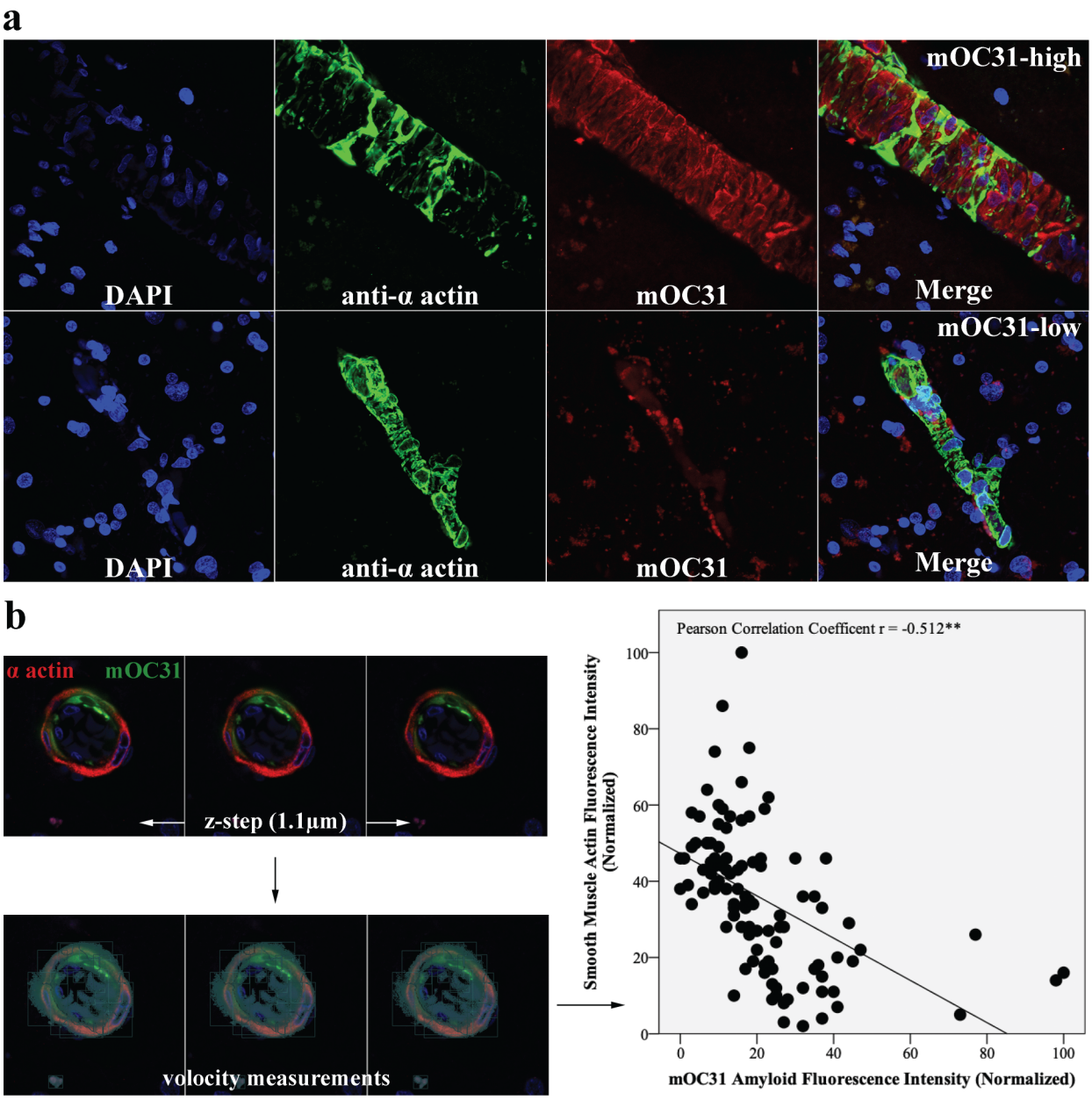

Figure 2.4 mOC31 amyloid immunoreactivity is correlated with a loss of α-actin immunoreactivity. (a) Maximum intensity projection of confocal micrographs from a human AD brain depicting α-actin (green) and mOC31 (red) immunoreactivities from high (top panel) and low (bottom panel) mOC31 containing vesseles. (b) Flow-chart illustrating workflow: confocal micgrographs from 3 focal planes were imported into analytical software Volocity and fluorescence intensities were quantified. Individual dots are the fluoresence intensities for α-actin and mOC31 of single vessels and Pearson correlation coeffienct was calculated. r = -0.512 ** p = 0.01 N=108.

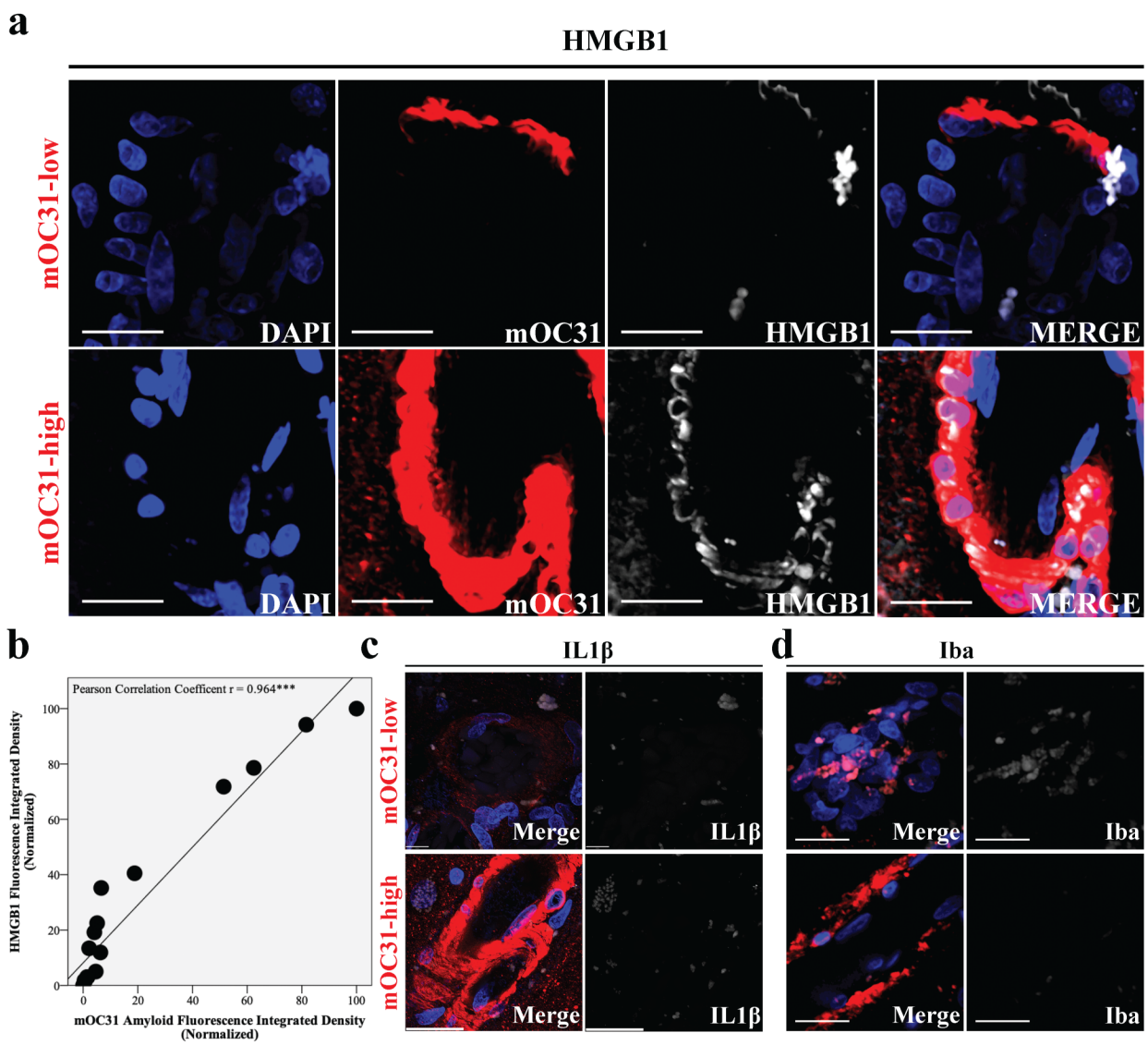

Figure 2.5 Inflammatory signal HMGB1 colocalizes with mOC31 vascular amyloid, but not pro-inflammatory cytokine or microglia. Maximum intensity projects of confocal micrographs from human brain cortex (Brodmann's area 9) tissue sections with either low mOC31 or high mOC31 immunoreactivity (red) and co-labeled with markers of inflamation (gray scale). Markers of inflammation include (a) anti-HMGB1, (b) anti-IL1β and (d) anti-Iba. (c) Fluorescence integrated densities of confocal micrographs probed for mOC31 and HMGB1 were plotted for 17 vessels and Pearson correlation coefficent was calculated: $\boldsymbol{r} = 0.964$ N=17, $p < 0.001$).

2.5-a) HMGB1 and mOC31 fluorescent densities were found to be highly correlated and statistically significant ($\boldsymbol{r} = 0.964$, p <001) (Figure 2.5-b). HMGB1 in these vascular smooth muscle cells is not only localized in the nucleus, but detectable levels are found in the cytosol.

Cytosolic HMGB1 has been shown to be secreted and is associated with systemic inflammation [95]. No detectible staining for pro-inflammatory cytokine (anti-IL1β) or activated microglia (anti-Iba) was observed in the brain tissue examined (Figure 2.5-c,d). These findings suggest that mOC31 vascular amyloid immunoreactivity is correlated with inflammatory factors, but work needs to be done to ascertain the mechanism.

Discussion

A growing body of evidence supports the idea that vascular dysregulation is a major risk factor for sporadic Alzheimer's disease [96]. Here we reported the pathological significance of a unique amyloid immunoreactivity deposited into vascular smooth muscle cells. We found that in human brain and 5xFAD-Tg-mouse brains vascular amyloid accumulates before the presence of amyloid plaques (Figure 2.1 and 3.2). mOC31 vascular amyloid immunoreactivity is significantly elevated in the hippocampus at intermediate stages of amyloid pathology and correlates with age-related disease progression in Tg-mouse models of AD and linked to apoE4-related amyloid deposition in arterioles (Figure 2.2 and 3.3).

The accumulation of mOC31 immunoreactivity is correlated with a loss of smooth muscle actin immunoreactivity (Figure 2.4). The observation that vascular amyloid and α-actin antibody immunoreactivity are negatively correlated is not novel. In a much larger cohort of humans, vascular amyloid was found to have a significant negative correlation (r=-0.631) compared to our observation of (r=-0.512) [97]. Surprisingly, Stopa et. al did not observe the significant correlations with AD disease progression and apoE polymorphism we report. The choice of

amyloid antibody may provide a reasonable explanation for this difference. In their experiments amyloid was detected by a polyclonal rabbit anti-human antibody, we specifically used a monoclonal antibody directed against a subset of Aβ42 fibrils. mOC31 does not colocalize with general anti-Aβ antibodies (e.g. 6E10, 4G8, anti-Aβ40 and Aβ40) and in early and intermediate stages of pathology does not entirely colocalize with Thioflavin S. Therefore, the relationship we characterize may be novel and specific to aggregates recognized by mOC31. In any regard, Stopa et al. find that in AD, a loss of smooth muscle actin immunoreactivity is associated with increases in arteriolar wall width and luminal diameter in patients with significant AD pathology versus those without and also in subjects with clinical AD compared with non-demented patients. These findings suggest that mOC31 immunoreactivity may be correlated with compromises in blood flow self regulation.

Amyloid deposition has been known to cause increases in inflammation in the form of cytokine release and microglia recruitment; in AD we observe no difference between control and demented brains (Figure 2.5) [98]. More sensitive approaches may need to be utilized to determine the presence of cytokine release, such as in-situ hybridization. Systemic inflammation, measured by the transcription factor HMGB1 is elevated in response to mOC31 immunoreactivity; this transcription factor is of particular significance because it has been reported to correlate with Aβ levels in serum of AD patients (vs. control subjects) [99]. Furthermore, vascular smooth muscle cells have been shown to produce extracellular HMGB1 found in atherosclerotic plaques, but not normal arteries, and in response proliferate, migrate, and secrete more HMGB1[95]. Blocking the secretion of vascular smooth muscle cells may

prove to be an important strategy for not only atherosclerotic disease, but also CAA in Alzheimer's disease.

CHAPTER 3

Mechanisms of pathogenicity in an *in vitro* human brain vascular smooth muscle cell culture model

Introduction

In vitro systems have allowed for the examination of several aspects of CAA; in particular, smooth muscle and pericyte cell cultures have been used to study cellular toxicity towards vascular amyloid. Initial studies using these cultured cell types showed that soluble Aβ42-WT, but not Aβ40-WT, promoted cellular degeneration, an increase in amyloid precursor protein (APP) expression, and inflammation (100,101). Unexpectedly, pre-formed Aβ42-WT fibrils that were administered to cultured VSMCs did not have the pathogenic effects seen with freshly prepared Aβ42-WT. Studies conducted with familial CAA substitutions at E22 and D23 of Aβ40 demonstrated increases in toxicity and cellular degeneration towards cultured VSMCs over Aβ40-WT (31). The Flemish familial CAA substitution, A21G, was also shown to not be cytotoxic *in vitro* despite patients accumulating severe amyloid angiopathy, dementia and cerebral hemorrhage [102]. *In vivo* amyloid is deposited into vasculature when the ratio of Aβ40:Aβ42 favors the shorter peptide and although the cytotoxicity observed with Aβ42-WT is striking it maybe not be the dominant pathological agent to vascular smooth muscle cells [17,103]. This raises the question as to what pathological effect does Aβ40-WT and Aβ40-A21G have on vascular smooth muscle cells?

To address this we developed an *in vitro* model where we treated vascular smooth muscle cells with 2-5 μM Aβ (previous studies used 25 μM) and cultured cells for up to 84 hours. This model

generally reproduced what was known about Aβ40 cytotoxicity; that is, Aβ40-WT and Aβ40-A21G are not cytotoxic to primary cultures of human brain vascular smooth muscle cells and preformed aggregates of Aβ further decreases cytotoxicity. A novel finding from this study was that at these concentrations lysosomal compartments become "leaky" as previously reported for other cell types [104], proving a potential avenue for exogenously administered Aβ to enter the cell. In fact if we stain for an anti-fibrillar Aβ antibody (mOC31) we see an increase in immunoreactivity in Aβ treated cells. Additionally, we see a dramatic decrease in α-actin immunoreactivity without cytotoxicity. Finally, immunoprecipitation using mOC31 revealed an extremely stable interaction between Aβ and α-actin. These findings present a novel pathogenic effect of soluble Aβ40-WT and Aβ40-A21G on human brain vascular smooth muscle cells that closely mirror *in vivo* observations in AD and Tg-mouse models of AD.

Materials and methods

Primary human brain vascular smooth muscle cell culture

Primary human cerebral VSMC were purchased from ScienCell Research Laboratories (Carlsbad, CA) and grown according to the manufacturer's instructions. Primary human cerebral VSMC cells were used between passages 4 and 10 and maintained at 37 °C in humidified air containing 5 % CO2.

Peptide Production

Aβ40(wt) and Aβ40(A21G) mutant peptide were prepared as previously described [105]. Side chain protected fluorenylmethyl- oxycarbonyl (Fmoc) amino acids, Fmoc-PAL-PEG-polystyrene

support, and O-(benzotriazol-1-yl)-N,N,N,N-tetramethyl-uronium tetrafluoroborate (TBTU) were purchased from Applied Biosystems, Inc. (Carlsbad, CA), and N,N-diisopropyl- ethylamine (DIEA), dithiothreitol (DTT), thioanisole, ethanedithiol, and anisole were from Aldrich. Trifluoroacetic acid (TFA) was purchased from Advanced Chemical Technology, Inc. (Louisville, KY). WT Aβ40 and Aβ40 containing the FAD mutations were synthesized by the batch-wise method on a CS336X (CS Bio, Inc., Menlo Park, CA) peptide synthesizer using Fmoc/t-butyl chemistry. TBTU/DIEA was used as the coupling reagent for 1 h, and 2% piperidine, 2% 1,8-diazabicyclo[5.4.0]undec-7-ene in dimethylformamide were used as the deprotection reagent for 7 min. Cleavage of the peptide from the resin support and the concomitant deprotection of the amino acid side chains were carried out in reagent R (TFA/ thioanisole/ethanediol/anisole at 90:5:3:2) at room temperature for 6 h. This step was followed by removal of the exhausted resin by filtration and precipitation of the peptide product in ice-cold anhydrous ether. The precipitate was allowed to settle overnight at 20 °C and then washed three times with ice-cold water and dried under high vacuum. Preparative reversed phase high performance liquid chromatography was performed using a Waters (Irvine, CA) system (Model 510) with a Vydac C4 (214TP1022) column and a flow rate of 8 ml/min. The crude peptide was loaded after treatment with DTT and eluted using 0.1% TFA/H2O (buffer A) and 0.1% TFA/ acetonitrile (buffer B) by gradient (5–95% buffer B). The center cut from the preparative run was frozen in liquid nitrogen immediately after collection and lyophilized under high vacuum. Peptide structure and purity (90%) were verified by mass spectroscopy.

Aggregation of Aβ40(wt) and Aβ40(A21G) FAD Variant

Synthetic peptides of Aβ40, along with an Aβ40 variant containing the A21G FAD mutation were aggregated over a 10-day time course, as previously described [106]. Briefly, 0.3 mg of the lyophilized peptide was resuspended in 33 µL of 100 mM NaOH and incubated for 10 min. This solution was then diluted to a 45 µM final concentration by adding 1.5 ml of 10 mM sodium phosphate buffer, pH 7.4. The mixture was aliquoted and allowed to self assemble on the bench at RT; when desired time point was reached they were snap frozen and stored at -80 °C.

Treatment of cell culture with Aβ40

Primary HVSMC were plated onto Primaria™, 6-well flat bottom plates (Corning Inc, Life Sciences, Durham, NC) at a density of 8.0 x 10^4 cells/well or onto 12-well flat bottom plates (Corning Inc, Life Sciences, Durham, NC) containing pre-treated poly-L lysine glass coverslips (2 µg/cm^2) at a density of 2.0 x 10^4 cells/well two days prior to experiments. On treatment day, cells (near 80% confluency) were washed gently for 15-20 seconds with warmed (37 °C) Dulbecco's Phosphate-Buffered Saline (DPBS) and incubated with freshly prepared 2 µM Aβ solution (45 µM Aβ described above then diluted in HVSMC media) for 84 hours. The control treatment was equal volume of 10mM sodium phosphate buffer diluted in HVSMC media.

Cell lysis and coverslip preparation

HVSMC cultured in 6-well flat bottom plates were washed 3 times for 15-20 seconds with warmed DPBS and detached from culture plates after a 7 minute incubation in Accutase (Innovative Cell Technologies, Inc, San Diego, CA) at 37 °C. Detached cells were transferred to 1.5 mL sterile tubes and centrifuged for 5 minutes at 1,000 x g. After centrifugation the

supernatant was discarded and cell pellet was resuspended in chilled lysis buffer (50 mM Tris HCl, 150 mM NaCl 1% Trition-X 100, 5 mM EDTA, and Halt protease inhibitor cocktail #78410 Thermo). Samples were pipetted up and down for 10-15 seconds, placed on vortex for 5 seconds (low setting), and centrifuged at 14,000 x g for 20 minutes to remove cell debris. Protein concentration of supernatant was measured using BCA protein quantification assay (Thermo Scientific, Waltham, MA) and subject to immunoprecipitation, gel electrophoresis, and Western blot analysis.

HVSMC cultured in 12-well flat bottom plates containing coverslips were prepared for staining by washing wells three times for 20-30 seconds, followed by incubation in 2% paraformaldehyde diluted in PBS (w/v) for 30 minutes at RT. Coverslips were than transferred to clean 12-well flat bottom plate and washed with PBS three times for 20-30 seconds.

Immunoprecipitation

Immunoprecipitation with mOC31, anti-α-actin, mouse-IgG2a, and rabbit-IgG were preformed by binding 3µg of purified antibody to protein G magnetic beads and cross-linking with BS_3 (Invitrogen, Waltham, MA) according to the manufacturers instructions. Following antibody binding, 10µg of HVSMC lysate was incubated with beads, then washed with PBS and transferred to a new tube. Immunoprecipitate was eluted from beads with 50 mM glycine pH 2.8 and mixed with sample loading buffer before heating at 70 °C for 10 minutes.

Gel electrophoresis and Western blotting analysis

For gel electrophoresis, 25 µl of each sample were mixed with 5X loading buffer (312 mM Tris pH 6.8, 10% SDS, 40% glycerol, 25% 2-mercaptoethanol, bromophenol blue) and the resulting 30 µl mixtures were loaded onto an 18-well 4%-20% precast Triton Gradient eXtended (TGX) gel (BioRad Laboratories, Hercules, CA). The gel was then run at 125 V and the resolved proteins were transferred onto a 0.2 µm Protran nitrocellulose (GE Healthcare Life Science) or Immun-Blot PVDF (BioRad Laboratories, Hercules, CA) membrane at 400 mA for 75 minutes. Non-specific binding was blocked by incubating the membrane in 5% non-fat dried milk in PBS-T for 1 hour at RT. The blot was then incubated in the indicated primary antibody overnight at 4 °C. After three 5 minute washes in TBS-T, the membranes were blocked with 5% non-fat dried milk in PBS-T for 30 minutes followed by incubation with the appropriate secondary antibody for 1 hour at RT. Following three 5 minute washes in TBS- T, the results were visualized using the ECL protocol and micrographs of the results were obtained by exposing membranes to Amersham Hyperfilm ECL (GE Healthcare Bio-Sciences, Buckinghamshire, UK) or using a Nikon D700 (Nikon Inc., Melville, NY) camera as described in methods for dot blot analysis.

Immunofluorescence, confocal microscopy and quantification

Paraformaldehyde-fixed HVSMC cultured on poly-L lysine coated coverslips were washed 3 times for 5 minutes with TBS, permeabilized in 0.1% (v/v) Tx in TBS for 30 minutes and incubated in blocking solution for 1-hour at RT. Coverslips were then co-labeled with primary rabbit antibody (e.g. mOC31) and a mouse antibody (e.g. α-actin Smooth Muscle Cells) in blocking solution for 2 hours at RT (antibody information listed in Table 3.1). After washing 3

times for 5 minutes in TBS with 0.1% Tx, and incubation in blocking solution with 1.5% (v/v) normal goat serum for 1 hour, primary antibodies were detected with 10 µg/mL of highly cross-absorbed goat-anti-rabbit and goat-anti-mouse secondary antibodies coupled to Alexa Fluor 488, 555 or 647 dyes (Invitrogen, Thermo Fisher Scientific) for 1 hour at RT. When probing with antibodies from identical species (e.g. mOC31/NFκB p65), one monoclonal antibody was biotinylated and detected using streptavidin conjugated to Alex Fluor 488, 555, or 647 dyes (Invitrogen, Thermo Fisher Scientific) after detection of non-biotinylated primary antibody and blocking with 10x excess of normal IgG of primary antibody species (e.g. rabbit IgG). Selected coverslips were counter stained with the toxin philloidin (1:1000) that was conjugated to CF® 555 dye, a well established method visualizing f-actin (Biotium Inc, Fremont, CA), in parallel with primary antibody incubation. Confocal micrographs were acquired using a Leica TCS SP8 confocal microscope (Leica Microsystems Inc., Buffalo Grove, IL) using a 63× objective (NA=1.40). Phalloidin, mOC31 and α-actin immunoreactivity were quantified from two independent experiments. 15 to 17 (245 µm × 245 µm) fields were imported into Volocity 6.3 high-performance 3D imaging software (PerkinElmer) in which volume and fluorescence intensity of objects were automatically collated after setting threshold for minimum object size and intensity. Quantification was followed by statistical analyses applying a one-way ANOVA with post-hoc Tukey HSD (Honestly Significant Difference) by IBM SPSS Statistics Version 24 software. Data are shown as mean± SEM. p values are as follows: * $p < 0.05$, ** $p < 0.01$, and *** $p < 0.001$.

Pre-treatment with Lucifer yellow and quantification

HVSMC were first pre-incubated with 10 mg/ml Lucifer Yellow (CH) in culture media for 14 hours and were washed 3 times for 20-30 seconds with PBS prior to Aβ40 treatment. The Lucifer Yellow-labeled cells were then treated with Aβ diluted in culture media as previously described for 12 and 24 hours. The coverslips were then rinsed with warm PBS and confocal micrographs were acquired using a Leica TCS SP8 confocal microscope (Leica Microsystems Inc., Buffalo Grove, IL) using a 63× objective (NA=1.40). Lysosomal leakage was defined by the presence of Lucifer Yellow fluorescence in the cytosol. Confocal images were manually quantified from 4 (245 μm × 245 μm) fields for each time point and reported as a percentage of total cells per field. Quantification was followed by statistical analyses applying a one-way ANOVA with post-hoc Tukey HSD (Honestly Significant Difference) by IBM SPSS Statistics Version 24 software. Data are shown as mean± SEM. p values are as follows: * $p < 0.05$, ** $p < 0.01$, and *** $p < 0.001$.

Cell viability assay and quantification

Primary HVSMC were grown on poly-L lysine coated Lab-Tek II 8 chambered coverglass (Nunc, Rochester, NY) and treated with Aβ for 72 hours, as previously described. Treated HVSMC were then exposed to 2 μM calcein AM and 4 μM Ethidium homodimer-1 (EthD) (Invitrogen, Thermo Fisher Scientific) for 15 minutes at 37° C. Cells were then quickly washed in PBS and Live/Dead cells were imaged and confocal micrographs were acquired using a Leica TCS SP8 confocal microscope (Leica Microsystems Inc., Buffalo Grove, IL) using a 20x (NA=0.75). Live/Dead cells were quantified from two independent experiments. Four fields (1000 μm × 1000 μm) were analyzed from each treatment condition. The confocal micrographs

were imported into Volocity 6.3 high-performance 3D imaging software (PerkinElmer) in which cell counts and fluorescence intensity of calcein AM and EthD objects were automatically collated after setting threshold for minimum object size and intensity. Cells with fluorescence above background for only EthD were classified as dead and reported as a percent of total cells per field. Cells with fluorescence above background for calcein AM and EthD were classified as loss of membrane integrity and were reported as a percent of total cells per field. Quantification was followed by statistical analyses applying a one-way ANOVA with post-hoc Tukey HSD (Honestly Significant Difference) by IBM SPSS Statistics Version 24 software. Data are shown as mean± SEM. p values are as follows: * $p < 0.05$, ** $p < 0.01$, and *** $p < 0.001$.

Antibodies used in IHC or IF

The antibodies used in this chapter and the working concentrations are listed in Table 3.1

Table 3.1: Antibodies used in Chapter 3

Antibody	Epitope/Immunogen	Source	Type	Working Dilution	Application
mOC31	Fibrillar Aβ	Glabe Lab	rabbit	1 µg/mL	WB, ICC
α-actin SMC	n-terminus of smooth muscle α-actin	Sigma	mouse	1 µg/mL	WB, ICC
α-actin SMC (polyclonal)	α-actin	Abcam	rabbit	1:500	WB
anti-Aβ (6E10)	n-terminus of Aβ peptide (1-16)	Covance	mouse	1 µg/mL	WB

Results

mOC31 recognizes fibrillar oligomers of Aβ and the loop adjacent to glutamic acid and aspartic acid is an important part of the epitope

In human and Tg tissue sections mOC31 immunoreactivity is exclusively localized within vascular smooth muscle cells, even in tissue with abundant parenchymal plaques. To investigate whether mOC31 preferred soluble or insoluble *in vitro* aggregates, we spotted nitrocellulose membrane with synthetic wild-type Aβ40 and Aβ42 peptide that was dissolved in NaOH then diluted in phosphate buffered saline (PBS), as previously described [29]. Dot blotted samples included freshly prepared (Day 0, D0) and four day aggregated (Day 4, D4) synthetic Aβ that was centrifuged at 100,000 x g proving two fractions for each sample: supernatant (DXs) and pellet (DXp). We found that mOC31 recognized 100,000 x g soluble aggregates present in both Aβ40 and Aβ42 preparations (Figure 3.1-a). The D0s and D4s samples were a heterogenous mixture of fibrillar aggregates as it also had immunoreactivity for mOC78 and OC serum (pOC), but not the anti-prefibrillar aggregate serum A11. Adam Kreutzer in the laboratory of Dr. James Nowick recently crystalized two hairpin structures formed by $A\beta_{17-23}$ and $A\beta_{30-36}$ (peptide 1) and $A\beta_{17-36}$ (peptide 2); peptide 1 lacks the loop connecting the two β-strands [80]. Previously we reported that mOC31 recognized a linear and discontinuous epitope that corresponded to residues $A\beta_{3-10}$ and $A\beta_{22-23}$; we investigated whether mOC31 could differentiate these two peptides because of the proximity of the mOC31 epitope (specifically glutamic and aspartic acid at the 22nd and 23rd residue) to the loop formed by the β-hairpin in peptide 2. Surprisingly, mOC31 specifically recognized peptide 2 that contained the loop linking the β-strands and not the peptide 1 which only contained the β-strands and no loop despite both containing glutamic and aspartic

acid (Figure 3.1-b). These findings suggest that mOC31 recognizes fibrillar oligomers of Aβ and the loop adjacent to glutamic acid and aspartic acid is signifiant to the antibodies epitope.

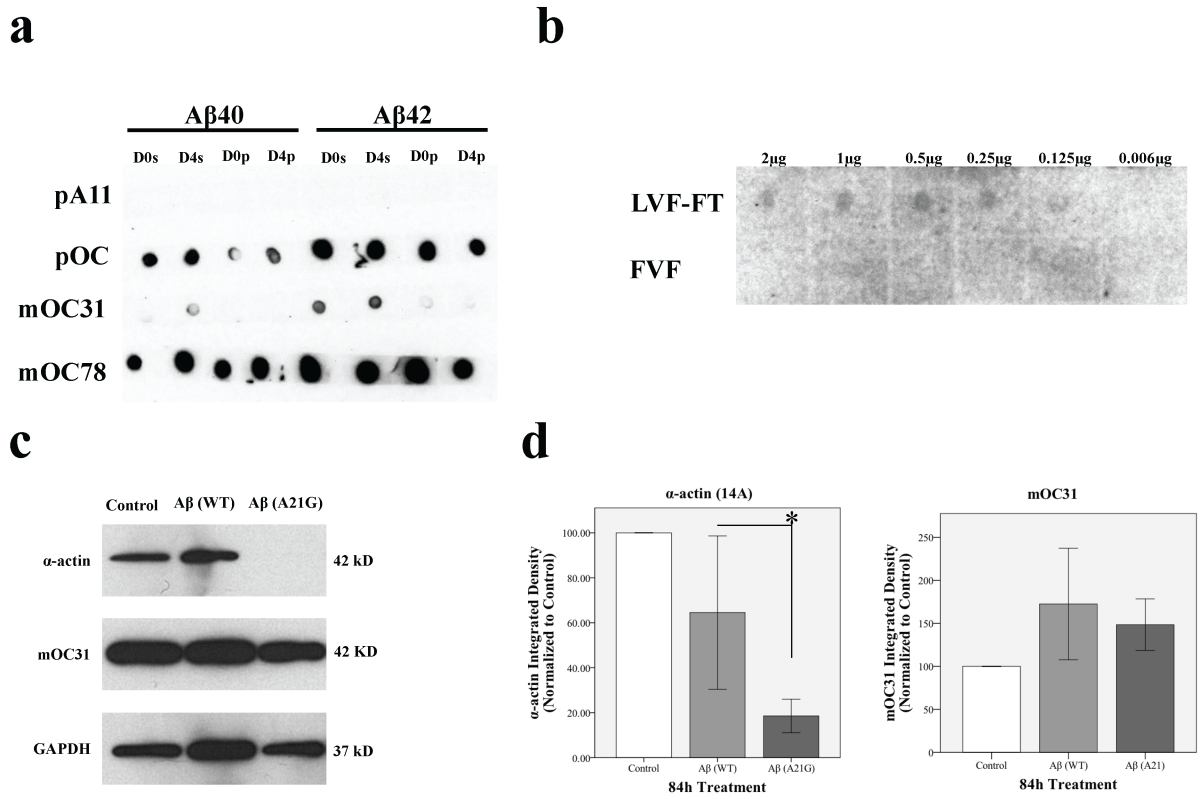

Figure 3.1 mOC31 recognizes loop adjacent to glutamic and aspartic acid in fibrillar oligomers of Aβ and loss of α-actin immunoreactivity is coupled with an increase in mOC31 amyloid immunoreactivity in HBVSMC lysates. (a) Characterization of freshly (D0) and four day aggregated (D4) preperations of Aβ40 and Aβ42 after 100,000 x g centrifugation. 1µL of solution was spotted on to nitrocellulose from the 100,000 x g supernant (DXs) and (DXp) and probed with pA11, pOC, mOC31, mOC78. (b) Two fragments of Aβ (LVF-FT: Aβ17-36, LVF Aβ17-23 and 30-36) were spotted on nitrocellulose and probed with mOC31. (c) Western blot of cell lysate from human vascular smooth muscle cells treated with wild-type (WT), Flemish (A21G) Aβ, or control for 84 hours and probed with antibodies: α-actin, mOC31 and GAPDH. (d) Quantification of α-actin and mOC31 Western blots by ImageJ. Bars indicate the mean ±sem, * $p < 0.05$.

Loss of α-actin immunoreactivity is coupled with an increase in mOC31 amyloid immunoreactivity in HBVSMC treated with wild-type and mutant Aβ

We previously showed that a unique vascular amyloid immunoreactivity was correlated with the loss of α-actin staining in human and Tg-mouse models of AD brain. To specifically determine the effect Aβ has on vascular smooth muscle cells we developed an *in vitro* cell model utilizing primary human brain vascular smooth muscle cells (HBVSMC) treated with 2μM freshly prepared synthetic Aβ40 peptide. Total cell lysate from HBVSMC treated for 84 hours with either wild-type (wt) or mutant peptide (A21G) Aβ40 (Aβ-WT and Aβ-A21G, respectively) were subjected to SDS-PAGE and Western blotting. We found a trend that mirrored our immunofluorescent studies in human and Tg-mouse models of AD brain; that is, increases in mOC31 immunoreactivity are accompanied by decreases in α-actin immunoreactivity (Figure 3.1-c). Densitometric analysis showed a statistically significant decrease in HBVSMC α-actin after 84 hours of Aβ-A21G treatment when compared to control buffer treated cells ($p<0.01$) (Figure 3.1-d). HBVSMC were probed with mOC31, anti-α-actin, and philloidin after being cultured on glass coverslips and treated with Aβ-WT or Aβ-A21G for 84 hours (Figure 3.2-a). Triple-label immunofluorescence and quantitative analysis of the volume and fluorescence intensity showed a dramatic and statistically significant decrease in both α-actin immunoreactivity and philloidin fluorescence after treatment with Aβ-WT and Aβ-A21G for 84 hours when compared to control buffer ($p<0.01$ and $p<0.05$, respectively) Figure 3.2-b,d). In contrast, mOC31 immunoreactivity dramatically increased after Aβ-WT and Aβ-A21G treatment ($p<0.001$) (Figure 3.2-c). These findings suggest that, *in vitro*, Aβ peptide is sufficient to causes a loss of smooth muscle actin immunoreactivity in HBVSMCs measured by Western blotting

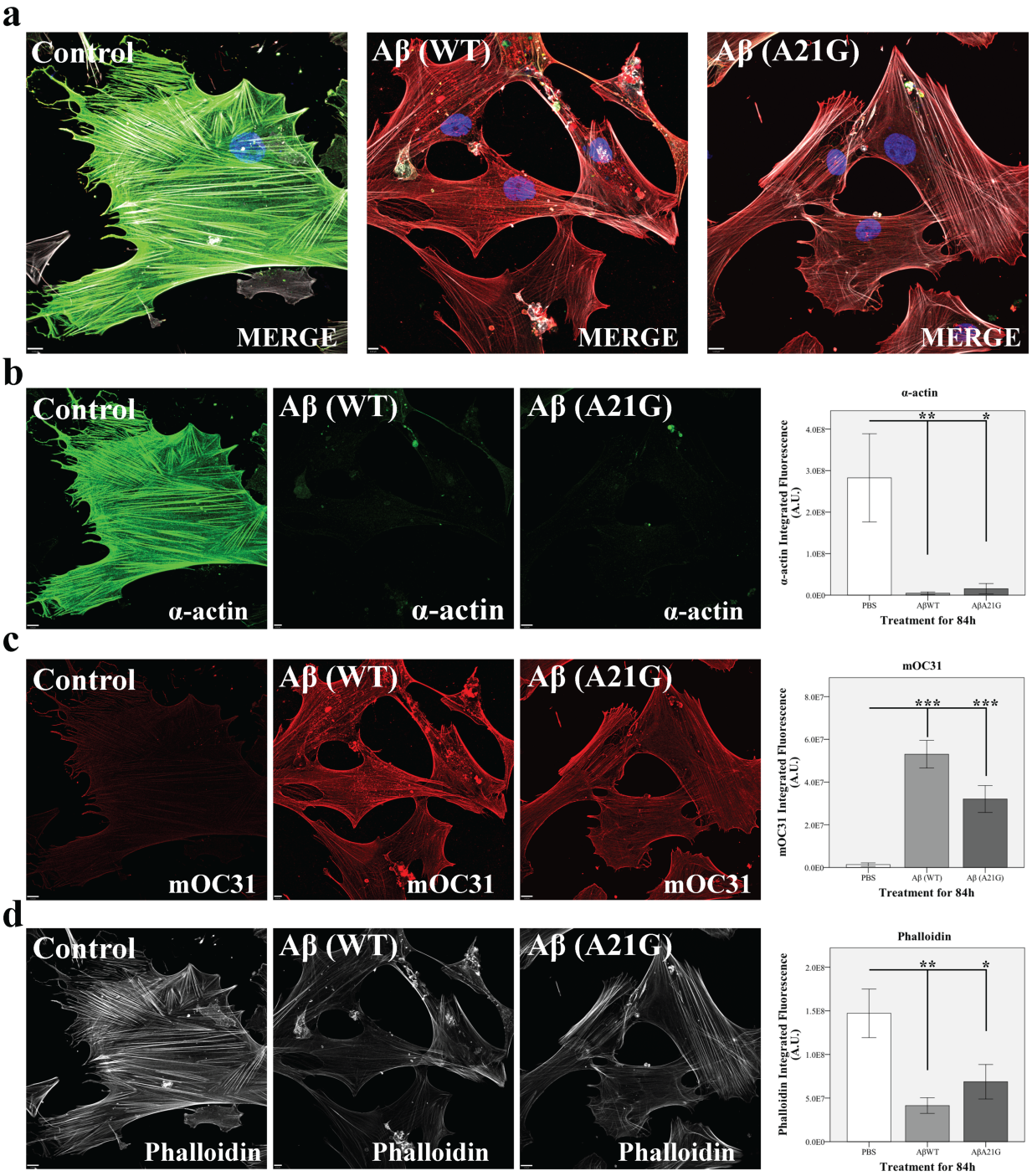

Figure 3.2 Loss of α-actin immunoreactivity is correlated with an increase in mOC31 amyloid immunoreactivity in confocal micrographs of HBVSMC. (a) Confocal micrographs were obtained from human brain vascular smooth muscle cell treated with wild-type Aβ (Aβ WT), Flemish (Aβ A21G), or control buffer for 84 hours. For (b) α-actin, (c) mOC31, and (d) Phalloidin the fluorescence integrated density was quantified in the analytical software Volocity. Bars indicate the mean ±sem, * p <0.05 ** p <0.01 *** p <0.001. Scale bar 12 μm.

analysis and triple-label confocal analysis.

Stimulation with Aβ is sufficient to cause lysosomal / endosomal vesicle leakage in HBVSMCs

Since our *in vitro* model depends on exogenous application Aβ peptide, we were interested in determining whether HBVSMCs suffered from lysosomal leakage in response to Aβ treatment. To address this we pre-loaded endosomes and lysosomes of HBVSMCs cultured on glass coverslips with media containing a non-membrane permeable fluidic dye, Lucifer yellow CH, that was subsequently taken up by the cells and trapped in lysosomal compartments. Lucifer yellow CH-treated cells were then treated with control buffer, Aβ-WT or Aβ-A21G for 12 and 24

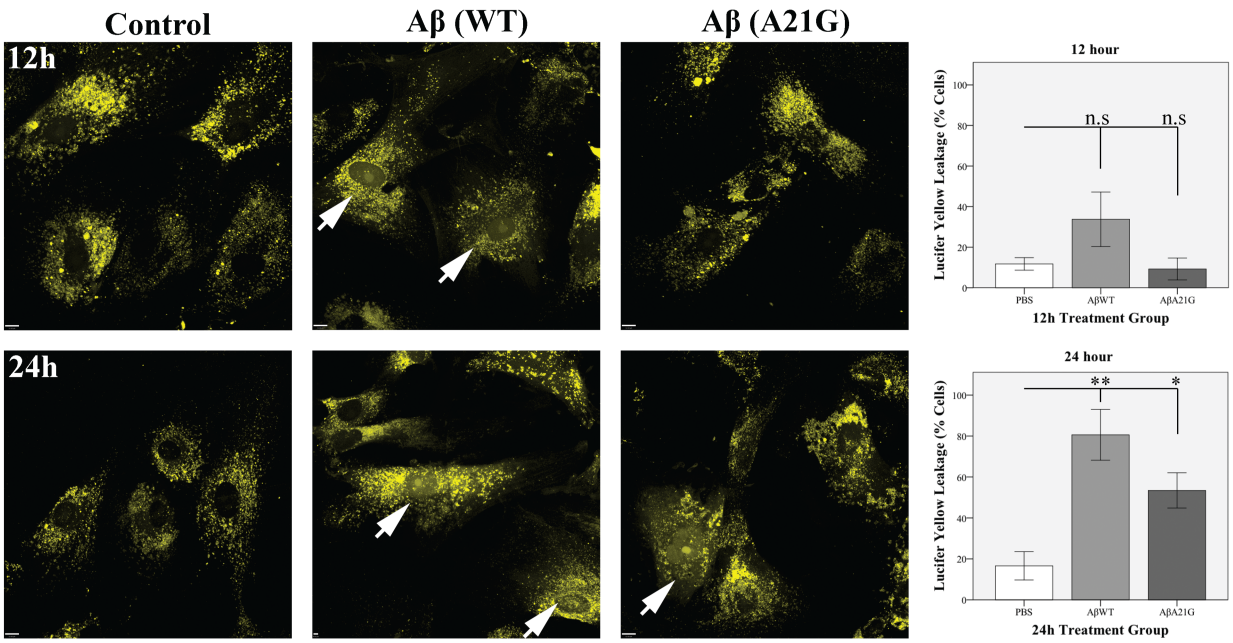

Figure 3.3 Stimulation with Aβ is sufficient to cause lysosomal / endosomal vesicle leakage in HBVSMC. Human brain vascular smooth muscle cells (HBVSMC) were pre-loaded with the non-membrane permeable fluidic dye Lucifer Yellow (LY). Media was exchanged with freshly prepared Aβ and cells were fixed with paraformaldehyde after indicated time (12h or 24h). Leakage of LY into cytosol and nuclear compartments was determined by the presence of dye in cytosol and nucleus (arrowhead). Bars indicate mean ± sem, n.s = not significant, * $p<0.05$, ** $p<0.01$. Scale bar 12 µm.

hours, paraformaldehyde-fixed and imaged on a confocal microscope (Figure 3.3). We found that after 24 hours Aβ-WT and Aβ-A21G caused lysosomal leakage as evidence of Lucifer yellow in the cytoplasm and nucleus. We quantified the proportion of cells that exhibited nuclear Lucifer yellow CH and found that Aβ treatment enhanced lysosomal leakage 2-3 fold. These findings provide one possible avenue in which exogenous Aβ can center the cell and have a pathogenic effect. In these experiments Aβ-WT was more efficient at disrupting the lysosomal compartment in which they are contained. These results may be related to the fact that Aβ-WT aggregates more aggressively than Aβ-A21G *in vitro.*

Treatment with wild-type Aβ40 results in a loss of membrane integrity with minimal cell death

We examined whether the preparation of synthetic Aβ in our *in vitro* model is cytotoxic to HBVSMCs; here we treated cultured cells with synthetic Aβ-WT peptide that was prepared seven days (D7) prior, three days (D3) prior, or same day (D0) as experiment. HBVSMCs treated with 2 μM Aβ for 72 hours showed significant reduction in cell viability in D0 Aβ-WT treatment as compared to control buffer treated cells ($p<0.05$) (Figure 3.4). In this assay cells were viable if they maintained esterase activity which allowed the membrane permeable and non fluorescent calcein AM to be processed to membrane impermeable and fluorescent calcein. Membrane impermeable Ethidium homo dimer was also included in this assay to determine cytoplasmic membrane integrity of treated and non-treated cells. Dead cells in this assay were calcein^{-}/ ethidium^{+}. Synthetic Aβ-WT peptide that was prepared D7 and D3 prior to experiment showed no significant loss of cell viability compared to buffer treated controls. In both D0 and D3 Aβ treatment conditions membrane integrity was significantly compromised as evidence of nuclear

ethidium homo dimer and intact esterase activity (ethidium^{+}/calcein^{+}). These data suggest that treatment with freshly prepared Aβ-WT is the most cytotoxic to HBVSMCs, presumably because they contain the highest concentration of soluble aggregates and available monomer. At 2μM Aβ,

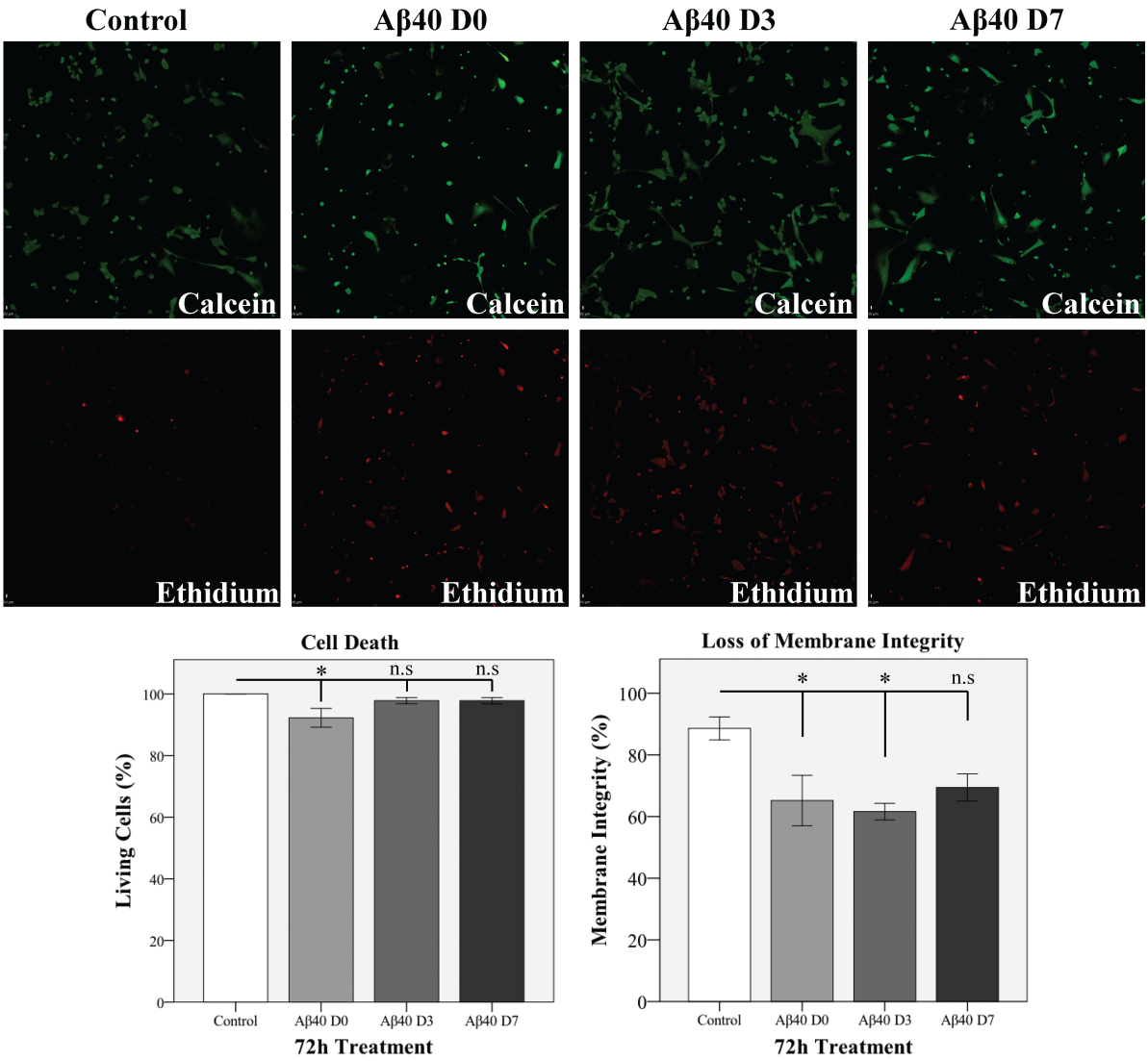

Figure 3.4 Treatment with wild-type Aβ40 results in a loss of membrane integrity with minimal cell death. Human brain vascular smooth muscle cells were treated with freshly prepared A β (D0) or pre-aggregated (D3,D7) for 72 hours. Media was replaced with fresh media containing both Ehidium bromide homo dimer and Calcein AM and imaged on a confocal microscope with 20x objective. Confocal micrographs were imported into analytical software Volocity to automatically aquire counts for cells postive for Ethidium and/or Calcein. Bars indicate mean ± sem, * p <0.05 n.s-not significant.

both D0 and D3 treatment conditions resulted in Aβ-related loss of membrane integrity which suggest that the concentration of soluble aggregates is important for the disruption of membrane integrity; this is consistent with the widely excepted idea that soluble oligomers are cytotoxic and disruptive to cell homeostasis [107].

mOC31 does not recognize recombinant α-smooth muscle actin

We have recapitulated the loss of α-actin immunoreactivity in HBVSMCs after treatment with freshly prepared Aβ *in vitro* and provided evidence that exogenously administered aggregates can leak out of lysosomal compartments once internalized by the cell. Western blot analysis revealed an unanticipated finding, the apparent size of the molecule recognized by mOC31 was approximately 42kD (Figure 3.1-c), coincidently the same size as α-actin. Probing the blot simultaneously with mOC31 and anti-A-actin confirmed that both antibodies were recognizing the same apparent size band (data not shown). We investigated whether mOC31 could recognize pure α-actin and if synthetic Aβ could cause a conformational change in a cell free system (Figure 3.5). We mixed various concentrations of Aβ40-WT (0 μM, 0.001 μM, 0.1 μM, and 10 μM) with a consistent 1μM concentration of recombinant α-actin. We found that at the concentrations tested Aβ-WT did not causes the loss of α-actin immunoreactivity seen in human, mouse, and primary cell culture. In the absence of cells mOC31 does not react with the α-actin 42kD band but did recognize low-molecular weight species corresponding to Aβ dimer and high-molecular weight aggregates as you might expect for anti-fibrillar antibody. These data suggest that the epitope recognized *in vitro* potentially require post-translational modifications or interaction with Aβ that cannot be recapitulated in our current test tube paradigm.

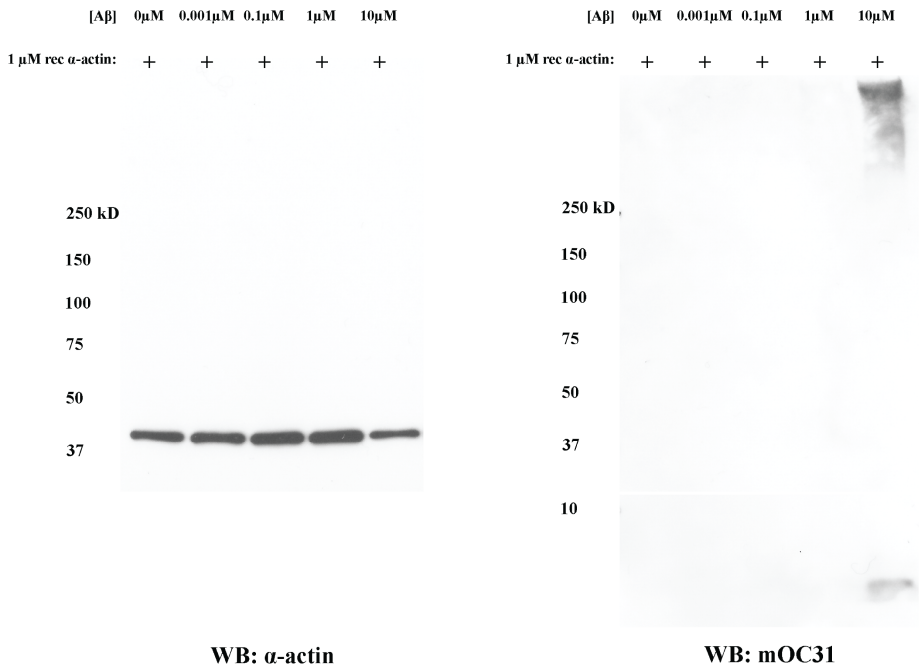

Figure 3.5 mOC31 does not recognize recombinant α-smooth muscle actin. Solutions of 1μM recombinant α-actin and synthetic Aβ (0, 0.001, 0.1, 1, 10μM) were prepared and seperated by SDS-PAGE. Western blots were carried out with anti-α-actin (1A4) and mOC31, the antibodies recognized distinct bands.

mOC31 amyloid antibody immunoprecipitates a SDS stable complex of α-actin and Aβ in HBVSMCs

Western blotting revealed that mOC31 and α-actin recognized a molecule with the apparent weight of 42kD, we decided to investigate whether a direct interaction existed between the amyloid recognized by mOC31 and α-actin. We treated HBVSMC with Aβ-WT, Aβ-A21G, and buffer control then subjected total cell lysates to immunoprecipitation with mOC31 and IgG control (Figure 3.6). We found that mOC31 was able to pull down material that had immunoreactivity for α-actin. Two unique bands that were not present in the IgG control ran at the apparent molecular weight of 46kD and 50kD in Aβ-WT and Aβ-A21G, but not control

buffer treated conditions. Western blots were stripped and reprobed with anti-Aβ (6E10); both unique bands had 6E10 immunoreactivity. Together these results demonstrate that not only do Aβ and α-actin interact, as evidence of the shift in apparent size, some fraction of both proteins form

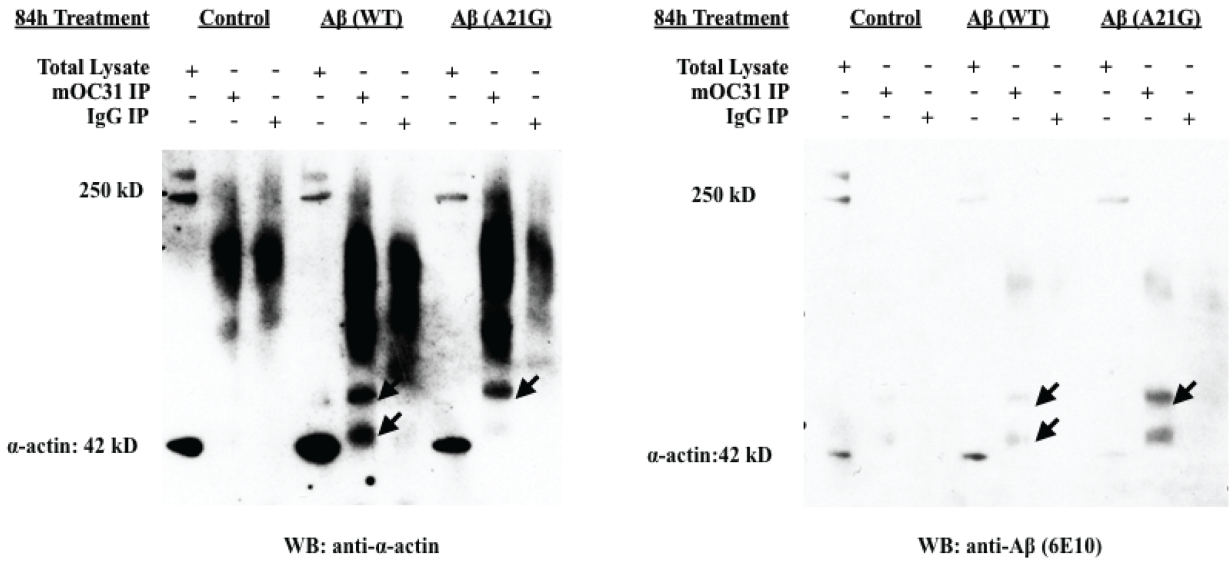

Figure 3.6 mOC31 amyloid antibody immunoprecipitates a SDS stable complex of α-actin and Aβ in HBVSMC. Human vascular smooth muscle cells were treated with freshly prepared Aβ (WT), Aβ (A21G), or control buffer for 84h hours. Cell lysates were immunoprecipitated with mOC31 and IgG isotype control and seperated on SDS-PAGE. Western blots with anti-α-actin and anti-Aβ (6E10) show unique 46kD and 50kD band in the immunoprecipitated lanes that are not present in contol IgG lanes.

a SDS stable complex with one or two molecules of Aβ (46kD and 50kD, respectively).

Discussion

The use of brain derived vascular smooth muscle cells to study cerebral amyloid angiopathy dates back over 20 years [108]. A great deal has been gleaned from their use as a model; for example: VSMC express and secrete Aβ, cytotoxicity of various familial forms of CAA, loss of smooth muscle α-actin in response to Aβ [109,102,31]. Here we use primary human brain vascular smooth muscle cells to investigate the pathological effects of mOC31 immunoreactivity.

In Chapters 1 and 2 we characterized an anti-fibrillar Aβ rabbit monoclonal mOC31 and report that the accumulation of mOC31 immunoreactivity in brain arterioles is negatively correlated with α-actin immunoreactivity. We demonstrated here that 2-5μM of freshly prepared Aβ is sufficient to reproduce this phenotype *in vitro* (Figure 3.1 and 4.2). Western blotting HBVSMC treated with the addition of Aβ to the media resulted in statistically significant decrease of α-actin as observed by Western blotting, with Aβ40-A21G and not Aβ40-WT (vs buffer control treated cells). Confocal microscopy revealed significant decreases in α-actin immunoreactivity by as much as 10-fold for Aβ40-WT and Aβ40-A21G (Figure 3.2). One possible explanation for the loss of sensitively seen with Western blotting could be related to sample processing. In confocal microscopy antibodies are exposed to epitopes that are more or less fixed in a "native" state by paraformaldehyde; this is not the case for Western blotting. Here proteins are denatured with sodium dodecyl sulfate (SDS) buffer and heat before exposure to antibody; given that many antibodies have some degree of conformation dependence a loss of sensitivity is not out of the realm of possibility. In this study, we examined the effects of exogenous administration of Aβ40-WT and Aβ40-A21G on the integrity of lysosomal compartments. We found that leakage occurs as evidenced by the redistribution of Lucifer Yellow into the cytoplasm and nucleus (Figure 3.3). Similar experiments with Aβ40-WT were carried out in SH-SY5Y cells and here it was reported that in those cells Aβ40-WT did not cause lysosomal leakage suggesting a unique susceptibility of VSMCs to Aβ40-WT and Aβ40-A21G [104]. We found that freshly prepared Aβ-WT was most cytotoxic to HBVSMCs, presumable because they contain the highest concentration of soluble aggregates and available monomer; the small effect size should be noted (Figure 3.4). These results are consistent with published results for Aβ40-WT and Aβ40-A21G and were

repeated to rule out cytotoxicity as the pathogenic consequence of mOC31 immunoreactivity [31]. In our initial characterization of cell lysates we learned that mOC31 Western blotted a molecule that ran at 42kD, the same apparent size as α-actin (Figure 3.1). We used recombinant α-actin and synthetic Aβ to confirm the specificity of both α-actin antibody and mOC31 antibody; we showed that in mixtures of recombinant α-actin and synthetic Aβ, only Aβ was recognized by mOC31 and only α-actin was recognized by anti-α-actin. We investigated whether an interaction existed between Aβ and α-actin by immunoprecipitating HBVSMC lysate with mOC31 antibody and found an interaction in Aβ-WT and Aβ-A21G treated cells. The immunoprecipitated material is positive for anti-Aβ antibody (6E10) and appears to be a complex comprised of either one or two molecules of Aβ per molecule of α-actin. This interaction is significant because it may explain the loss of α-actin immunoreactivity observed. One hypothesis is Aβ could interact with α-actin and physically mask the epitope required for anti-α-actin immunoreactivity. The interaction could have a consequential effect of interfering with α-actin polymerization, supported by the negative correlation between mOC31 immunoreactivity and phalloidin binding to f-actin. Another possibility is the interaction between Aβ and α-actin causes a change in the secondary and tertiary structure that also affect the epitope of anti-α-actin immunoreactivity. Determining the exact nature of the Aβ and α-actin interaction will require further investigation, including structural analysis of this complex with mOC31 antibody.

CHAPTER 4

Summary and Conclusions

The shortcoming of current therapeutics implores us to re-evaluate the amyloid hypothesis and explore parallels from other diseases caused by amyloidosis. Alzheimer's disease (AD), prion disease, and cerebral amyloid angiopathy (CAA) all arise from structural changes in the protein backbone where a natively folded protein becomes mis-folded and enriched in β-sheets. Developing effective immunotherapy treatments for AD and other amyloidosis rests in our ability to target specific toxic species of amyloid. This task is complicated by the fact that the underlying β-sheet structure of aggregates favor two conformations, including parallel β-sheets and anti-parallel β-sheets. Parallel β-sheets make up the underlying structure of soluble fibrillar oligomers and insoluble fibrils. Prefibrillar oligomers arise from a separate aggregation pathway that consist of proteinaceous aggregates that have anti-parallel β-sheets; this amyloid structure is transient and immunologically distinct from fibrillar oligomers and fibrils. Structural data obtained by X-ray crystallography and solid-state NMR provide evidence to suggest that structural heterogeneity within these two classes of amyloid exist. Studies using serum developed to recognize these distinct classes of β-sheet structure have contributed immensely to the understanding of Alzheimer's disease pathology; most notably, the landmark finding that common amyloid structure implies common mechanism of pathogenesis [69]. To date, the generation of monoclonal antibodies against prefibrillar and fibrillar amyloid has proven useful in not only understanding amyloid heterogeneity but in investigating which epitopes are associated with pathology and contribute to disease phenotype.

In this dissertation, we have shown that polymorphism in amyloid can be differentiated by our panel of 29 monoclonal antibodies as evidenced by the differential temporal, spatial, and subcellular localization observed in AD and Tg-mouse models of AD (Chapter 1 and Chapter 2). Specifically, we showed that conformational epitopes recognized by our panel associate with unique plaque morphology or different subcellular locations of intracellular amyloid. We highlight that the location of mOC78 epitope is dynamic and indicative of disease progression. In the 3xTg-AD mouse, intracellular mOC78 immunoreactivity accumulates before cognitive decline, translocates to the nucleus at the approximate age behavior deficits are reported, and ultimately associate with amyloid plaques. The observation that intracellular aggregates and extracellular amyloid share the same conformational epitope supports the hypothesis that neurons are the nidus of the senile plaques. Our panel of monoclonal antibodies also revealed a unique epitope of amyloid immunoreactivity localized to brain vasculature. The characterization of mOC31 immunoreactivity showed that vascular and parenchymal amyloid are structurally disparate evidenced by the absence of the mOC31 epitope in plaque amyloid. The majority of mOC31 immunoreactivity did not colocalize with current probes for investigating vascular amyloid (e.g. anti-Aβ (6E10) or Thioflavin S) suggesting a previously uncharacterized type of vascular amyloidosis. The unique histopathological profiles of mOC31 and mOC78 immunoreactivities seem to suggest that structural diversity in amyloid dictates more than the aggregation pathway and kinetics of prefibrillar oligomers, fibrillar oligomers, and fibrils; these pathology associated epitopes correlate with disease progression, the onset of cognitive decline, and spatial localization of amyloid deposition. We hypothesized that the characterization of

mOC31 immunoreactivity in Alzheimer's disease and Tg-mouse models of AD would reveal a unique pathology in Alzheimer's disease related to CAA.

We found that mOC31 immunoreactivity specifically deposited within vascular smooth muscle cells (VSMC) of the brain and is correlated with the progression of plaque pathology in AD and age in 5XFAD-Tg mice (Chapter 1 and Chapter 2). We observed significant levels of mOC31-positive vascular amyloidosis in the hippocampus at intermediate stages of plaque pathology that plateaus thereafter; the degree to which vascular amyloidosis occurs is influenced by the apoE4 isoform. These results suggest that the amyloid cascade hypothesis applies to mOC31-positive vascular amyloid; that is, Aβ is the root of the pathogenic agent. Furthermore, factors that influence levels of Aβ, such as mutations in *APP* or isoforms of *APOE*, affect the degree to which mOC31-positive amyloid deposits into VSMC. The observation that amyloid plaques do not correlate with cognitive decline suggests that not all amyloid strains are pathogenic. Vascular amyloid recognized by mOC31 was shown to negatively correlate with α-actin immunoreactivity in VSMCs in a cohort of 21 human brain samples and has an inflammatory component (Chapter 2). Cytosolic immunoreactivity of the systemic inflammatory marker, HMBG1, colocalized with mOC31 immunoreactivity in vessels of AD brain. In arteriosclerosis, the secretion of HMGB1 by both endothelial and VSMCs has been reported and with regard to VSMCs has been shown to promote the conversion from a contractile to a proliferative phenotype. Fibrillar conformations of amyloid also activate the receptor for HMGB1, Receptor for Advanced Glycation End Products (RAGE), and function blocking antibodies or ligands may provide a therapeutic target to treat symptoms related to mOC31-positive CAA [110]. Likewise, immunotherapy directed

toward pathogenic conformations of fibrillar amyloid, such as mOC31-positive amyloid, could alleviate the inflammatory component in VSMCs.

To investigate the pathological role of Aβ we developed an *in vitro* model utilizing primary human brain vascular smooth muscle cells (HBVSMC). By treating cultures of HBVSMC with wild-type and mutant Aβ we were able to reproduce the correlations seen in human and Tg-mouse models of AD brain, that is, exogenous Aβ resulted in a decrease in α-actin immunoreactivity that correlated with an increase in mOC31 immunoreactivity (Chapter 3). HBVSMC suffer from lysosomal leakage in the presence of Aβ, providing a potential avenue for the entry of Aβ into the cell. In fact, we learned that Aβ and α-actin directly interact and form a heat and detergent stable complex. The results from our *in vitro* HBVSMC model are intriguing because they directly show that the accumulation of Aβ causes lysosomal leakage and a loss of α-actin immunoreactivity in the absence of cell death. However, the Aβ-induced loss of α-actin immunoreactivity raises two questions: (1) does Aβ directly mask the α-actin antibody epitope and (2) could α-actin expression be affected. Although the current set of experiments do not directly address these questions, two independent experiments suggest the masking is related to the Aβ/α-actin interaction rather loss of α-actin expression. First, gel-electrophoresis of lysates from wild-type Aβ treated HBVSMC and Western blot analysis with α-actin antibody showed levels of α-actin protein that was comparable to control treated HBVSMC. Second, analysis of α-actin immunoreactivity by fluorescent confocal microscopy of HBVSMC treated with wild-type Aβ showed a dramatic decrease in α-actin immunoreactivity for this condition. The simplest interpretation for these results is Aβ masks the α-actin epitope in wild-type Aβ treated HBVSMC

that is unmasked under SDS-PAGE and Western blotting. The findings presented in this dissertation are both novel and significant to AD and CAA in that they elucidate a novel epitope of Aβ that is correlated with a specific disease phenotype in VSMCs.

We propose the following model that illustrates VSMCs response to soluble fibrillar oligomers of Aβ (Figure 4.1). In the model, VSMC change from a contractile to proliferative phenotype in the presence of HMGB1 and soluble wild-type or flemish Aβ. Proliferative VSMC become more phagocytic and take up exogenous Aβ, allowing for it to accumulate and causes lysosomal leakage. Internalized Aβ interacts with α-actin that may directly mask the α-actin antibody epitope or indirectly mask the α-actin antibody epitope through a conformational change. We show that fibrillar oligomers of Aβ directly interact with α-actin and disrupts levels of polymerized actin (f-actin) in VSMC. The phenotypic change correlated with HMGB1 and Aβ

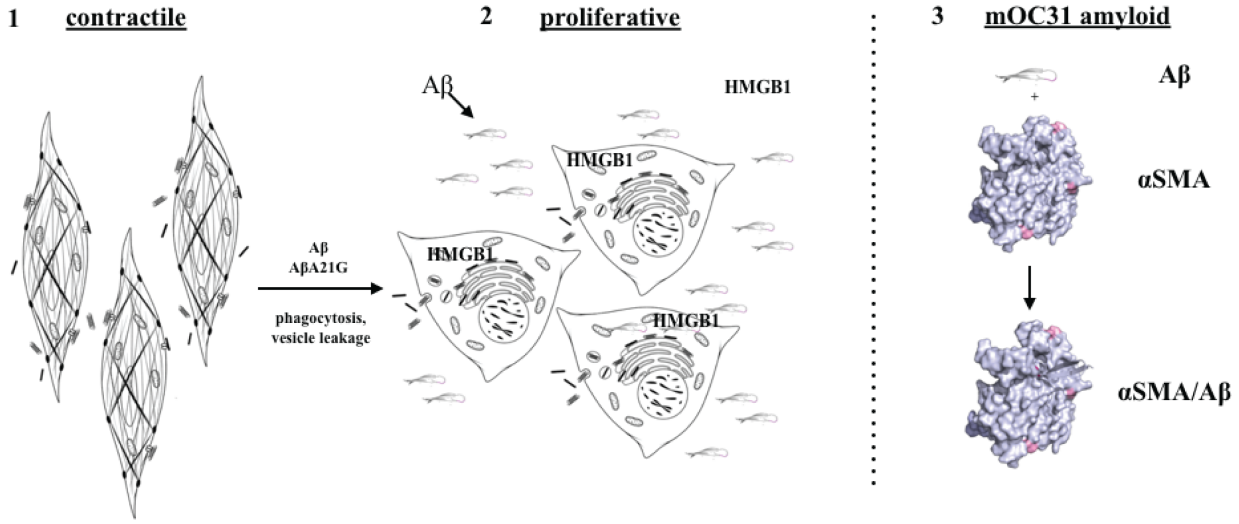

Figure 4.1 Vascular smooth muscle cells response to soluble Aβ. (1) In the presence of HMGB1 and soluble wild-type or flemish Aβ VSMC change from a contractile to proliferative phenotype. (2) Proliferative VSMC become more phagocytic and take up exogenous Aβ, allowing for the accumulation and cause of vesicle leakage. (3) Internalized Aβ interacts with α-actin that may directly mask the anti-actin epitope or facilitate a coformational change. Together a loss of function results in deficiency in blood flow self regulation reported in AD.

represent a loss of function in VSMC that could explain the deficiency in blood flow self regulation reported in AD [52].

The vascular amyloidosis present in AD is often an under appreciated lesion and warrants further investigation. Future studies should be directed toward investigating the structures adopted by the soluble aggregates formed from wild-type and flemish Aβ40; using mOC31 to co-crystal Aβ may help facilitate an otherwise daunting endeavor. Understanding the underlying β-sheet structures of these soluble oligomers would be instrumental in determining what differentiates mOC31-positive fibrillar oligomers from parenchymal plaques. In characterizing the mOC31 antibody we described a novel cerebral vascular amyloidosis that follows disease progression in Tg-mouse models of AD and AD. Investigating the mechanism underlying the inflammatory component of mOC31 immunoreactivity is also an intriguing avenue of inquiry. In particular, what are the signals involved downstream of HMGB1 that regulate the observed conversion of VSMC phenotype? Can this conversion be blocked and does it affect mOC31 immunoreactivity? Translational studies with collaborators, although preliminary, have shown the presence of these aggregates in cerebral spinal fluid and longitudinal studies may find that mOC31 is a predictive biomarker for the progression of AD. Additionally, positron emission tomography with mOC31 antibody has had success differentiating wild-type from TgCRND8 mice and follow-up studies in human subjects would be a worthwhile endeavor [111]. If CAA is associated with a loss of blood flow self-regulation, the targeting of vascular amyloid by mOC31 may prove to be a beneficial immunotherapy alone and mouse studies targeting the removal of vascular amyloid may slow cognitive decline while leaving parenchymal plaques untouched.

REFERENCES

1 Wadman, M. in *Nature* Vol. 485 426-427 (2012).

2 Vinters, H. V. Emerging concepts in Alzheimer's disease. *Annu Rev Pathol* **10**, 291-319, doi:10.1146/annurev-pathol-020712-163927 (2015).

3 Henryk M. Wisniewski M.D. and Robert D. Terry, M. D. *Reexamination of the Pathogenesis of the Senile Plaque*. (Progress in Neuropathology, 1973).

4 Glenner, G. G. & Wong, C. W. Alzheimer's disease and Down's syndrome: sharing of a unique cerebrovascular amyloid fibril protein. *Biochem Biophys Res Commun* **122**, 1131-1135 (1984).

5 Masters, C. L. *et al.* Neuronal origin of a cerebral amyloid: neurofibrillary tangles of Alzheimer's disease contain the same protein as the amyloid of plaque cores and blood vessels. *EMBO J* **4**, 2757-2763 (1985).

6 Prelli, F., Castano, E., Glenner, G. G. & Frangione, B. Differences between vascular and plaque core amyloid in Alzheimer's disease. *J Neurochem* **51**, 648-651 (1988).

7 Kang, J. *et al.* The precursor of Alzheimer's disease amyloid A4 protein resembles a cell-surface receptor. *Nature* **325**, 733-736, doi:10.1038/325733a0 (1987).

8 Tanzi, R. E. *et al.* Amyloid beta protein gene: cDNA, mRNA distribution, and genetic linkage near the Alzheimer locus. *Science* **235**, 880-884 (1987).

9 Masters, C. L. *et al.* Amyloid plaque core protein in Alzheimer disease and Down syndrome. *Proc Natl Acad Sci U S A* **82**, 4245-4249 (1985).

10 Levy, E. *et al.* Mutation of the Alzheimer's disease amyloid gene in hereditary cerebral hemorrhage, Dutch type. *Science* **248**, 1124-1126 (1990).

11 Yoshikai, S., Sasaki, H., Doh-ura, K., Furuya, H. & Sakaki, Y. Genomic organization of the human amyloid beta-protein precursor gene. *Gene* **87**, 257-263 (1990).

12 Tcw, J. & Goate, A. M. Genetics of beta-Amyloid Precursor Protein in Alzheimer's Disease. *Cold Spring Harb Perspect Med* **7**, doi:10.1101/cshperspect.a024539 (2017).

13 Citron, M. *et al.* Mutation of the Beta-Amyloid Precursor Protein in Familial Alzheimers-Disease Increases Beta-Protein Production. *Nature* **360**, 672-674, doi:DOI 10.1038/360672a0 (1992).

14 Nilsberth, C. *et al.* The 'Arctic' APP mutation (E693G) causes Alzheimer's disease by enhanced Abeta protofibril formation. *Nat Neurosci* **4**, 887-893, doi:10.1038/nn0901-887 (2001).

15 Wisniewski, T., Ghiso, J. & Frangione, B. Peptides homologous to the amyloid protein of Alzheimer's disease containing a glutamine for glutamic acid substitution have accelerated amyloid fibril formation. *Biochem Biophys Res Commun* **180**, 1528 (1991).

16 Hendriks, L. *et al.* Presenile dementia and cerebral haemorrhage linked to a mutation at codon 692 of the beta-amyloid precursor protein gene. *Nat Genet* **1**, 218-221, doi:10.1038/ng0692-218 (1992).

17 Suzuki, N. *et al.* An increased percentage of long amyloid beta protein secreted by familial amyloid beta protein precursor (beta APP717) mutants. *Science* **264**, 1336-1340 (1994).

18 Hardy, J. Amyloid, the presenilins and Alzheimer's disease. *Trends Neurosci* **20**, 154-159 (1997).

19 Jonsson, T. *et al.* A mutation in APP protects against Alzheimer's disease and age-related cognitive decline. *Nature* **488**, 96-99, doi:10.1038/nature11283 (2012).
20 Scheuner, D. *et al.* Secreted amyloid beta-protein similar to that in the senile plaques of Alzheimer's disease is increased in vivo by the presenilin 1 and 2 and APP mutations linked to familial Alzheimer's disease. *Nature Medicine* **2**, 864-870, doi:DOI 10.1038/nm0896-864 (1996).
21 De Strooper, B. *et al.* Deficiency of presenilin-1 inhibits the normal cleavage of amyloid precursor protein. *Nature* **391**, 387-390, doi:10.1038/34910 (1998).
22 Fernandez, M. A., Klutkowski, J. A., Freret, T. & Wolfe, M. S. Alzheimer presenilin-1 mutations dramatically reduce trimming of long amyloid beta-peptides (Abeta) by gamma-secretase to increase 42-to-40-residue Abeta. *J Biol Chem* **289**, 31043-31052, doi:10.1074/jbc.M114.581165 (2014).
23 Arriagada, P. V., Growdon, J. H., Hedley-Whyte, E. T. & Hyman, B. T. Neurofibrillary tangles but not senile plaques parallel duration and severity of Alzheimer's disease. *Neurology* **42**, 631-639 (1992).
24 Doody, R. S. *et al.* A Phase 3 Trial of Semagacestat for Treatment of Alzheimer's Disease. *The New England journal of medicine* **369**, 341-350, doi:10.1056/NEJMoa1210951 (2013).
25 Salloway, S. *et al.* Two Phase 3 Trials of Bapineuzumab in Mild-to-Moderate Alzheimer's Disease. *The New England journal of medicine* **370**, 322-333, doi:10.1056/NEJMoa1304839 (2014).
26 Doody, R. S. *et al.* Phase 3 Trials of Solanezumab for Mild-to-Moderate Alzheimer's Disease. *The New England journal of medicine* **370**, 311-321, doi:10.1056/NEJMoa1312889 (2014).
27 Sevigny, J. *et al.* The antibody aducanumab reduces Abeta plaques in Alzheimer's disease. *Nature* **537**, 50-56, doi:10.1038/nature19323 (2016).
28 Revesz, T. *et al.* Cerebral amyloid angiopathies: a pathologic, biochemical, and genetic view. *Journal of neuropathology and experimental neurology* **62**, 885-898 (2003).
29 Hatami, A., Albay, R., Monjazeb, S., Milton, S. & Glabe, C. Monoclonal antibodies against Aβ42 fibrils distinguish multiple aggregation state polymorphisms in vitro and in Alzheimer disease brain. *The Journal of biological chemistry* **289**, 32131-32143, doi:10.1074/jbc.M114.594846 (2014).
30 Grabowski, T. J., Cho, H. S., Vonsattel, J. P., Rebeck, G. W. & Greenberg, S. M. Novel amyloid precursor protein mutation in an Iowa family with dementia and severe cerebral amyloid angiopathy. *Ann Neurol* **49**, 697-705 (2001).
31 Van Nostrand, W. E., Melchor, J. P., Cho, H. S., Greenberg, S. M. & Rebeck, G. W. Pathogenic Effects of D23N Iowa Mutant Amyloid -Protein. *The Journal of biological chemistry* **276**, 32860-32866, doi:10.1074/jbc.M104135200 (2001).
32 Vinters, H. V. Cerebral amyloid angiopathy. A critical review. *Stroke* **18**, 311-324 (1987).
33 Itoh, Y., Yamada, M., Hayakawa, M., Otomo, E. & Miyatake, T. Cerebral Amyloid Angiopathy - a Significant Cause of Cerebellar as Well as Lobar Cerebral-Hemorrhage in the Elderly. *J Neurol Sci* **116**, 135-141, doi:Doi 10.1016/0022-510x(93)90317-R (1993).
34 O'Donnell, H. C. *et al.* Apolipoprotein E genotype and the risk of recurrent lobar intracerebral hemorrhage. *The New England journal of medicine* **342**, 240-245, doi:10.1056/NEJM200001273420403 (2000).

35 Xu, Q. *et al.* Profile and regulation of apolipoprotein E (ApoE) expression in the CNS in mice with targeting of green fluorescent protein gene to the ApoE locus. *J Neurosci* **26**, 4985-4994, doi:10.1523/JNEUROSCI.5476-05.2006 (2006).
36 Masliah, E. *et al.* Neurodegeneration in the Central-Nervous-System of Apoe-Deficient Mice. *Exp Neurol* **136**, 107-122, doi:DOI 10.1006/exnr.1995.1088 (1995).
37 DeMattos, R. B. *et al.* Purification and characterization of astrocyte-secreted apolipoprotein E and J-containing lipoproteins from wild-type and human apoE transgenic mice. *Neurochem Int* **39**, 415-425, doi:Doi 10.1016/S0197-0186(01)00049-3 (2001).
38 Nickerson, D. A. *et al.* Sequence diversity and large-scale typing of SNPs in the human apolipoprotein E gene. *Genome Res* **10**, 1532-1545, doi:DOI 10.1101/gr.146900 (2000).
39 Namba, Y., Tomonaga, M., Kawasaki, H., Otomo, E. & Ikeda, K. Apolipoprotein-E Immunoreactivity in Cerebral Amyloid Deposits and Neurofibrillary Tangles in Alzheimers-Disease and Kuru Plaque Amyloid in Creutzfeldt-Jakob Disease. *Brain Research* **541**, 163-166, doi:Doi 10.1016/0006-8993(91)91092-F (1991).
40 CORDER, E. H. *et al.* Gene Dose of Apolipoprotein-E Type-4 Allele and the Risk of Alzheimers-Disease in Late-Onset Families. *Science (New York, NY)* **261**, 921-923 (1993).
41 Holtzman, D. M., Herz, J. & Bu, G. J. Apolipoprotein E and Apolipoprotein E Receptors: Normal Biology and Roles in Alzheimer Disease. *Csh Perspect Med* **2**, doi:ARTN a006312 10.1101/cshperspect.a006312 (2012).
42 Castellano, J. M. *et al.* Human apoE isoforms differentially regulate brain amyloid-beta peptide clearance. *Sci Transl Med* **3**, 89ra57, doi:10.1126/scitranslmed.3002156 (2011).
43 Wang, C. *et al.* Gain of toxic apolipoprotein E4 effects in human iPSC-derived neurons is ameliorated by a small-molecule structure corrector. *Nat Med*, doi:10.1038/s41591-018-0004-z (2018).
44 Rebeck, G. W., Reiter, J. S., Strickland, D. K. & Hyman, B. T. Apolipoprotein E in sporadic Alzheimer's disease: allelic variation and receptor interactions. *Neuron* **11**, 575-580 (1993).
45 Holtzman, D. M. *et al.* Apolipoprotein E isoform-dependent amyloid deposition and neuritic degeneration in a mouse model of Alzheimer's disease. *Proceedings of the National Academy of Sciences of the United States of America* **97**, 2892-2897, doi:10.1073/pnas.050004797 (2000).
46 Fryer, J. D. *et al.* Human apolipoprotein E4 alters the amyloid-beta 40 : 42 ratio and promotes the formation of cerebral amyloid angiopathy in an amyloid precursor protein transgenic model. *Journal of Neuroscience* **25**, 2803-2810, doi:10.1523/Jneurosci.5170-04.2005 (2005).
47 Oddo, S., Caccamo, A., Cheng, D. & LaFerla, F. M. Genetically altering Abeta distribution from the brain to the vasculature ameliorates tau pathology. *Brain Pathol* **19**, 421-430, doi:10.1111/j.1750-3639.2008.00194.x (2009).
48 Alonzo, N. C., Hyman, B. T., Rebeck, G. W. & Greenberg, S. M. Progression of cerebral amyloid angiopathy: accumulation of amyloid-beta40 in affected vessels. *Journal of neuropathology and experimental neurology* **57**, 353-359 (1998).

49 Greenberg, S. M., Rebeck, G. W., Vonsattel, J. P., Gomez-Isla, T. & Hyman, B. T. Apolipoprotein E epsilon 4 and cerebral hemorrhage associated with amyloid angiopathy. *Annals of Neurology* **38**, 254-259, doi:10.1002/ana.410380219 (1995).
50 Christie, R., Yamada, M., Moskowitz, M. & Hyman, B. Structural and functional disruption of vascular smooth muscle cells in a transgenic mouse model of amyloid angiopathy. *Am J Pathol* **158**, 1065-1071, doi:10.1016/S0002-9440(10)64053-9 (2001).
51 Hill, R. A. *et al.* Regional Blood Flow in the Normal and Ischemic Brain Is Controlled by Arteriolar Smooth Muscle Cell Contractility and Not by Capillary Pericytes. *Neuron* **87**, 95-110, doi:10.1016/j.neuron.2015.06.001 (2015).
52 Iturria-Medina, Y. *et al.* Early role of vascular dysregulation on late-onset Alzheimer's disease based on multifactorial data-driven analysis. *Nat Commun* **7**, doi:ARTN 11934 10.1038/ncomms11934 (2016).
53 Kretzschmar, H. & Tatzelt, J. Prion disease: a tale of folds and strains. *Brain pathology (Zurich, Switzerland)* **23**, 321-332, doi:10.1111/bpa.12045 (2013).
54 Tan, Z. *et al.* Huntington's disease cerebrospinal fluid seeds aggregation of mutant huntingtin. *Mol Psychiatry* **20**, 1286-1293, doi:10.1038/mp.2015.81 (2015).
55 Guo, J. L. & Lee, V. M.-Y. Cell-to-cell transmission of pathogenic proteins in neurodegenerative diseases. *Nature Medicine* **20**, 130-138, doi:10.1038/nm.3457 (2014).
56 Watts, J. C. *et al.* Serial propagation of distinct strains of Aβ prions from Alzheimer's disease patients. *Proceedings of the National Academy of Sciences* **111**, 10323-10328, doi:10.1073/pnas.1408900111 (2014).
57 Qiang, W., Yau, W. M., Lu, J. X., Collinge, J. & Tycko, R. Structural variation in amyloid-beta fibrils from Alzheimer's disease clinical subtypes. *Nature* **541**, 217-221, doi:10.1038/nature20814 (2017).
58 Guo, J. L. & Lee, V. M. Seeding of normal Tau by pathological Tau conformers drives pathogenesis of Alzheimer-like tangles. *J Biol Chem* **286**, 15317-15331, doi:10.1074/jbc.M110.209296 (2011).
59 Stohr, J. *et al.* Purified and synthetic Alzheimer's amyloid beta (Abeta) prions. *Proc Natl Acad Sci U S A* **109**, 11025-11030, doi:10.1073/pnas.1206555109 (2012).
60 Busciglio, J., Lorenzo, A., Yeh, J. & Yankner, B. A. beta-amyloid fibrils induce tau phosphorylation and loss of microtubule binding. *Neuron* **14**, 879-888 (1995).
61 Mandal, P. K., Pettegrew, J. W., Masliah, E., Hamilton, R. L. & Mandal, R. Interaction between A beta peptide and alpha synuclein: Molecular mechanisms in overlapping pathology of Alzheimer's and Parkinson's in dementia with Lewy body disease. *Neurochem Res* **31**, 1153-1162, doi:10.1007/s11064-006-9140-9 (2006).
62 Hu, R. D., Zhang, M. Z., Chen, H., Jiang, B. B. & Zheng, J. Cross-Seeding Interaction between beta-Amyloid and Human Islet Amyloid Polypeptide. *Acs Chemical Neuroscience* **6**, 1759-1768, doi:10.1021/acschemneuro.5b00192 (2015).
63 Westhof, E. *et al.* Correlation between Segmental Mobility and the Location of Antigenic Determinants in Proteins. *Nature* **311**, 123-126, doi:DOI 10.1038/311123a0 (1984).
64 Thornton, J. M., Edwards, M. S., Taylor, W. R. & Barlow, D. J. Location of Continuous Antigenic Determinants in the Protruding Regions of Proteins. *Embo Journal* **5**, 409-413 (1986).

65 Barlow, D. J., Edwards, M. S. & Thornton, J. M. Continuous and Discontinuous Protein Antigenic Determinants. *Nature* **322**, 747-748, doi:DOI 10.1038/322747a0 (1986).
66 O'Nuallain, B. & Wetzel, R. Conformational Abs recognizing a generic amyloid fibril epitope. *Proceedings of the National Academy of Sciences of the United States of America* **99**, 1485-1490, doi:DOI 10.1073/pnas.022662599 (2002).
67 Kayed, R. *et al.* Fibril specific, conformation dependent antibodies recognize a generic epitope common to amyloid fibrils and fibrillar oligomers that is absent in prefibrillar oligomers. *Molecular Neurodegeneration* **2**, 18, doi:10.1186/1750-1326-2-18 (2007).
68 Glabe, C. G. Conformation-dependent antibodies target diseases of protein misfolding. *Trends in biochemical sciences* **29**, 542-547, doi:10.1016/j.tibs.2004.08.009 (2004).
69 Kayed, R. *et al.* Common structure of soluble amyloid oligomers implies common mechanism of pathogenesis. *Science (New York, NY)* **300**, 486-489, doi:10.1126/science.1079469 (2003).
70 Goldsbury, C., Frey, P., Olivieri, V., Aebi, U. & Muller, S. A. Multiple assembly pathways underlie amyloid-beta fibril polymorphisms. *J Mol Biol* **352**, 282-298, doi:10.1016/j.jmb. 2005.07.029 (2005).
71 Meinhardt, J., Sachse, C., Hortschansky, P., Grigorieff, N. & Fandrich, M. Abeta(1-40) fibril polymorphism implies diverse interaction patterns in amyloid fibrils. *J Mol Biol* **386**, 869-877, doi:10.1016/j.jmb.2008.11.005 (2009).
72 Cerf, E. *et al.* Antiparallel beta-sheet: a signature structure of the oligomeric amyloid beta-peptide. *Biochem J* **421**, 415-423, doi:10.1042/BJ20090379 (2009).
73 Balbach, J. J. *et al.* Supramolecular structure in full-length Alzheimer's beta-amyloid fibrils: evidence for a parallel beta-sheet organization from solid-state nuclear magnetic resonance. *Biophys J* **83**, 1205-1216, doi:10.1016/S0006-3495(02)75244-2 (2002).
74 Glabe, C. G. Structural Classification of Toxic Amyloid Oligomers. *Journal of Biological Chemistry* **283**, 29639-29643, doi:10.1074/jbc.R800016200 (2008).
75 Kayed, R. *et al.* Conformation dependent monoclonal antibodies distinguish different replicating strains or conformers of prefibrillar Abeta oligomers. *Mol Neurodegener* **5**, 57, doi: 10.1186/1750-1326-5-57 (2010).
76 Nussbaum, J. M. *et al.* Prion-like behaviour and tau-dependent cytotoxicity of pyroglutamylated amyloid-beta. *Nature* **485**, 651-655, doi:10.1038/nature11060 (2012).
77 Braak, H. & Braak, E. Neuropathological stageing of Alzheimer-related changes. *Acta Neuropathol* **82**, 239-259 (1991).
78 Oddo, S. *et al.* Triple-transgenic model of Alzheimer's disease with plaques and tangles: intracellular Abeta and synaptic dysfunction. *Neuron* **39**, 409-421 (2003).
79 Spencer, R. K., Li, H. & Nowick, J. S. X-ray crystallographic structures of trimers and higher-order oligomeric assemblies of a peptide derived from Abeta(17-36). *J Am Chem Soc* **136**, 5595-5598, doi:10.1021/ja5017409 (2014).
80 Kreutzer, A. G., Hamza, I. L., Spencer, R. K. & Nowick, J. S. X-ray Crystallographic Structures of a Trimer, Dodecamer, and Annular Pore Formed by an Abeta17-36 beta-Hairpin. *J Am Chem Soc* **138**, 4634-4642, doi:10.1021/jacs.6b01332 (2016).

81 Khoury, M. K., Parker, I. & Aswad, D. W. Acquisition of chemiluminescent signals from immunoblots with a digital single-lens reflex camera. *Anal Biochem* **397**, 129-131, doi:10.1016/j.ab.2009.09.041 (2010).
82 Herzig, M. C., Van Nostrand, W. E. & Jucker, M. Mechanism of cerebral beta-amyloid angiopathy: murine and cellular models. *Brain Pathol* **16**, 40-54 (2006).
83 Petkova, A. T. *et al.* Self-propagating, molecular-level polymorphism in Alzheimer's beta-amyloid fibrils. *Science* **307**, 262-265, doi:10.1126/science.1105850 (2005).
84 Thal, D. R., Rüb, U., Orantes, M. & Braak, H. Phases of A beta-deposition in the human brain and its relevance for the development of AD. *Neurology* **58**, 1791-1800 (2002).
85 Cacquevel, M., Aeschbach, L., Houacine, J. & Fraering, P. C. Alzheimer's Disease-Linked Mutations in Presenilin-1 Result in a Drastic Loss of Activity in Purified γ-Secretase Complexes. *PLoS ONE* **7**, e35133, doi:10.1371/journal.pone.0035133 (2012).
86 Vinters, H. V. Emerging Concepts in Alzheimer's Disease. *Annual review of pathology*, doi:10.1146/annurev-pathol-020712-163927 (2014).
87 Holtzman, D. M., Morris, J. C. & Goate, A. M. Alzheimer's disease: the challenge of the second century. *Science translational medicine* **3**, 77sr71-77sr71, doi:10.1126/scitranslmed.3002369 (2011).
88 Frackowiak, J. *et al.* Secretion and accumulation of Alzheimer's beta-protein by cultured vascular smooth muscle cells from old and young dogs. *Brain research* **676**, 225-230 (1995).
89 Winkler, D. T. *et al.* Spontaneous Hemorrhagic Stroke in a Mouse Model of Cerebral Amyloid Angiopathy. *Journal of Neuroscience* **21**, 1619-1627 (2001).
90 Van Nostrand, W. E., Melchor, J. P. & Ruffini, L. Pathologic Amyloid β−Protein Cell Surface Fibril Assembly on Cultured Human Cerebrovascular Smooth Muscle Cells. *Journal of Neurochemistry* **70**, 216-223, doi:10.1046/j.1471-4159.1998.70010216.x (1998).
91 Weller, R. O. *et al.* Cerebral Amyloid Angiopathy. *The American Journal of Pathology* **153**, 725-733, doi:10.1016/S0002-9440(10)65616-7 (2010).
92 Maier, F. C. *et al.* Longitudinal PET-MRI reveals β-amyloid deposition and rCBF dynamics and connects vascular amyloidosis to quantitative loss of perfusion. *Nature Medicine* **20**, 1485-1492, doi:10.1038/nm.3734 (2014).
93 Oakley, H. *et al.* Intraneuronal beta-amyloid aggregates, neurodegeneration, and neuron loss in transgenic mice with five familial Alzheimer's disease mutations: potential factors in amyloid plaque formation. *J Neurosci* **26**, 10129-10140, doi:10.1523/JNEUROSCI.1202-06.2006 (2006).
94 Sosna, J. *et al.* Early long-term administration of the CSF1R inhibitor PLX3397 ablates microglia and reduces accumulation of intraneuronal amyloid, neuritic plaque deposition and pre-fibrillar oligomers in 5XFAD mouse model of Alzheimer's disease. *Mol Neurodegener* **13**, 11, doi:10.1186/s13024-018-0244-x (2018).
95 Porto, A. *et al.* Smooth muscle cells in human atherosclerotic plaques secrete and proliferate in response to high mobility group box 1 protein. *FASEB J* **20**, 2565-2566, doi:10.1096/fj.06-5867fje (2006).
96 Iadecola, C. The Pathobiology of Vascular Dementia. *Neuron* **80**, 844-866, doi:10.1016/j.neuron.2013.10.008 (2013).

97 Stopa, E. G. *et al.* Cerebral cortical arteriolar angiopathy, vascular beta-amyloid, smooth muscle actin, braak stage, and APOE genotype. *Stroke* **39**, 814-821, doi:10.1161/Strokeaha.107.493429 (2008).
98 Cunningham, C. & Hennessy, E. Co-morbidity and systemic inflammation as drivers of cognitive decline: new experimental models adopting a broader paradigm in dementia research. *Alzheimers Res Ther* **7**, doi:ARTN 33 10.1186/s13195-015-0117-2 (2015).
99 Festoff, B. W., Sajja, R. K., van Dreden, P. & Cucullo, L. HMGB1 and thrombin mediate the blood-brain barrier dysfunction acting as biomarkers of neuroinflammation and progression to neurodegeneration in Alzheimer's disease. *J Neuroinflammation* **13**, 194, doi:10.1186/s12974-016-0670-z (2016).
100 Davis-Salinas, J. & Van Nostrand, W. E. Amyloid beta-protein aggregation nullifies its pathologic properties in cultured cerebrovascular smooth muscle cells. *The Journal of biological chemistry* **270**, 20887-20890 (1995).
101 Sprague, A. H. & Khalil, R. A. Inflammatory cytokines in vascular dysfunction and vascular disease. *Biochemical Pharmacology* **78**, 539-552, doi:10.1016/j.bcp.2009.04.029 (2009).
102 Wang, Z., Natte, R., Berliner, J. A., van Duinen, S. G. & Vinters, H. V. Toxicity of Dutch (E22Q) and Flemish (A21G) mutant amyloid beta proteins to human cerebral microvessel and aortic smooth muscle cells. *Stroke* **31**, 534-538 (2000).
103 De Jonghe, C. *et al.* Pathogenic APP mutations near the gamma-secretase cleavage site differentially affect Abeta secretion and APP C-terminal fragment stability. *Hum Mol Genet* **10**, 1665-1671 (2001).
104 Yang, A. J., Chandswangbhuvana, D., Margol, L. & Glabe, C. G. Loss of endosomal/lysosomal membrane impermeability is an early event in amyloid A beta 1-42 pathogenesis. *J Neurosci Res* **52**, 691-698, doi:Doi 10.1002/(Sici)1097-4547(19980615)52:6<691::Aid-Jnr8>3.0.Co;2-3 (1998).
105 Hatami, A., Albay, R., 3rd, Monjazeb, S., Milton, S. & Glabe, C. Monoclonal antibodies against Abeta42 fibrils distinguish multiple aggregation state polymorphisms in vitro and in Alzheimer disease brain. *J Biol Chem* **289**, 32131-32143, doi:10.1074/jbc.M114.594846 (2014).
106 Hatami, A., Monjazeb, S., Milton, S. & Glabe, C. G. Familial Alzheimer's Disease Mutations within the Amyloid Precursor Protein Alter the Aggregation and Conformation of the Amyloid-beta Peptide. *J Biol Chem* **292**, 3172-3185, doi:10.1074/jbc.M116.755264 (2017).
107 Esparza, T. J. *et al.* Amyloid-beta oligomerization in Alzheimer dementia versus high-pathology controls. *Ann Neurol* **73**, 104-119, doi:10.1002/ana.23748 (2013).
108 Van Nostrand, W. E., Rozemuller, A. J. M., Chung, R., Cotman, C. W. & Saporito Irwin, S. M. Amyloid β-protein precursor in cultured leptomeningeal smooth muscle cells. *Amyloid* **1**, 1-7, doi:10.3109/13506129409148618 (1994).
109 Frackowiak, J. *et al.* Secretion and accumulation of Alzheimer's beta-protein by cultured vascular smooth muscle cells from old and young dogs. *Brain research* **676**, 225-230 (1995).
110 De Strooper, B. & Karran, E. The Cellular Phase of Alzheimer's Disease. *Cell* **164**, 603-615, doi:10.1016/j.cell.2015.12.056 (2016).

111 McLean, D., Cooke, M. J., Albay III, R., Glabe, C. & Shoichet, M. S. Positron Emission Tomography Imaging of Fibrillar Parenchymal and Vascular Amyloid-β in TgCRND8 Mice. *ACS Chemical Neuroscience*, 130319125942006, doi:10.1021/cn300226q (2013).